Numerical Studies on the Induced Ignition Process of Various Fuels

Zur Erlangung des akademischen Grades einer

Doktorin der Ingenieurwissenschaften (Dr.-Ing.)

von der KIT-Fakultät für Maschinenbau des Karlsruher Instituts für Technologie (KIT)

angenommene

Dissertation

von

M.Sc. Chunwei Wu

Tag der mündlichen Prüfung: 20.12.2024
Erster Gutachter: Prof. Dr. rer. nat. habil. Ulrich Maas
Zweiter Gutachter: Prof. Dr. Shenqyang (Steven) Shy

Acknowledgements

Completing this dissertation has been an incredibly challenging yet deeply rewarding experience. Along the way, I have been fortunate to receive the support, guidance, and encouragement of many wonderful people. Without their belief in me and their contributions, this work would not have been possible. I am profoundly thankful for their presence in my life.

First and foremost, I would like to express my heartfelt gratitude to my advisor, Prof. Dr. rer. nat. habil. Ulrich Maas. His exceptional mentorship, profound expertise in ignition and numerical simulation, and insightful guidance have been invaluable throughout my research. I am especially grateful for his patience, constructive feedback, and the many opportunities he offered me, which have shaped both this dissertation and my personal and professional growth. His dedication to excellence continues to inspire me.

I am also deeply thankful to my co-advisor, Prof. Dr. Shenqyang (Steven) Shy, for his collaboration and guidance during my doctoral studies. Working together on several papers greatly expanded my understanding of ignition-related experiments, and his support was instrumental to this dissertation's progress. My gratitude also extends to Prof. Dr. sc. techn. Thomas Koch, who chaired my defense committee and provided valuable support and insights throughout the examination process.

To my colleagues at the Institute of Technical Thermodynamics at the Karlsruhe Institute of Technology: thank you for fostering a collaborative and supportive environment. In particular, I am deeply grateful to Dr.-Ing. Robert Schießl for his generous assistance, insightful advice, and encouragement, which significantly advanced my work. I would also like to acknowledge the Deutsche Forschungsgemeinschaft (DFG) for their financial support through the DFG-MOST collaboration projects.

On a more personal note, I am profoundly grateful to my family. To my parents, Qingsong Wu and Yi Yang: your unwavering love and encouragement have been my anchor through every stage of this journey. Your belief in me, especially during the hardest times, gave me the strength to keep going. I deeply appreciate your sacrifices and the foundation of support

you've provided, which made this accomplishment possible. I also thank my grandparents for their unconditional love and support.

Finally, my deepest thanks go to my husband, Yueyao. Your steadfast presence, patience, and unwavering belief in me have been a source of comfort and strength throughout this process. Your encouragement has helped me navigate the challenges of this journey, and I am endlessly grateful for your love and partnership.

This dissertation is not just a reflection of my efforts but a testament to the collective support and encouragement of so many people. To all who have been part of this journey, thank you from the bottom of my heart.

Abstract

This work presents a detailed numerical investigation on induced ignition and early flame propagation in both hydrocarbon fuels (methane and primari reference fuels, PRF) and non-carbon fuels (ammonia and ammonia/hydrogen mixtures) using one-dimensional simulations, detailed chemical kinetics and detailed transport models. The study focuses on the dependence of minimum ignition energy (MIE) on various ignition parameters, which is crutial in improving combustion efficiency and ensuring safety by preventing undesired ignition.

Through the analysis of various ignition parameters, including mixture composition, pressure, and ignition geometry, the research uncovers key insights into the ignition behavior of different fuel mixtures. Simulations accurately replicate experimental observations, highlighting significant dependencies of MIE on factors such as the equivalence ratio and ignition geometry. This study also investigates the stochastic nature of ignition radii, which was identified as a crucial parameter contributing to the stochastic ignition behavior observed in experiments.

The findings contribute to the field by providing a comprehensive quantitative analysis of MIE dependencies and validating simulation results with experimental data. The research underscores the importance of understanding the complex interaction between chemical kinetics and transportation during induced ignition process. This work provides valuable insights for the design of more efficient and safer combustion systems.

Kurzfassung

Diese Arbeit präsentiert eine detaillierte numerische Untersuchung der erzwungenen Zündung und der frühen Flammenausbreitung in sowohl kohlenwasserstoffbasierten Brennstoffen (Methan und Primärreferenzbrennstoffe, PRF) als auch kohlenstofffreien Brennstoffen (Ammoniak und Ammoniak/Wasserstoff-Gemischen) unter Verwendung eindimensionaler Simulationen, detaillierter chemischer Kinetik und detaillierter Transportmodelle. Die Studie konzentriert sich auf die Abhängigkeit der minimalen Zündenergie (MIE) von verschiedenen Zündparametern, die entscheidend für die Verbesserung der Verbrennungseffizienz und die Gewährleistung der Sicherheit durch Vermeidung unerwünschter Zündungen ist.

Durch die Analyse verschiedener Zündparameter, darunter Gemischzusammensetzung, Druck und Zündgeometrie, deckt die Forschung wichtige Erkenntnisse über das Zündverhalten unterschiedlicher Brennstoffgemische auf. Die Simulationen replizieren experimentelle Beobachtungen genau und zeigen signifikante Abhängigkeiten der MIE von Faktoren wie dem Äquivalenzverhältnis und der Zündgeometrie. Diese Studie untersucht auch die stochastische Natur der Zündradien, die als ein entscheidender Parameter identifiziert wurde, der zum stochastischen Zündverhalten in Experimenten beiträgt.

Die Ergebnisse tragen zum Forschungsfeld bei, indem sie eine umfassende quantitative Analyse der MIE-Abhängigkeiten liefern und die Simulationsergebnisse mit experimentellen Daten validieren. Die Forschung unterstreicht die Bedeutung des Verständnisses der komplexen Wechselwirkung zwischen chemischer Kinetik und Transportvorgängen während des Zündprozesses. Diese Arbeit liefert wertvolle Erkenntnisse für die Entwicklung effizienterer und sichererer Verbrennungssysteme.

Contents

1 Introduction

Investigating ignition and early flame propagation processes is essential in combustion research, with significant implications for applications such as internal combustion engines and gas turbines [113]. Accurately describing the ignition process is vital not only for the development of combustion machines with high efficiency and low emission but also for safety-related concerns.

As the demand for efficient and environmentally conscious combustion technologies grows, the focus on ignition processes becomes increasingly imperative in both experimental and numerical investigations. One advantage of numerical investigations, compared to experimental investigations, is the reduction in the cost and potential risks of experimental setups [86]. Moreover, simulations allow precise control over variables and parameters during combustion processes—a level of control that is challenging to achieve in experimental setups. Furthermore, simulations generate detailed data on temperature distribution, reaction rates, and species concentrations. This information might be challenging or impossible to obtain through experiments alone. While experiments remain crucial for validating and verifying simulation results, the combination of both approaches allows researchers to gain a comprehensive understanding of combustion processes.

Since numerical simulations play an important role in understanding combustion processes, they are essential for exploring the specific combustion characteristics of individual fuels. As an important component of natural gas, the combustion characteristics of methane directly impact environmental considerations. Primary reference fuels (PRF), a binary mixture of iso-octane and n-heptane, are surrogate fuels that aim to replicate the key characteristics of gasoline, which is still widely used in combustion engines. Investigating the ignition process of methane and PRF not only assists in the development of combustion devices but also provides fundamental knowledge of the interaction between chemical kinetics and transport processes during combustion.

However, even though certain actions (e.g., lean combustion) can be implemented in the combustion process of fossil fuels such as methane and gasoline, they still significantly contribute to carbon dioxide emissions, directly con-

tributing to global warming. This underscores the importance of sustainable, non-carbon fuels, such as ammonia and hydrogen.

For all fuels mentioned above, auto-ignition processes (the ignition process without external energy deposition), and stationary flame propagation are intensively studied in the last few decades. Ignition delay time (IDT) and laminar burning velocity of methane (see e.g. [43, 48, 143]), PRF (see e.g. [13, 33, 54, 76]), ammonia and ammonia/hydrogen blend (see e.g. [14, 38, 49, 65, 96, 100]) are intensively studied both in experiments and simulations . However, there are less studies of induced ignition processes (the ignition process with external energy or radical deposition) and the transition from a flame kernel to a self-sustained flame. In this work, the initiation of flame with external energy source and early flame propagation of various fuels is studied numerically, with a comparison to the experimental results.

For induced ignition, the amount of external energy deposited into the system is crucial. Minimum Ignition Energy (MIE) defines the threshold above which the fuel/air mixture reaches high temperatures, allowing rapid chemical reactions to start (see e.g. [123]). This characteristic is vital for specific fuel/air mixtures. In this work, MIEs for methane, PRF, and ammonia/hydrogen mixtures are investigated, with a focus on their dependence on fuel composition, pressure, and source size. The objective is to understand the interaction between chemical reactions and transport effects, such as species diffusion and heat conduction, during ignition. Numerical simulations are employed, incorporating detailed chemical and transport models, and are validated with experimental results.

Chapter 2 provides a phenomenological description of induced ignition, encompassing the ignition process, flame structure, and flame extinction. Chapter 3 delves into the mathematical methods employed in this work, covering the Navier-Stokes equations, mathematical modeling of one-dimensional unsteady combustion processes, and unsteady combustion processes with counterflow configurations. This chapter also discusses the chemical kinetics and transport processes necessary for solving the Navier-Stokes equations. Chapters 4, 5, and 6 offer detailed descriptions and analyses of the ignition and early flame propagation processes for methane (Chapter 4), PRF (Chapter 5), and ammonia/hydrogen (Chapter 6). These chapters focus on the dependence of the MIE on various ignition parameters such as mixture composition, ignition kernel geometry, pressure, and the uncertainty of ignition radius.

2 Induced Ignition

The ignition process refers to the unsteady onset of combustion reactions between a fuel and an oxidizer, which then leads to a steadily burning flame [116, 123]. Ignition can be further divided into auto-ignition and induced ignition, based on the absence or presence of an external ignition source [123].

Auto-ignition, commonly employed in diesel engines, occurs when the temperature, pressure, and mixture composition are sufficient for ignition without any external energy source [92]. During the ignition delay time (IDT), a key characteristic of auto-ignition, active radicals accumulate while the temperature remains nearly constant. Auto-ignition occurs when the radical pool becomes large enough [123]. In contrast, induced ignition, commonly used in gasoline engines, is initiated by an external heat source, such as a spark discharge. This raises the temperature locally within the energy deposition volume. Auto-ignition then occurs within this ignition volume, forming a flame kernel that propagates into the unburnt mixture [123]. Additionally, ignition can also occur through radical generation [71, 123].

In this work, induced ignition with the assistance of an external heating source is investigated. This is important not only for achieving a desired combustion process with high efficiency and low emissions but also for preventing unwanted combustion in safety-related issues. As mentioned before, in an induced ignition process, a portion of the mixture is locally heated by an external energy source, causing a rise in temperature within the ignition volume. Elementary reactions begin to take place, generating additional heat. If the rate of heat production exceeds the rate of heat loss (e.g., through heat conduction to the cold mixture), a flame kernel is formed, resulting in successful ignition. Otherwise, the ignition attempt concludes with an unsuccessful outcome [68, 123]. Following the successful formation of a flame kernel, the flame front propagates into the unburnt mixture. During the early flame propagation phase, effects such as the stretch effect might lead to flame extinction, which will be explained in detail in Section 2.4. In cases where flame extinction doesn't occur, the flame will propagate into a self-sustained steady-state flame.

In this chapter, the phenomenological description of the induced ignition and early flame propagation is addressed, including the flame structure, the minimum ignition energy, and flame extinction.

2.1 Flame Structure

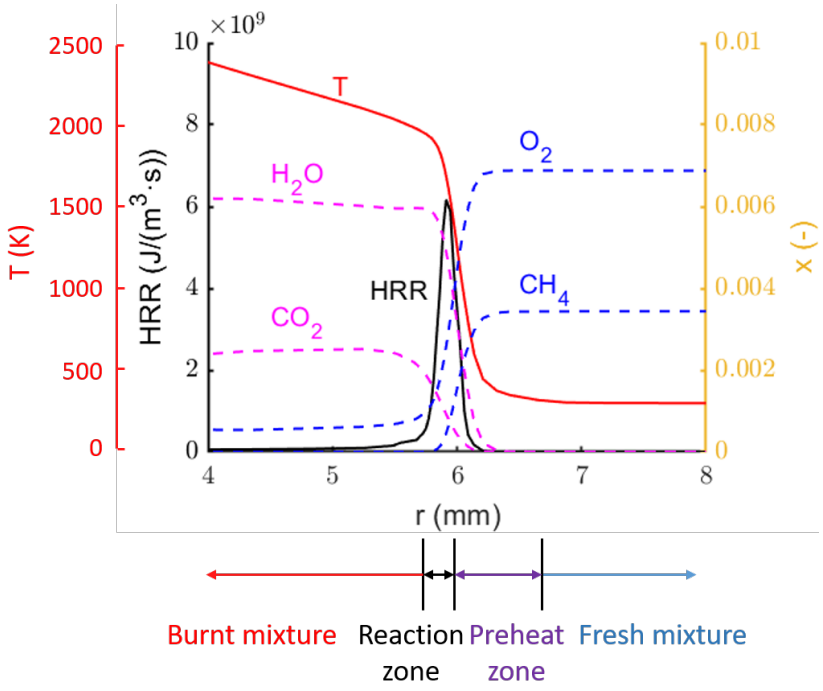

Figure 2.1: Profile of temperature (T), heat release rate (HRR), mole fractions of reactants (CH_4 and O_2) and products (H_2O and CO_2) of a planar laminar free premixed flame of stoichiometric methane/air mixture, $p = 1\,\mathrm{bar}$, $T_u = 300\,\mathrm{K}$

For the case of freely burning premixed laminar flat flame, the propagating speed is defined as the laminar burning velocity v_L, which is a characteristic of a given mixture at a specific temperature and pressure [123]. For other flame configurations, such as a spherically outwardly propagating flame, the flame propagation speed might differ from the laminar burning velocity.

Figure 2.1 shows the flame structure of a planar laminar premixed flame of a stoichiometric methane/air mixture under ambient conditions. The unburnt mixture of fuel and air has a temperature T_u and is heated in the preheat zone, the temperature of the mixture increases. Subsequently, in a much

thinner reaction zone dominated by reaction and diffusion, extensive chemical reactions occur, leading to a rapid decrease in reactant concentration (in this case, CH_4 and O_2) and a simultaneous increase in product concentration (in this case, CO_2 and H_2O). The significant heat release resulting from these chemical reactions is evident in a thin peak in the heat release rate (HRR). In the reaction zone, due of the rapid chemical reactions, intermediates are produced and then consumed. The released heat then raises the temperature of the unburnt mixture nearby through heat conduction, and the flame front subsequently propagates into the unburnt mixture [10, 71, 123].

In both simulations and experimental observations, the flame area is not an infinitely thin sheet separating the burnt and unburnt mixture, but has a finite thickness [71], the position of flame front has to be defined. In simulations, one popular way to define the position of the flame front, which is also adopted in this work, is the peak of the HRR [121], which indicates the strongest energy transition from chemical potential energy to thermal energy. In experiments, a direct measurement of HRR is not practical, concentrations of HRR indicators are measured to represent the position of the flame front. Examples include the product CH_2O and OH concentrations [93] or HCO concentration [89] for methane/air flame. For ammonia/hydrogen/air flame, Chi et al. [25] used the concentration of NH and OH to represent the profile of HRR. For one-dimensional simulations using spherically and cylindrically symmetric geometry, as applied in this work, the flame radius r_f is defined as the distance between the flame front and the symmetric center (left boundary in simulations), as is shown in Fig. 2.2. The flame propagation speed s_u is then defined as the temporal rate of change of r_f:

$$s_u = \frac{dr_f}{dt} \tag{2.1}$$

Defining the ignition radius using physical coordinates directly captures the movement of the flame front. However, since the flame front's movement can be influenced by both chemical reactions and thermal expansion, this definition may obscure the underlying processes. It becomes challenging to distinguish between flame displacement and flame propagation. Another description for the movement of the flame front using a mass-based Lagrangian coordinate will be explained in Section 3.1.1.

2.2 Flammability Limit

For all fuels, a flammability limit exists in terms of mixture composition within which the mixture can be ignited with sufficiently high ignition energy.

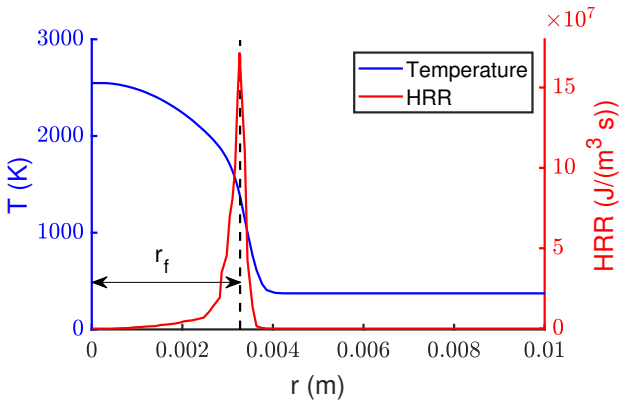

Figure 2.2: Definition of the flame radius based on the location of the peak of the heat release rate (HRR) [128]

In this work, the fuel equivalence ratio Φ is used to describe the mixture composition [123]:

$$\Phi = \frac{x_{\text{fuel}}/x_{\text{air}}}{x_{\text{fuel,stoich}}/x_{\text{air,stoich}}} \tag{2.2}$$

Here, x_{fuel} and x_{air} represent the mole fractions of fuel and air in the presented mixture, while $x_{\text{fuel,stoich}}$ and $x_{\text{air,stoich}}$ represent the mole fractions of fuel and air in a stoichiometric mixture, where fuel and air are completely consumed. The oxidizer in the mixture is chosen to be air. With the definition of Φ, it becomes straightforward to categorize premixed combustion into rich combustion ($\Phi > 1$), stoichiometric combustion ($\Phi = 1$), and lean combustion ($\Phi < 1$) [123].

For all flammable mixtures at a certain pressure and temperature, lower flammability limits (LFL) and upper flammability limits (UFL) exist. Beyond these flammability limits, where the mixture is either too lean or too rich, despite efforts to increase the ignition energy and minimize heat loss, ignition remains unattainable [71]. There are several explanations of the existence of flammability limits, including slow chemical kinetic caused by decrease of flame temperature [70], heat loss through heat conduction to the unburnt mixture [77], and stretch of the flame front [74].

The LFL and UFL can be experimentally determined for fuel/oxidizer mixtures at a specific pressure and temperature [27]. The apparatus and procedures have a effect on the determined flammability limits [102]. There exist different standards to determine the LFL and UFL in experiments. For example, German DIN 51649 method uses a glass cylinder as ignition vessel

and visually flame detachment as criterion. The explosion limit is defined as the last non-ignition point [35].

2.3 Minimum Ignition Energy

Within these flammability limits, ignition occurs when the external energy source is sufficiently strong. The minimum ignition energy (MIE) is the threshold ignition energy, above which the mixture in the ignition volume successfully ignites. Another important concept is the minimum ignition temperature, above which fast chemical reactions are triggered and the ignition is successful [123].

In the past century, both numerical and experimental investigations have been carried out on the MIE. One of the most widely referenced works concerning MIE data is that of Lewis and von Elbe [74], which includes MIE values for various fuels under different conditions. Since then, MIE values for different fuels are studied experimentally for laminar flames (see e.g. [10, 16, 36, 88, 128]) and turbulent flames (see e.g. [9, 53]).

Numerical models for the ignition processes are also developed. One popular one-dimensional numerical model of ignition process was developed by Maas and Warnatz [80]. In their work, the MIE of hydrogen/oxygen mixtures and its dependence on mixture composition, ignition parameters, and pressure were determined numerically. Several authors have performed one-dimensional numerical simulations and determined the MIE for various fuels (see e.g. [129, 138]). In comparison to the experimental results, it was found that some important phenomena during ignition and early flame propagation processes were accurately predicted using a one-dimensional simulation model [128].

In this work, one-dimensional simulations of ignition and early flame propagation processes are conducted for both carbon-containing and non-carbon fuels. The primary objective is to explore the relationship between the MIE and various influencing parameters. In experiments, the ignition process exhibits statistical behavior due to the uncertainties in the ignition parameters. This statistical behavior is also investigated numerically in this work, taking into account the fluctuations of the ignition radius and stretch rate.

2.3.1 Determination of Minimum Ignition Energy and Stochastic Nature of Ignition Process

Experimental Measurement of Minimum Ignition Energy

Fig. 2.3 shows a schematic of a combustion vessel for the spark ignition experiments. The ignition energy is provided with a spark ignition system with two electrodes. The geometry of the electrodes can be either sharp ended (see e.g. [10, 105]), or flanged (see e.g. [74]). Fans are typically used in both laminar ignition experiments (for improved mixing, turned off before ignition) and turbulent ignition experiments (for turbulence generation) [105]. Ignition detection can be achieved through pressure measurement, temperature measurement, schlieren visualization, or a combination of these methods [10].

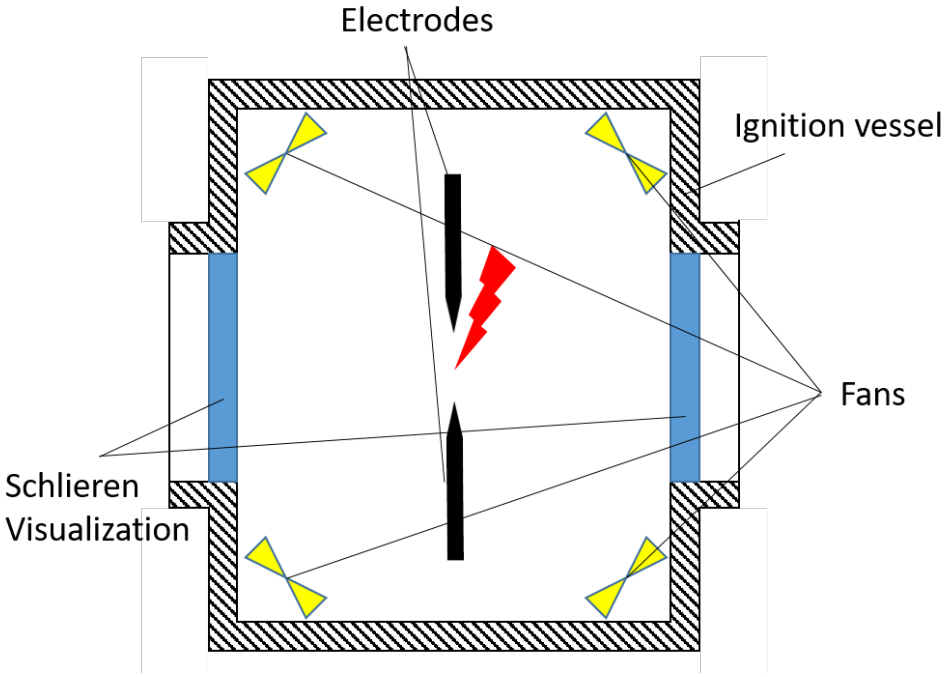

Figure 2.3: A schematic of a combustion vessel for the spark ignition experiments

The ignition process in experiments has a stochasitic nature [10, 128]. In other words, even with the same ignition energy, successful ignition and ignition failure might coexist. In the experiments, the MIE is not a single threshold value and has to be determined using a statistical method [10, 40, 53]. This result indicates the presence of uncertainties during the ignition

process even for laminar ignitions, such as uncertainties in the size of the ignition kernel [10]. In turbulent flow ignition, fluctuations in flow velocity introduce additional uncertainties in ignition parameters and stretch rate of the flame front. For a more accurate prediction of the stochastic nature of the ignition process through simulations, it is crucial to account for these uncertainties in the numerical model.

Numerical Estimation of Minimum Ignition Energy with fixed parameters

In simulations with well-defined initial and boundary conditions, the MIE represents a single threshold above which ignition is successful. However, the definition of successful ignition has to be clarified. In some cases, the formation of a flame kernel does not guarantee flame propagation; the formed flame kernel might quench due to various reasons, such as flame curvature [128].

Two MIEs are defined in this situation:

- $\mathrm{MIE}_{\mathrm{ini}}$, above which a flame kernel is formed
- $\mathrm{MIE}_{\mathrm{prop}}$, above which the flame can evolve into a self-sustained propagating flame

In the results chapters, the various scenarios of ignition and early flame propagation processes for different fuels are described and analyzed individually in the first section. The explanation for the existence of flame extinction in some cases and its absence in others is provided in detail.

Statistical Determination of Minimum Ignition Energy

As mentioned earlier, ignition experiments have a stochastic nature due to the uncertainties inherent in experimental conditions. To account for these uncertainties in simulations, variable values are assigned to certain parameters, such as ignition radius, rather than using fixed values. An example is shown in Fig. 2.4(a), where simulations were conducted using different ignition radii that are normally distributed. The logistic regression method, which models the probability of a binary outcome by applying a logistic function to a linear combination of input features [51], is utilized to determine the MIE. Logistic regression method is also a popular approach in experimental MIE determination [10, 105, 128].

In alignment with experimental conditions, the statistical method defines a successful ignition ("go"case) as the formation of a self-sustained flame

(flame propagation). Conversely, ignition failure and flame extinction are categorized as "no go"cases [10, 105]. The MIE determined in simulations using the statistical method corresponds to the MIE observed in experiments, as well as to the $\mathrm{MIE}_{\mathrm{prop}}$ obtained in simulations with fixed parameters.

For the i^{th} simulation with an ignition energy E_i, a binary result was assigned:

$$y_i = \begin{cases} 1 & \text{"go"case} \\ 0 & \text{"no go"case} \end{cases} \tag{2.3}$$

A probability distribution for the occurrence of a "go"case at an ignition energy E_i is defined as:

$$p(E_i) = \text{Probability}(y_i = 1; E_i) \tag{2.4}$$

For the i^{th} simulation with an ignition energy E_i, a binary result was assigned:

$$y_i = \begin{cases} 1 & \text{"go"case} \\ 0 & \text{"no go"case} \end{cases} \tag{2.5}$$

A probability distribution for the occurrence of a "go"case at an ignition energy E_i is defined as:

$$p(E_i) = \text{Probability}(y_i = 1; E_i) \tag{2.6}$$

The probability distribution can be expressed in the form of a logistic distribution function:

$$p(E) = \frac{1}{1 + e^{-(\beta_0 + \beta_1 E)}} \tag{2.7}$$

where β_0 and β_1 are parameters that can be estimated through maximizing the likelihood function, which is a collective representation of all ignition energies and binary results from the n tests:

$$L = \prod_{i=1}^{n} p(E_i)^{y_i} (1 - p(E_i))^{1-y_i} \tag{2.8}$$

To estimate the ignition energy E_q at an ignition probability of q, which means

$$q = p(E_q) = \frac{1}{1 + e^{-(\beta_0 + \beta_1) E_q}}. \tag{2.9}$$

The solution of the equation gives

$$E_q = \frac{1}{\beta_1} ln[\frac{q}{1-q} - \beta_0] \tag{2.10}$$

The upper confidence limit (UCL) and lower confidence limit (LCL) for the $100 \cdot (1 - \frac{\alpha}{2})\%$ confidence interval regarding E_q can be determined:

$$\mathrm{UCL/LCL} = E_q \pm Z_{\frac{\alpha}{2}} \sqrt{(\sigma_{00} + 2E_q\sigma_{01} + E_q^2\sigma_1 1)/\beta_1^2} \tag{2.11}$$

where $\sigma_0 0$ and $\sigma_1 1$ are the variances of β_0 and β_1, $\sigma_0 1$ is the covariance of β_0 and β_1, α is 1 minus the confidence level ($\alpha = 1 - 0.95 = 0.05$ for 95% confidence level) and $Z_{\frac{\alpha}{2}}$ represents the $100 \cdot (1 - \frac{\alpha}{2})\%$ percentile derived from a standard cumulative Gaussian distribution with parameters $\mu = 0$ and $\sigma = 1$. This analysis yields a cumulative probability distribution of n simulations and establishes a confidence envelope concerning the probability of ignition relative to ignition energy.

An example is shown in Fig. 2.4. Here, the MIE of an n-heptane/air mixture ($\phi = 0.8$) using a cylindrical geometry with an ignition duration of $\tau_s = 100\,\mu s$ is determined statistically. The ignition radius for each simulation is a random number generated from a normal distribution with a mean radius of $\mu_{r_s} = 0.5\,\mathrm{mm}$ and a standard deviation of $\sigma_{r_s} = 0.15\,\mathrm{mm}$.

The overlapping region (from $E_{ig} = 0.8\,\mathrm{mJ}$ to $E_{ig} = 1.28\,\mathrm{mJ}$) is clearly seen in Fig. 2.4. In this region, "go"cases and "no go"cases can co-exist. The existence of the overlapping region can be attributed to fluctuations in the ignition energy density, which are caused by variations in the ignition radius. For instance, when the ignition radius exceeds the desired value, the corresponding ignition volume also exceeds the desired value. Consequently, the ignition energy density within the ignition volume may fall below the requisite minimum threshold. As a result, the mixture within the ignition volume fails to attain the necessary temperature for ignition initiation.

The MIE estimated at an ignition probability 50% is $E_{ig}(p_{ig} = 50\%) = 1.04\,\mathrm{mJ}$, about 20% larger than the MIE calculated with a fixed ignition radius $r_s = 0.5\,\mathrm{mm}$. In the results section, the impact of the statistical nature of ignition on the MIE of different fuels will be discussed, along with the underlying reasons.

2.3.2 Factors influencing Minimum Ignition Energy

The MIE depends on various factors. Firstly, it strongly depends on the physical and chemical characteristics of the fuel or fuel mixture. For example, the MIE of a stoichiometric hydrogen/air mixture can be an order smaller than that of a stoichiometric methane/air mixture under the same conditions [74, 84]. Besides the type of fuel or fuel mixtures, the fuel/air equivalence ratio also plays a role in the MIE, since both the specific constant pressure heat

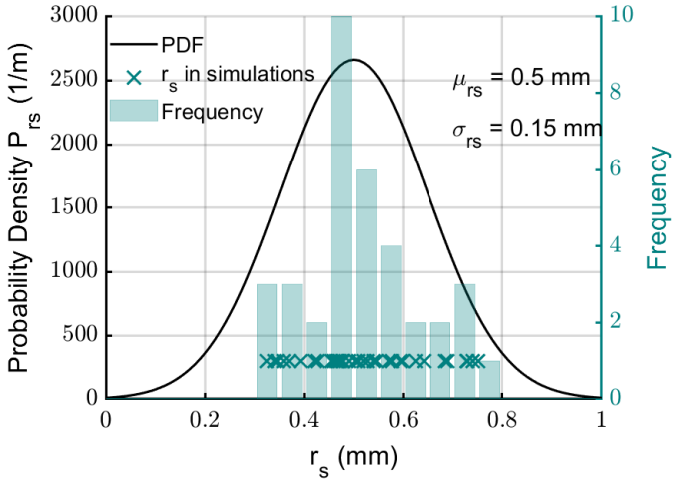

(a) Probability density function of ignition radius

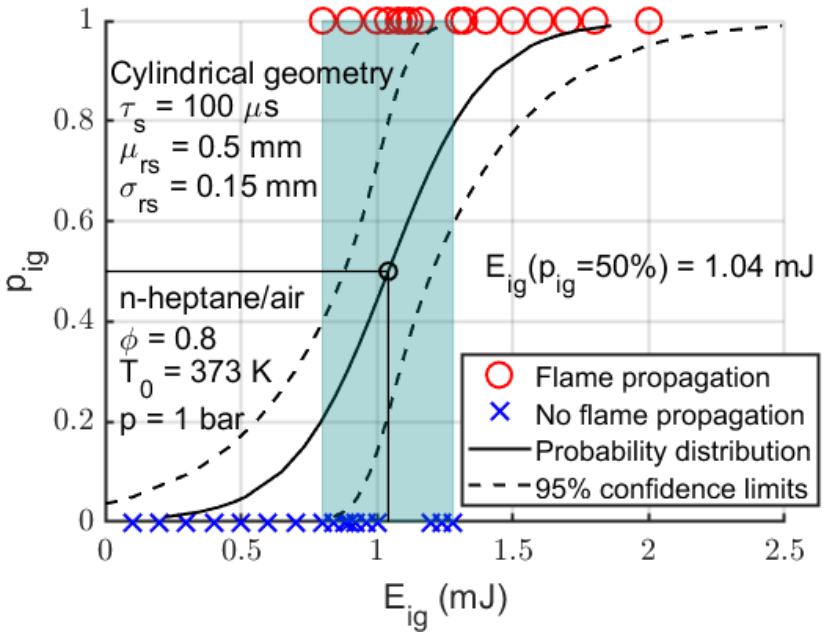

(b) Ignition probability

Figure 2.4: Probability density function of ignition radius and statistical determination of minimum ignition energy for n-heptane/air mixture ($\phi = 0.8$, $T_0 = 373$ K, $p = 1$ bar) with cylindrical geometry, the ignition radius has a normal distribution (mean $\mu_{r_s} = 0.5\text{mm}$, standard deviation $\sigma_{r_s} = 0.15\text{mm}$)

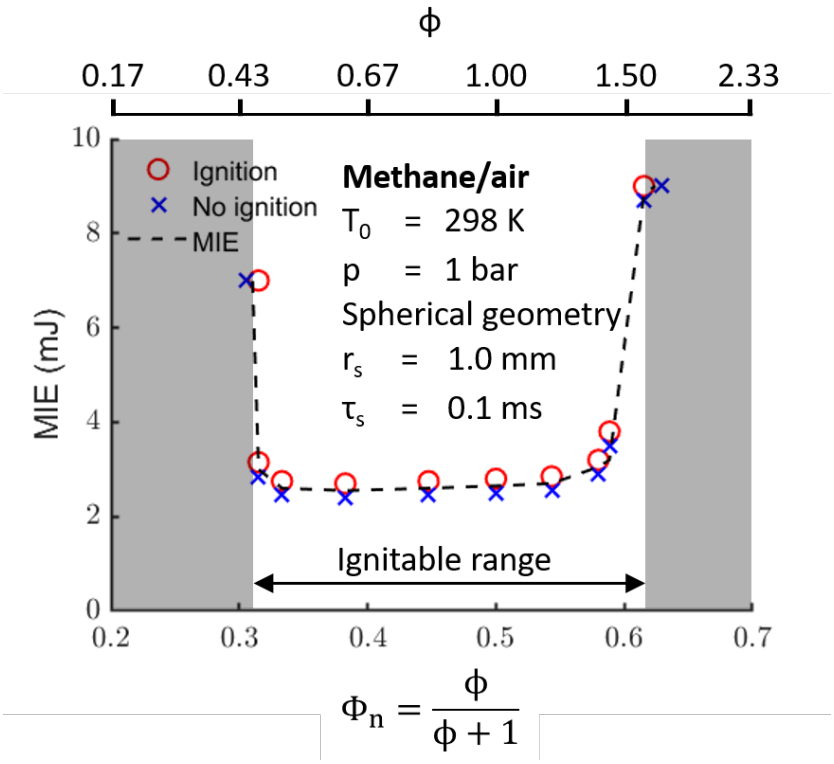

Figure 2.5: The dependence of MIE on equivalence ratio at 1 bar and $T_0 = 298\,\mathrm{K}$ for methane/air mixture with spherical geometry [129]

capacity and the chemical reaction rate depend on the equivalence ratio [74, 79]. The dependence of MIE on equivalence ratio has a U-shape. As an example, the dependence of MIE for methane/air mixture under atmospheric conditions is shown in Fig. 2.5. Moreover, initial temperature, pressure, and flow field are important factors which affect MIE. Finally, ignition parameters, such as the size and geometry of the ignition volume, also influence the MIE. The size of the ignition volume determines the total amount of fresh mixture to be heated, while the geometry of the ignition volume affects its diffusion properties [79, 80].

The MIE determined through experiments also depends on experimental conditions, such as the gap between the two spark electrodes [10], the shape of the spark electrode [15], the criteria for successful ignition, and the size of the ignition vessel. [103]. Another crucial influencing factor of experimentally determined MIE is the stochastic nature of induced ignition [10, 105].

2.4 Stretch Effect and Flame Extinction

In some practical applications of ignition, the flame front often exhibits a curved rather than a perfectly planar geometry (see e.g. [3, 10]). Moreover, in turbulent cases, the flame is also curved and strained due to the flow field [18, 71, 123]. The curvature and strain of the flame front play a crucial role in flame propagation. The concept of flame stretch includes the combined effects of aerodynamic straining and flame curvature. Understanding flame stretch is essential for accurately predicting flame speed and explaining phenomena such as flame extinction and flame front instability [71].

To describe the influence of stretch on flame propagation and extinction, the stretch rate κ is a key parameter. It is defined as the ratio of the temporal rate of change of the flame surface area A for an infinitesimal element to the area itself. [127]:

$$\kappa = \frac{1}{A}\frac{dA}{dt} \tag{2.12}$$

For a premixed laminar outwardly propagating spherical flame, the stretch rate is [71]:

$$\kappa_{sph} = \frac{2}{r_f}\frac{dr_f}{dt} \tag{2.13}$$

And for a premixed laminar outwardly propagating cylindrical flame, the stretch rate is [71]:

$$\kappa_{cyl} = \frac{1}{r_f}\frac{dr_f}{dt} \tag{2.14}$$

The influence of stretch on flame propagation is significantly pronounced in mixtures with unequal thermal and mass diffusivities. The Lewis number expresses a correlation between mass and thermal diffusivities [45, 71]:

$$Le = \frac{\alpha}{D_i} = \frac{\lambda}{D_i \cdot \rho c_p} \tag{2.15}$$

Here, α represents the thermal diffusivity, D_i is the mass diffusivity of the limiting reactant in the mixture, λ is the thermal conductivity, ρ is the density, and c_p is the specific heat capacity at constant pressure.

The stretch effect for a mixture with $Le \neq 1$ can be explained as follows: For a flame with positive flame stretch, the flame area increases. For a mixture with $Le > 1$ (for example, lean iso-octane/air mixture [112] or rich hydrogen/air mixture [52]), the mass diffusion of reactants into the reaction zone is slower than the thermal diffusion out of the reaction zone. This leads to a decrease in flame temperature, subsequently reducing the chemical

reaction rate in the reaction zone. On the contrary, for a mixture with $Le < 1$, the mass diffusion of reactants into the reaction zone exceeds the heat loss through heat conduction, resulting in an increase in flame temperature and increasing chemical reaction rate [71].

2.5 Induced ignition in turbulent flow field

Turbulent flows are prevalent in the operation of most practical combustion engines. Spark ignition in premixed turbulent flow is a common scenario in gasoline engines. The MIE in turbulent premixed flows is therefore a meaningful character of fuel/air mixtures.

In the experiments, turbulent flow can be generated through fans [105]. In simulations of induced ignition within a turbulent flow field, unlike laminar ignition where conditions are well-defined, flow parameters fluctuate across time and space. These fluctuations can significantly increase computational costs. [123].

To classify different combustion regimes based on the interaction between turbulence and the flame, and to guide the simulation of turbulent flames, the Borghi diagram shown in Fig. 2.6 [123] is used. In this diagram, the turbulent velocity fluctuation v', normalized by the laminar flame speed v_L, is plotted against the largest eddy length scale l_0, normalized by the thickness of a laminar flame front l_L. Turbulent Reynolds number R_l, turbulent Damköhler number Da, and turbulent Karlovitz number Ka are used to divide combustion into different zones, with the definitions:

$$R_l = \frac{v' l_0}{\nu}, \tag{2.16}$$

where ν is the kinematic viscosity,

$$Ka = \frac{t_L}{t_K}, \tag{2.17}$$

where $t_L = l_L / v_L$ is the time scale of the laminar flame, t_K is the Kolmogotov time scale, and

$$Da = \frac{t_0}{t_L}, \tag{2.18}$$

where t_0 is the macroscopic time scale.

Combustion with $R_l < 1$ is categorized as laminar flame. For turbulent flame ($R_l > 1$), a flamelet regime is observed below the $Ka = 1$ line [123].

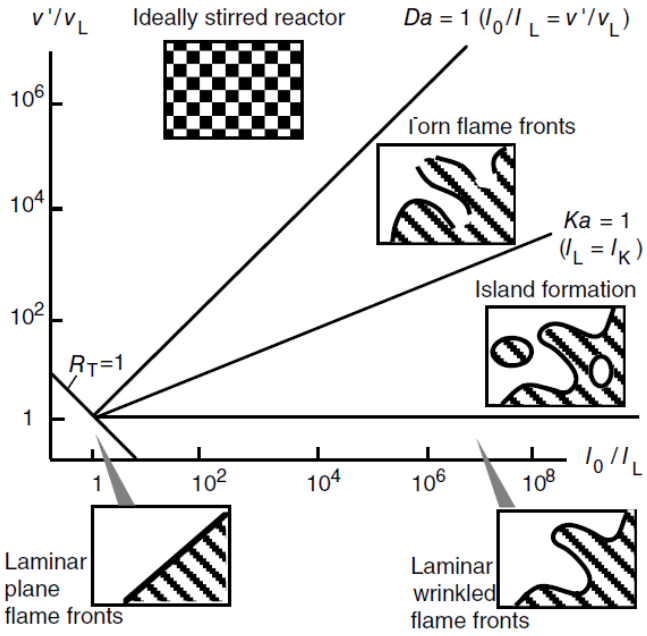

Figure 2.6: Borghi Diagram [123]

Above the $Da = 1$ line, no flame structure is present; it is called a well-mixed reactor. Between the well-mixed reactor zone and the flamelet zone, the flame front is strongly disturbed by the turbulent eddies and is called the distributed reaction zone.

In the flamelet regime of a turbulent flame, the time scale of chemical reactions is faster than the time scale of turbulence. In this case, the turbulent flame front can be treated as a wrinkled and strained laminar flame front, where chemical reactions still take place in a thin reaction sheet that separates the fresh mixture and burnt mixture [19, 94, 108]. The study of a laminar strained flame provides important insights into turbulent flames. In this work, a counterflow configuration is employed, and the detailed mathematical model of the counterflow configuration will be explained in Sec. 3.1.2.

For the case of induced ignition in turbulent flow, uncertainties in the flow field and ignition parameters strongly affect the ignition process. In this work, the strain rate and ignition radius are assumed to follow normal distributions, as was observed in experiments (see e.g. [12]). The possibility of successful ignition is then calculated using a regression method, and the MIE in this case is defined as the ignition energy with a 50% ignitability [10, 53].

In the past, experimental measurements of MIE in turbulent premixed flows were carried out (see e.g. [8, 53, 60]). One common observation is that the MIE increases with increasing turbulence intensity [8, 20, 53, 60]. In the results section, the MIE is estimated using a counterflow flame configuration, and the observed MIE transition in simulations is explained.

3 Mathematical Methods

The induced ignition process is an unsteady combustion process [79]. In this chapter, the mathematical methods of this work are explained. This includes a description of the mathematical model of the instationary combustion process with the simplification of restricting it to a one-dimensional geometry. Additionally, the mathematical models of chemical kinetics and the molecular transport process are also explained in this chapter, as they are necessary for solving the conservation equations.

3.1 Governing equations

In combustion processes, a complex interaction of chemical reactions and transport processes (such as heat conduction and molecular diffusion process) takes place. The mathematical description of chemically reacting flows is accomplished by formulating the conservation equations for total mass, species mass, momentum, and energy. It results in a system of partial differential equations (PDE) that describe the temporal and spatial changes of the variables (e.g. mass fractions w_i of species i, enthalpy h, density ρ, pressure p and velocity $\vec{v}$) caused by chemical reactions, transport processes, and other effects (e.g. radiation, gravity and external ignition energy) [71, 79, 97, 123]. Full description of the three-dimensional conservation equations can be found in e.g. [123].

3.1.1 One-dimensional instationary combustion processes

Induced ignition is an unsteady combustion process. In this work, one-dimensional simulations are employed for the simulation of the spark ignition process in a premixed quiescent mixture as a simplification. In such systems, inhomogeneities occur only in one spatial dimension, allowing the exploitation of symmetry with respect to the other spatial coordinates. In real spark ignition in quiescent mixture, a cylindrical discharge channel forms shortly after ignition; the discharge channel soon acquires a spherical shape with

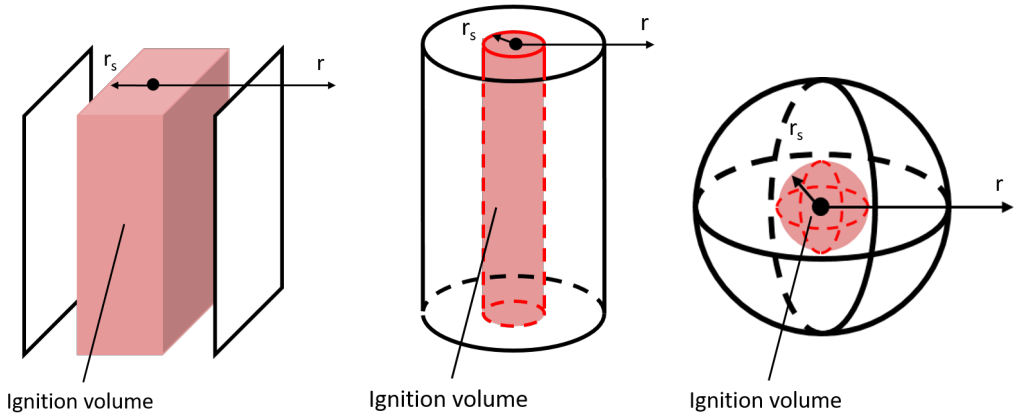

(a) Infinite slab **(b)** Infinite cylinder **(c)** Sphere

Figure 3.1: Schematic of the induced ignition with one-dimensional geometries in quiescent mixture

flat poles at the electrodes and propagates to the fresh mixture [82]. In this study, simulations are conducted mainly with spherically symmetric geometry. Planar geometry and cylindrical geometry are also used to highlight the influence of curvature.

When using one-dimensional simulations, two or three-dimensional effects cannot be fully accounted for. However, valuable insights into the interaction between chemical reactions and transport processes and their impact on the minimum ignition energy can still be gained through one-dimensional simulation. Nevertheless, certain 3D effects, such as buoyancy and their influence on the ignition process, will be briefly discussed in the results sections.

Fig. 3.1 shows schematics of the induced ignition with one-dimensional geometries in a quiescent mixture. External energy is deposited into the ignition volume at the center with an ignition radius r_s for the ignition duration τ_s. After τ_s, the ignition source is shut down, and the flame front with a flame radius r_f propagates from the center to the outer boundary along one spatial coordinate r.

Another crucial simplification in this work is the assumption of constant pressure, which assumes that the increase in pressure propagates infinitely fast in space, and a spatially constant pressure exists in the calculation domain.

It could be shown that this assumption is a very good approximation for many cases (see e.g. [46, 80]).

To eliminate the convective terms in the conservation equations and automatically satisfy the continuity equation, a Lagrangian coordinate transformation $(t, r) \rightarrow (t, \psi)$ is applied, where t denotes time, r represents the physical spatial radius, and ψ denotes the Lagrangian coordinate [79, 80]:

$$\left(\frac{\partial \psi}{\partial r}\right)_t = \rho r^\alpha \tag{3.1}$$

Here ρ is the density and α denotes the geometry. For planar geometry, $\alpha = 0$; for cylindrical geometry, $\alpha = 1$; for spherical geometry, $\alpha = 2$.

Another benefit of using the Lagrangian coordinate is that, as the Lagrangian coordinate ψ is proportional to the mass of the burnt gas, it serves as a better parameter for observing flame propagation caused by chemical reactions compared to the traditional definition of flame radius using spatial coordinates, as outlined in Section 2.1. This can be explained as follows: In the case of pure thermal expansion where no chemical reaction takes place, the flame front still moves away from the center, leading to an increase in the flame radius r_f defined with spatial coordinates. However, since the mass of the burnt gas remains constant in this scenario, the Lagrangian coordinate ψ doesn't change. ψ only increases when chemical reactions occur and more fresh mixture is burnt. In this work, the cubic root of ψ_{r_f}, representing the Lagrangian coordinate at the flame front, is employed as a spatial indicator of flame propagation.

After restricting the simulation to one-dimensional cases, applying the constant pressure assumption, and transforming into Lagrangian coordinates, the governing conservation equations can be expressed as follows [46, 79, 80]:

$$\frac{\partial \psi}{\partial r} - \rho r^\alpha = 0 \tag{3.2}$$

$$\frac{\partial p}{\partial \psi} = 0 \tag{3.3}$$

$$\frac{\partial T}{\partial t} - \frac{1}{\rho c_p}\frac{\partial p}{\partial t} - \frac{1}{c_p}\frac{\partial}{\partial \psi}\left(\rho r^{2\alpha}\lambda \frac{\partial T}{\partial \psi}\right) + \frac{r^\alpha}{c_p}\sum_{i=1}^{n_s}\rho c_{pi} j_i \frac{\partial T}{\partial \psi} + \frac{1}{\rho c_p}\sum_{i=1}^{n_s}\dot{\omega}_i h_i M_i = \frac{\dot{q}}{\rho c_p} \tag{3.4}$$

$$\frac{\partial w_i}{\partial t} + \frac{\partial}{\partial \psi}(\rho r^\alpha j_i) - \frac{\dot{\omega}_i M_i}{\rho} = 0 \tag{3.5}$$

where t is time, ψ is Lagrangian coordinate, r is radius, T is temperature, α denotes the geometry (0 for infinite slab, 1 for infinite cylinder and 2 for sphere), ρ is density, c_p is specific constant pressure heat capacity of the mixture, c_{pi} is specific constant pressure heat capacity of species i, w_i is mass fraction of species i, h_i is enthalpy of species i, M_i is molar mass of species i. j_i is the diffusion term of species i and will be explained in Sec. 3.3. $\dot{\omega}_i$ is the chemical production/consumption rate of species i and will be explained in Sec. 3.2.

The initial condition of the simulation is a premixed quiescent fuel/air mixture with a pre-defined mixture composition:

$$w(r,t=0) = w_i \tag{3.6}$$

$$T(r,t=0) = T_0 \tag{3.7}$$

The boundary conditions include symmetry at the center and a non-catalytic, adiabatic outer boundary:

Inner boundary at $r = 0$:

$$\frac{\partial T}{\partial \psi} = 0 \tag{3.8}$$

$$\frac{\partial w_i}{\partial \psi} = 0 \tag{3.9}$$

Outer boundary at $r = L$ (where L is the size of the calculation domain):

$$\frac{\partial T}{\partial \psi} = 0 \tag{3.10}$$

$$\frac{\partial w_i}{\partial \psi} = 0 \tag{3.11}$$

For the case of induced ignition, $\dot{q}$ denotes the artificial energy source [79]. Based on experimental source profiles of similar ignition processes, the external source term with an power density $\dot{q} = \dot{q}(r,t)$ is set to have an exponential form [80], as is shown in Fig. 3.2:

$$\dot{q} = \begin{cases} \dot{q}_{max} e^{-\left(\frac{r}{r_s}\right)^8} & , \quad 0 < t \leq \tau_s \\ 0 & , \quad t > \tau_s \end{cases} \tag{3.12}$$

For an infinity slab, as is shown in Fig. 3.1(a), the ignition energy is expressed in terms of energy per unit area, with the unit J/m^2:

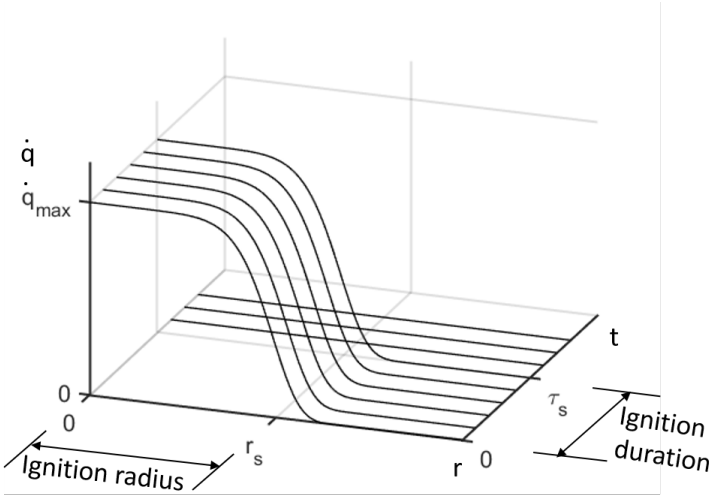

Figure 3.2: Spatial and temporal profile of external power density

$$\begin{aligned} E_{ig} &= \int_0^{\tau_s} \int_0^{\infty} \dot{q} dr dt \\ &= \Gamma(\frac{9}{8}) \cdot \tau_s \cdot r_s \cdot \dot{q}_{max} \\ &= 0.9417 \cdot \tau_s \cdot r_s \cdot \dot{q}_{max} \end{aligned} \tag{3.13}$$

For an infinity cylinder, as is shown in Fig. 3.1(b), the ignition energy is expressed in terms of energy per unit area, with the unit J/m:

$$\begin{aligned} E_{ig} &= \int_0^{\tau_s} \int_0^{\infty} (2\pi r) \dot{q} dr dt \\ &= \Gamma(\frac{5}{4}) \cdot \tau_s \cdot \pi r_s^2 \cdot \dot{q}_{max} \\ &= 0.9064 \cdot \tau_s \cdot \pi r_s^2 \cdot \dot{q}_{max} \end{aligned} \tag{3.14}$$

For a sphere, as is shown in Fig. 3.1(c), the ignition energy is expressed with the unit J:

$$\begin{aligned} E_{ig} &= \int_0^{\tau_s} \int_0^{\infty} (4\pi r^2) \dot{q} dr dt \\ &= \Gamma(\frac{3}{2}) \cdot \tau_s \cdot \frac{4}{3} \pi r_s^3 \cdot \\ &= 0.8862 \cdot \tau_s \cdot \frac{4}{3} \pi r_s^3 \cdot \dot{q}_{max} \end{aligned} \tag{3.15}$$

The Gamma function arises from the integral of energy density across various ignition geometries.

Model simulations of flame initiation and early flame propagation are conducted using the in-house code INSFLA [80]. This code solves the aforementioned Navier-Stokes equations using implicit time stepping with error control, computing the temporal evolution of combustion processes in one-dimensional geometries. An automatic adaptive mesh algorithm is applied to ensure sufficient grid points in the thin reaction zone, while fewer grid points are allocated to regions with low gradients. The grid point distribution is updated after each time step. It considers detailed chemistry. The transport model used in the simulation is the detailed transport model, which also includes thermal diffusion. Running the code provides spatiotemporal profiles of temperature and species mass fractions.

3.1.2 Unsteady combustion process in counterflow configurations

Fig. 3.3 illustrates a schematic of induced ignition for a strained axisymmetric counterflow premixed laminar flame. Here, r and z represent cylindrical coordinates that are tangential and normal to the flame, respectively. The inlets at both boundaries feature fresh premixed fuel/air mixtures with identical states, including mixture composition, temperature T_u, pressure p, and absolute flow velocity. At time $t = 0$, external energy is deposited at the center. The artificial energy source term with a power density $\dot{q} = \dot{q}(z,t)$ has an exponential form [80]:

$$\dot{q} = \begin{cases} \dot{q}_{max} e^{-\left(\frac{z}{z_s}\right)^8} & , \quad 0 < t \leq \tau_s \\ 0 & , \quad t > \tau_s \end{cases} \tag{3.16}$$

where z_s is the ignition radius, and τ_s is the ignition duration. The detailed description and spatial-temporal profile of the artificial energy source term can be found in Sec. 3.1.1.

Stahl and Warnatz [108] proposed that the combustion system, when represented in two-dimensional spatial coordinates (z-axis and r-axis), can be described by a system of partial differential equations for the variables along only one spatial coordinate (z-axis). This formulation relies on the assumption that temperature, species mass fractions, and axial velocity depend solely on z, and involves two independent parameters: the tangential pressure gradient J and the radial velocity gradient G [108]:

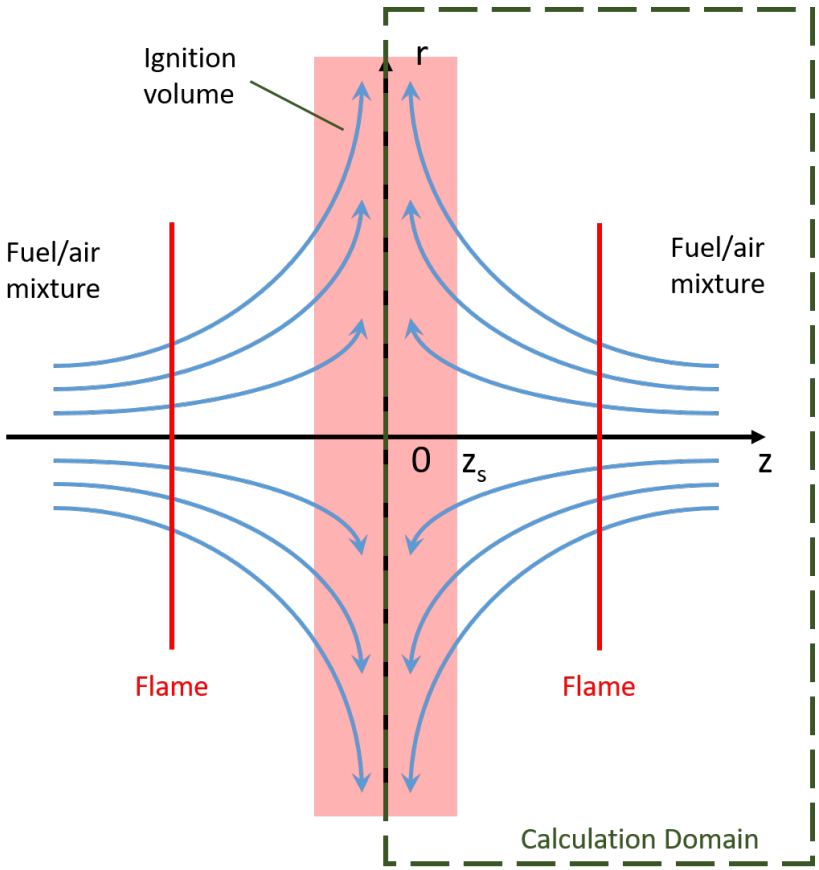

Figure 3.3: Schematic of the induced ignition in counterflow configuration

$$J = -\frac{1}{r}\frac{\partial p}{\partial r} \tag{3.17}$$

where p is the pressure, and

$$G(z,t) = \frac{v_r(z,t)}{r} \tag{3.18}$$

where v_r is the radial velocity.

The conservation equations in this case are as follows, according to [108]:

$$\frac{\partial \rho}{\partial t} + 2\rho G + \frac{\partial(\rho v_z)}{\partial z} = 0 \tag{3.19}$$

$$\frac{\partial G}{\partial t} + \frac{J}{\rho} + G^2 - \frac{1}{\rho}\frac{\partial}{\partial z}\left(\mu\frac{\partial G}{\partial z}\right) + v_z\frac{\partial G}{\partial z} = 0 \tag{3.20}$$

$$\frac{\partial v_z}{\partial t} + \frac{1}{\rho}\frac{\partial p}{\partial z} + \frac{4}{3\rho}\frac{\partial}{\partial z}(\mu G) - \frac{2\mu}{\rho}\frac{\partial G}{\partial z} - \frac{4}{3\rho}\frac{\partial}{\partial z}\left(\mu\frac{\partial v_z}{\partial z}\right) + v_z\frac{\partial v_z}{\partial z} = 0 \quad (3.21)$$

$$\frac{\partial T}{\partial t} - \frac{1}{\rho}\frac{\partial p}{\partial t} - \frac{1}{\rho c_p}\frac{\partial}{\partial z}\left(\lambda\frac{\partial T}{\partial z}\right) + \frac{1}{\rho c_p}\frac{\partial T}{\partial z}\sum_{i=1}^{n_s} c_{pi} j_{i,z} + \frac{1}{\rho c_p}\sum_{i=1}^{n_s}\dot{\omega}_i h_i M_i + v_z\frac{\partial T}{\partial z} = 0 \quad (3.22)$$

$$\frac{\partial w_i}{\partial t} + \frac{1}{\rho}\frac{\partial}{\partial z}(j_{i,z}) - \frac{\dot{\omega}_i M_i}{\rho} + v_z\frac{\partial w_i}{\partial z} = 0 \quad (3.23)$$

where t is time, T is temperature, p is the pressure, ρ is density, v_z is the normal velocity, c_p is specific constant pressure heat capacity of the mixture, c_{pi} is specific constant pressure heat capacity of species i, w_i is mass fraction of species i, M_i is molar mass of species i. j_i,z is the diffusion term of species i along z direction and will be explained in Sec. 3.3. $\dot{\omega}_i$ is the chemical production/consumption rate of species i and will be explained in Sec. 3.2.

Since the system is symmetric about the r-axis, the calculation domain is restricted to the positive domain of the z-axis, with the origin of the z-axis set at the symmetric center (stagnation point). The strain rate of the flame in this case is [108]:

$$a = \sqrt{-\frac{J}{\rho_u}} \quad (3.24)$$

where ρ_u denotes the density of the unburnt mixture.

In this case, the initial condition is that all thermo-kinetic state variables including T, p, and w_i for all species are homogeneously distributed across the entire spatial domain of the system:

$$T(r, t = 0) = T_0, \qquad p(r, t = 0) = p_0, \qquad w_i(r,t = 0) = w_{i,0} \quad (3.25)$$

The left boundary corresponds to the center of symmetry (z = 0) with Neumann boundary conditions for T and w_i for all species. The normal velocity v_z is zero at the left boundary (stagnation point):

$$v_z = 0, \qquad \frac{\partial T}{\partial z} = 0, \qquad \frac{\partial w_i}{\partial z} = 0 \quad (3.26)$$

The right boundary represents the unburnt mixture far away from the center, with Dirichlet boundary conditions for T and w_i for all species:

$$v_z(t) = v_{z,nz}(t), \qquad T(t) = T_{ub}(t), \qquad w_i(t) = w_{i,ub}(t) \quad (3.27)$$

3.2 Chemical Kinetics

To solve the Navier-Stokes equations described in Sec. 3.1, information about chemical kinetics is required. The source term in the species mass conservation equation represents the formation or consumption of species i due to chemical reactions [79, 123]:

$$\dot{\omega}_i = \left(\frac{\partial c_i}{\partial t}\right)_{chem} \tag{3.28}$$

where c_i denotes the concentration of species i. $\dot{\omega}_i$ can be calculated when the reaction mechanism of the fuel is provided.

3.2.1 Rate law and reaction mechanisms

For detailed chemical kinetic analysis, relying on a single global reaction is nearly impossible. In such cases, intermediates formed during the reaction are neglected, the reaction order is not constant, and the rate law becomes too complex to determine. Instead, the processes occurring in chemically reacting systems can be described by a set of elementary reactions, which occur directly at the molecular level [111, 123].

In elementary reactions, the molecularity of the reaction corresponds to the reaction order. Depending on whether one, two, or three reactant molecules are involved in the elementary reaction, it is classified as a unimolecular, bimolecular, or trimolecular reaction. The rate law for a unimolecular, bimolecular, and trimolecular reaction is then first, second, and third order, respectively. Reactions with molecularity higher than three are very unlikely and is never observed in experiments [123].

For an elementary reaction r given by [71, 123]

$$\sum_{s=1}^{S} v_{rs}^{(e)} A_s \xrightarrow{k_r} \sum_{s=1}^{S} v_{rs}^{(p)} A_s \tag{3.29}$$

Here, A_s represents the species symbol, S denotes the total number of species involved in the reaction, k_r is the rate coefficient of reaction r, and $v_{rs}^{(e)}$ and $v_{rs}^{(p)}$ denote the stoichiometric coefficients of the reactants and products, respectively.

The production rate of species i through reaction r is then [123]

$$\left(\frac{\partial c_i}{\partial t}\right)_{\text{chem,r}} = k_r (v_{ri}^{(p)} - v_{ri}^{(e)}) \prod_{s=1}^{S} c_s^{v_{rs}^{(e)}} \tag{3.30}$$

where c_i is the concentration of the species i.

k_r represents the rate coefficient of reaction r. It exhibits strong dependence on temperature, and for certain reactions, it is additionally influenced by pressure [123]. The temperature dependence of k_r is described by a modified Arrhenius law [71, 123]:

$$k_r(T) = A_r T^{b_r} \cdot \exp\left(-\frac{E_{a,r}}{RT}\right) \tag{3.31}$$

with R representing the universal gas constant, A_r representing the pre-exponential factor, b_r representing the temperature exponent, and $E_{a,r}$ representing the activation energy of reaction r, which corresponds to the minimum energy required for reactants to undergo the chemical reaction. The parameters in the Arrhenius law are often determined with experiments [71].

The exponential factor in the Arrhenius equation $\exp(-E_{a,r}/RT)$ represents the fraction of reactants that have approached the activation energy barrier. The reaction rate is more sensitive to changes in temperature when the activation energy of the reaction is higher [71].

As mentioned before, the rate coefficient k_r may also depend on pressure. In uni- and trimolecular reactions, complex sequences of reactions are treated as elementary reactions. The reaction sequence can be explained using the simplified Lindemann mechanism [123].

A molecule requires energy to break its bond, which it receives through a non-reactive collision. The energy supplied causes excitation within the molecule, allowing it to decompose into products. Since the concentration of collision partners in unimolecular decomposition reactions depends on pressure, this explains the characteristic dependence on pressure. At high pressures, the reactions follow first-order kinetics. Sufficient activating collisions occur, making the molecule's decomposition rate the determining factor. At low pressures, and therefore low concentrations of collision partners, the rate-limiting step for the reaction is the collision. The reaction then follows second-order kinetics [71, 123].

For a detailed chemical kinetic analysis, all occurring elementary reactions must be considered. For large hydrocarbon fuels, the detailed reaction mechanism may include too many elementary reactions, resulting in enormous computational costs. In such cases, semi-detailed chemical mechanisms with simplifications are developed and then validated against detailed reaction mechanisms and experimental data. For example, a detailed reaction mechanism for n-heptane developed by Curran et al., which is well-known as the LLNL-Mechanism, consists of 550 species and several 2450 elementary reactions [30]; A semi-detailed reaction mechanism for toluene reference fuel

(including the mechanism of n-heptane) developed by Andrae et al. consists of only 137 species and 633 reactions [5].

A reaction mechanism includes chain initiation reactions, chain propagation reactions, chain branching reactions, and chain termination reactions.

- In chain initiation reactions, reactive intermediate species are produced.
- In chain propagation reactions, a reactive species reacts and forms a new reactive species, while the number of reactive species remains constant.
- In chain branching reactions, the reaction of a reactive species forms two new reactive species.
- In chain termination reactions, reactive species are consumed, resulting in the formation of stable species.

3.2.2 Oxidation of Methane

The oxidation of methane is important in two ways. On the one hand, methane itself can be used as a fuel for, e.g., motor vehicles [125]. On the other hand, there is a similarity in the oxidation process for all aliphatic fuels: they all break down to C1 and C2 radicals initially, followed by further oxidation of these radicals. In other words, the oxidation of hydrocarbon fuels is hierarchical, with the oxidation of larger fuels containing sub-mechanisms of smaller fuels. Consequently, the oxidation of CH_4 is crucial for studying all aliphatic hydrocarbon fuels [71, 123].

The oxidation of methane in a flame starts with abstraction of hydrogen by H, O, and OH radicals, resulting in the formation of methyl radical (CH_3). The CH_3 radical is primarily consumed by oxygen atoms, forming CH_2O. Subsequently, with further hydrogen abstraction, the CHO radical is formed, which then decomposes into CO and H or undergoes abstraction of hydrogen by H or O_2. In stoichiometric or rich mixtures, recombination of CH_3 also occurs, forming C_2H_6.

3.2.3 Oxidation of Large Hydrocarbon Fuels

The reaction pathway of hydrocarbon fuels depends on the conditions under which the combustion process takes place. Different radicals and reactions dominate the reaction mechanism at high, intermediate, and low temperature ranges. Due to different reaction pathways at different temperatures, phenomena like cool flame and negative temperature coefficient (NTC) behaviors can be observed.

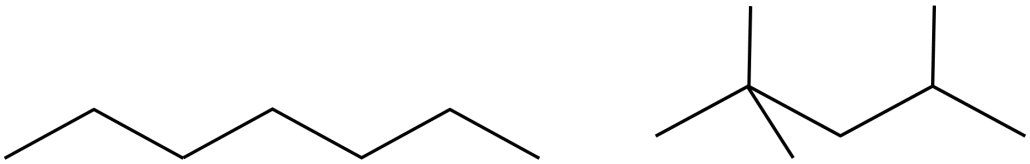

(a) n-heptane **(b)** iso-octane

Figure 3.4: Chemical structure of n-heptane and iso-octane

High Temperature Oxidation

At high temperature range (normally $T > 1100\,\mathrm{K}$ at 1 atm), the dominant chain branching reaction in hydrocarbon oxidation is the reaction of hydrogen atom radical (H•) with oxygen (O_2) to form an oxygen radical (•O•) and a hydroxyl radical (OH•) [11, 71, 123]:

$$\mathrm{H\bullet} + \mathrm{O_2} \longrightarrow \mathrm{\bullet O\bullet} + \mathrm{OH\bullet}$$

This reaction highlights the significance of hydrogen atom radicals in chain branching. Kinetic processes that increase the H• concentration accelerate the entire oxidation reaction [126].

The reaction pathway of hydrocarbon fuels at high temperatures is similar: H atom abstraction serves as the initial step, resulting in the formation of alkyl radical R• [11, 30, 71, 123]:

$$\mathrm{RH} + \mathrm{H\bullet}, \mathrm{\bullet O\bullet}, \mathrm{OH\bullet} \longrightarrow \mathrm{R\bullet} + \mathrm{H_2}, \mathrm{OH\bullet}, \mathrm{H_2O}$$

The H atom abstraction is followed by β-decomposition, where the formed alkyl radicals decomposes to smaller alkyl radical •R' [11, 30, 71, 123]:

$$\mathrm{R'{-}CH_2{-}\overset{\bullet}{C}H{-}R''} \longrightarrow \mathrm{\bullet R'} + \mathrm{CH_2{=}CH{-}R''}$$

The alkyl radicals continue to decompose until methyl and ethyl radicals are formed. This reduces the problem to the oxidation of methyl and ethyl radicals, which also represents the rate-limiting process in the oxidation of aliphatic hydrocarbon fuels [80]. The main product of the alkyl decomposition of straight-chain alkanes (e.g. n-heptane in Fig. 3.4(a)) is C_2H_5, and the main product of the alkyl decomposition of branched-chain alkanes (e.g. iso-octane in Fig. 3.4(b)) is CH_3 [39, 81].

For the oxidation of aliphatic hydrocarbons at high temperatures, the reaction between carbon monoxide (CO) and hydroxyl radicals (OH•)

$$\mathrm{CO} + \mathrm{OH}\bullet \longrightarrow \mathrm{CO_2} + \mathrm{H}\bullet$$

is responsible for a significant portion of the heat release and represents the second most sensitive reaction, making it rate-limiting [123].

Intermediate Temperature Oxidation

At intermediate temperatures ($900\,\mathrm{K} < T < 1100\,\mathrm{K}$), the hydroperoxy radical ($\mathrm{HO_2}\bullet$) plays an important role instead of $\mathrm{OH}\bullet$. This is because the large activation energy of the dominant reaction ($\mathrm{H}\bullet + \mathrm{O_2} \longrightarrow \mathrm{OH}\bullet + \mathrm{O}\bullet$) at high temperatures causes it to proceed slowly within the intermediate temperature range [39, 123].

The $\mathrm{HO_2}\bullet$ radical is initially produced through:

$$\mathrm{RH} + \mathrm{O_2} \longrightarrow \mathrm{R}\bullet + \mathrm{HO_2}\bullet$$

the formed $\mathrm{HO_2}\bullet$ radical attacks the alkane molecule and produces the alkyl radical through and allow chain-branching reaction:

$$\begin{aligned} \mathrm{HO_2}\bullet + \mathrm{RH} &\longrightarrow \mathrm{H_2O_2} + \mathrm{R}\bullet \\ \mathrm{H_2O_2} + \mathrm{M} &\longrightarrow \mathrm{OH}\bullet + \mathrm{OH}\bullet + \mathrm{M} \end{aligned}$$

More $\mathrm{HO_2}\bullet$ can be formed through

$$\begin{aligned} \mathrm{OH}\bullet + \mathrm{H_2} &\longrightarrow \mathrm{H_2O} + \mathrm{H}\bullet \\ \mathrm{H}\bullet + \mathrm{O_2} + \mathrm{M} &\longrightarrow \mathrm{HO_2}\bullet + \mathrm{M} \end{aligned}$$

Low Temperature Oxidation

If the oxidation takes place at a temperature lower than 900 K, both the β decomposition and the decomposition of $\mathrm{H_2O_2}$ would be too slow, and another reaction mechanism dominates the oxidation. In this case, peroxide radicals play an important role [29, 30, 123]. The first step of the oxidation is the formation of peroxide radicals through the reaction:

$$\mathrm{R}\bullet + \mathrm{O_2} \longrightarrow \mathrm{RO_2}\bullet$$

This can be followed by the H-atom abstraction from another alkane molecule and chain-branching reaction [29, 30, 123]:

$$\begin{aligned} \mathrm{RO_2}\bullet + \mathrm{RH} &\longrightarrow \mathrm{ROOH} + \mathrm{R}\bullet \\ \mathrm{ROOH} &\longrightarrow \mathrm{RO}\bullet + \mathrm{OH}\bullet\,, \end{aligned}$$

or the isomerization (internal H-atom abstraction) and chain propagation [29, 30, 123]:

$$\begin{aligned} RO_2\bullet &\longrightarrow \bullet QOOH \\ \bullet QOOH &\longrightarrow QO + OH\bullet \end{aligned}$$

Because the internal collision rate is faster than the external collision, the isomerization of $RO_2\bullet$ dominates [123]. This is followed by repeated O_2 addition, isomerization, and chain branching [30, 123]:

$$\begin{aligned} \bullet QOOH + O_2 &\longrightarrow \bullet O_2QOOH \\ \bullet O_2QOOH &\longrightarrow HO_2UO_2H \\ HO_2UO_2H &\longrightarrow HO_2UO + OH\bullet \\ HO_2UO &\longrightarrow OUO\bullet + OH\bullet \end{aligned}$$

The low-temperature oxidation depends strongly on the molecule structure of the alkanes. In general, low-temperature oxidation of straight-chain alkanes (e.g., n-heptane) is stronger than that of branched-chain alkanes (e.g., iso-octane). The reason is that the intermediate rings formed during the internal H-atom abstraction for iso-octane are more compact than those for n-heptane, resulting in higher ring strain energy [123, 135]. Another reason is that, a large proportion of H atoms in straight-chain alkanes are secondary H atoms, whose bond energy is much smaller than primary H atoms, which are the large proportion of in branched alkanes. This means that internal H-abstraction in straight-chain alkanes is easier than in branched alkanes, resulting in faster low-temperature oxidation of straight-chain alkanes than of branched-chain alkanes [123, 126].

Fig. 3.5 shows the ignition delay time (IDT) of stoichiometric n-heptane/air and iso-octane/air mixtures at atmospheric pressure. At high temperature range, the IDT of both mixtures almost coincide, which is also observed in experiments(see e.g. [59]). Due to the faster low-temperature chemistry of n-heptane compared to iso-octane, the IDT of n-heptane in the low-temperature range is much smaller than that of iso-octane. Moreover, the negative temperature coefficient (NTC) behavior of both fuels can be clearly observed in Fig. 3.5. The reason for the NTC behavior is that in the intermediate temperature range (at 1 bar, for n-heptane from about 650 K to about 800 K and for iso-octane from about 620 K to about 720 K), as the temperature increases, the reaction rate of the reverse reaction of $R\bullet + O_2 \longrightarrow RO_2,\bullet$ increases rapidly. This causes the $RO_2,\bullet$ radicals to decompose back into the alkyl radical $R\bullet$, resulting in a decrease in the concentration of $RO_2,\bullet$ radicals. Consequently, the chain-branching reactions slow down, and the overall reaction rate decreases.

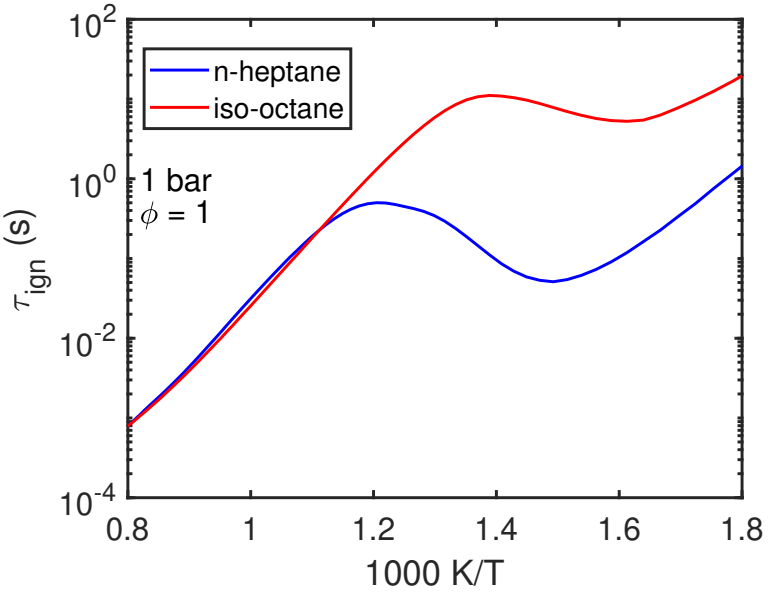

Figure 3.5: Ignition delay time of stoichiometric n-heptane/air and iso-octane/air mixtures at atmospharic pressure

3.2.4 Oxidation of Ammonia

The oxidation of ammonia begins with the H-atom abstraction in which ammonia is consumed by reacting with the H, O, OH, resulting in the formation of $NH_2\bullet$ radical [58, 104].

$$NH_3 + H\bullet \longrightarrow NH_2\bullet + H_2$$

$$NH_3 + \bullet O\bullet \longrightarrow NH_2\bullet + OH\bullet$$

$$NH_3 + OH\bullet \longrightarrow NH_2\bullet + H_2O \cdot$$

The formed amidogen radicals can either be consumed via another H-atom abstraction reaction to form the $NH\bullet$ radical, or they can be consumed via reaction with O to form the nitroxyl radical, which is one of the most important intermediates in the reaction pathway leading to NO pollution [4, 58, 65, 104]

$$NH_2 + O\bullet \longrightarrow HNO + H\bullet$$

According to Miller et al. [58], in lean mixtures, molecular nitrogen is primarily formed though reaction

$$\begin{aligned} \mathrm{NH^{\bullet} + NO} &\longrightarrow \mathrm{N_2O + H^{\bullet}} \\ \mathrm{N_2O + H^{\bullet}} &\longrightarrow \mathrm{N_2 + OH^{\bullet}} \end{aligned}$$

In rich mixtures, molecular nitrogen is mainly formed though [58, 104]

$$\begin{aligned} \mathrm{NH^{\bullet} + H^{\bullet}} &\longrightarrow \mathrm{N^{\bullet} + H_2} \\ \mathrm{N^{\bullet} + NO} &\longrightarrow \mathrm{N_2 + O^{\bullet}} \end{aligned}$$

Because the oxidation of ammonia is very slow, combustion enhancers like hydrogen or hydrocarbons are sometimes added to improve ignition and flame propagation. By combining the mechanism of ammonia oxidation with those of hydrogen or hydrocarbons, it is possible to conduct numerical studies on ammonia blends.

Unlike methane and hydrogen, whose reaction pathways are well-known, the oxidation mechanism of ammonia is not yet well understood. Existing mechanisms for ammonia still struggle to accurately reproduce flame characteristics observed in experiments [4]. Further experimental and numerical studies of ammonia flames are necessary to gain a better understanding of the ammonia oxidation process.

3.3 Molecular Transport

To solve the Navier-Stokes equations described in Sec. 3.1, information about the molecular transport processes (e.g. diffusion and heat conduction) is required.

3.3.1 Mass flux

The mass flux density j_i in the conservation equation consists of three parts: the mass transport caused by concentration gradients, temperature gradients, and pressure gradients [123]:

$$j_i = j_{i,d} + j_{i,T} + j_{i,p} \tag{3.32}$$

In the case of mass diffusion caused by concentration gradients, according to Fick's law [50, 123]:

$$j_{i,d} = -\rho D_i^M \mathrm{grad} w_i \tag{3.33}$$

where ρ is the density, w_i is the mass fraction of species i, and D_i^M is the effective diffusion coefficient of species i, given by [50, 123]:

$$D_i^M = \frac{1 - w_i}{\sum_{j \neq i} \frac{x_j}{D_{ij}}} \tag{3.34}$$

where x_j is the mole fraction of species j, and D_{ij} are the binary diffusion coefficients.

In the case of thermal diffusion, which is also called Soret effect, the diffusion flux is given by [50, 123]

$$j_{i,T} = -\frac{D_i^T}{T} \frac{\partial T}{\partial z} \tag{3.35}$$

For the case where no significant pressure gradient exists, the mass transport caused by pressure gradients can be neglected [50, 123]. The total mass flux density is then:

$$j_i = -\rho D_i^M \operatorname{grad} w_i - \frac{D_i^T}{T} \frac{\partial T}{\partial z} \tag{3.36}$$

For curved geometries (spherical or cylindrical), the curvature effect, which might cause flame extinction [69], results from enhanced diffusion compared to planar geometry. This can be explained briefly with the diffusion term of the species mass conservation equation, which is $\frac{1}{r^\alpha} \frac{\partial}{\partial r}(r^\alpha j_i)$, with α indicating the constant for the geometry. In the case of spherical geometry, this term can be expressed as:

$$\frac{1}{r^2} \frac{\partial}{\partial r}(r^2 j_i) = \frac{\partial}{\partial r}(j_i) + \frac{2}{r} j_i \tag{3.37}$$

whereas for planar geometry, this term is simply $\frac{\partial}{\partial r}(j_i)$. The additional term $\frac{2}{r} j_i$ only exists for curved geometry. In the result sections, the influence of the curvature effect on ignition processes will be discussed.

3.3.2 Heat flux

Just like the mass flux density, the heat flux density j_q also consists of three parts:

$$j_q = j_{q,c} + j_{q,d} + j_{q,D} \tag{3.38}$$

where $j_{q,c}$ denotes the heat flux density caused by temperature gradient, $j_{q,d}$ denotes the heat flux density caused by the specific enthalpy of species

mass diffusion, and $j_{q,D}$ denotes the heat flux density caused by the species concentration gradient.

According to Fourier law of heat conduction [50, 123]

$$j_{q,c} = -\lambda \mathrm{grad}\, T \tag{3.39}$$

where λ is the thermal conductivity.

The heat flux density caused by the specific enthalpy of species mass diffusion is

$$j_{q,d} = \sum_i h_i j_i \tag{3.40}$$

and the Dufour effect can be neglected in combustion processes [123].

In simulations, essential parameters for calculating molecular transport, such as thermal conductivity and the diffusion matrix of species, are provided as input. In this study, a detailed transport model, including the Soret effect, was employed. By incorporating the chemical mechanism, initial and boundary conditions, the Navier-Stokes equations were solved. The resulting temporal and spatial development of temperature and species mass fractions can then be used for further investigation of the underlying physics.

4 Induced Ignition of Methane

As mentioned in Sec. 3.2, methane is the primary component of natural gas, comprising 85% to 99% of the total volume [125]. As the smallest hydrocarbon fuel, the chemical kinetics of methane are simpler than those of higher hydrocarbon fuels. This makes methane an excellent starting point for studying the induced ignition of hydrocarbon fuels.

There exist several oxidation mechanisms for methane/air flames that have a good agreement with experiments for IDT and laminar flame speed data (e.g. [6, 107, 115, 124]). In this work, the induced ignition and early flame propagation process of methane was numerically investigated using the well-known GRI 3.0 mechanism, which comprises 53 species and 325 elementary reactions [107]. This mechanism can be used over a wide range of conditions (1000 to 2500 K, 10 Torr to 10 atm, and equivalence ratios from 0.1 to 5 [107]), and it is widely employed for numerical investigations of methane flames [144].

4.1 Flame Scenarios

As previously mentioned, minimum ignition energy (MIE) is a key characteristic of the induced ignition process. For the numerical investigation of induced ignition process, an accurate definition of MIE is necessary. To achieve this, it is necessary to examine the possible scenarios following ignition and then define MIE based on these scenarios.

Fig. 4.1 shows the possibilities after the deposition of external energy. The ignition kernel has a spherically symmetrical geometry with an ignition radius of $r_s = 1.0\,\mathrm{mm}$. During the ignition duration ($\tau_s = 0.1\,\mathrm{ms}$), the fresh mixture in the ignition volume is heated, resulting in an increase in temperature within the ignition volume. Both temperature and $w_{\mathrm{CO_2}}$ profiles ($w_{\mathrm{CO_2}} = m_{\mathrm{CO_2}}/m_{total}$) are shown to describe the flame scenarios. Temperature is a direct indicator of heat release and influences the reaction rate. However, during the early phases of flame propagation, temperature can also be affected by external energy sources. This makes it challenging to determine whether a temperature increase is due to chemical reactions or external energy deposition.

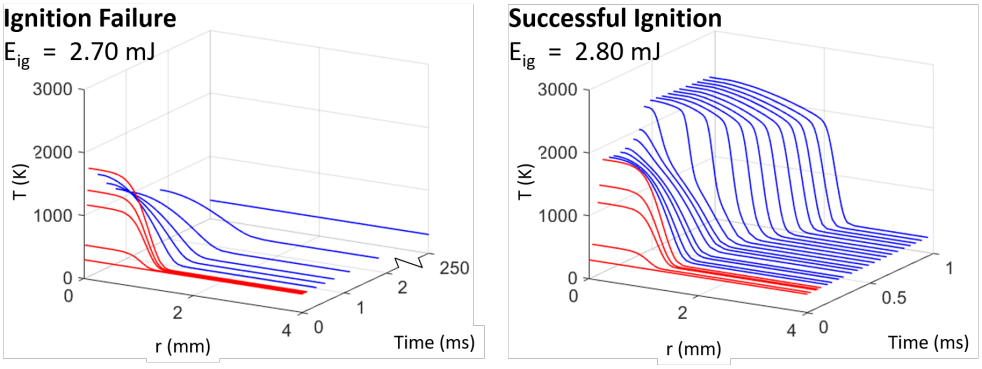

(a) Temperature profile

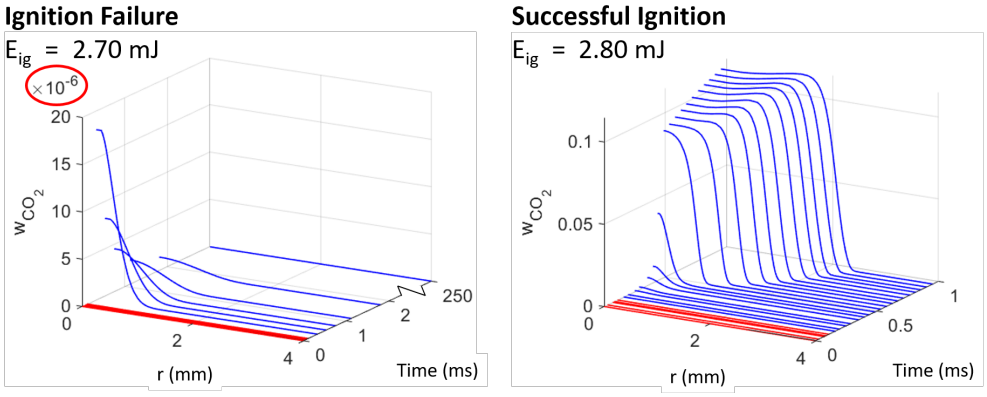

(b) CO_2 mass fraction profile

Figure 4.1: The spatio-temporal profile of temperature and CO_2 mass fraction for the case with ignition failure and the case with successful ignition in simulations under atmospheric conditions. Red lines represent temperatures and CO_2 mass fractions within the spark duration, blue lines represent temperatures and CO_2 mass fractions after the spark duration, $\phi = 1$, $T_0 = 298$ K, $p = 1$ bar, with spherical geometry, $r_s = 1.0$ mm, $\tau_s = 0.1$ ms

CO_2 is significantly produced only in the case of rapid chemical reactions; thus, massive CO_2 formation typically indicates the formation of a flame kernel.

In the case of ignition failure with an ignition energy of $E_{ig} = 2.70\,\mathrm{mJ}$, the temperature in the center of the ignition volume starts decreasing after ignition duration. After about 0.25 ms, the temperature in the entire computational domain returns to 298 K, with no sign of formation of a flame kernel.

On the other hand, if the ignition energy is 0.1 mJ higher than in the case of ignition failure, as can be observed in Fig. 4.1 (b), the temperature in the ignition volume remains almost constant for several milliseconds after ignition energy deposition, and then rapidly increases to about 2500 K due to successful ignition, while massive formation of CO_2 can be observed ($w_{CO_2,max}$ about 5000 times larger than the case of ignition failure). The formed ignition kernel then propagates outward. The Minimum Ignition Energy (MIE), defined as the minimum energy required for successful ignition, is in this case 2.80 mJ.

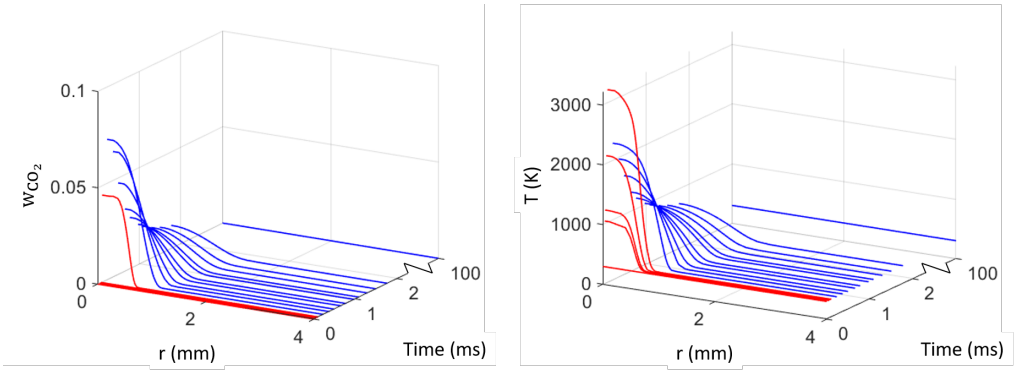

(a) CO_2 mass fraction profile (b) Temperature profile

Figure 4.2: The spatio-temporal profile of temperature and CO_2 mass fraction for the case of flame kernel formation with subsequent extinction for CH_4 / air mixture near the flammability limit. Red lines represent temperatures and CO_2 mass fractions within the spark duration, blue lines represent temperatures and CO_2 mass fractions after the spark duration, $\phi = 1.5$, $T_0 = 298$ K, $p = 1$ bar, with spherical geometry, $r_s = 0.5$ mm, $\tau_s = 0.1$ ms

In some cases, when the equivalence ratio of the CH_4/air mixture is near the lean/rich flammability limit and the ignition radius is small, flame extinction can be observed. This can be explained as follows: When the ignition radius is small, the flame curvature—being inversely proportional to the

flame radius—is large immediately after ignition, leading to rapid diffusion. However, since the chemical reactions for mixtures near the flammability limit are much slower than for stoichiometric mixtures [100], fast diffusion leads to a decrease in flame temperature, resulting in flame quenching after a while. An example is shown in Fig. 4.2, where the ignition radius of the spherical ignition kernel is $r_s = 0.5\,\mathrm{mm}$ and the equivalence ratio of the mixture is 1.5. In this case, CO_2 is massively produced after ignition ($w_{CO_2,\max}$ is about 4000 times larger than in the case of ignition failure), indicating a successful ignition and the formation of a flame kernel. However, fast diffusion causes a decrease in flame temperature. Eventually, the flame quenches, and the temperature at the center drops back to 298 K.

In the following sections, the dependence of MIE for methane/air mixture on different parameters is investigated.

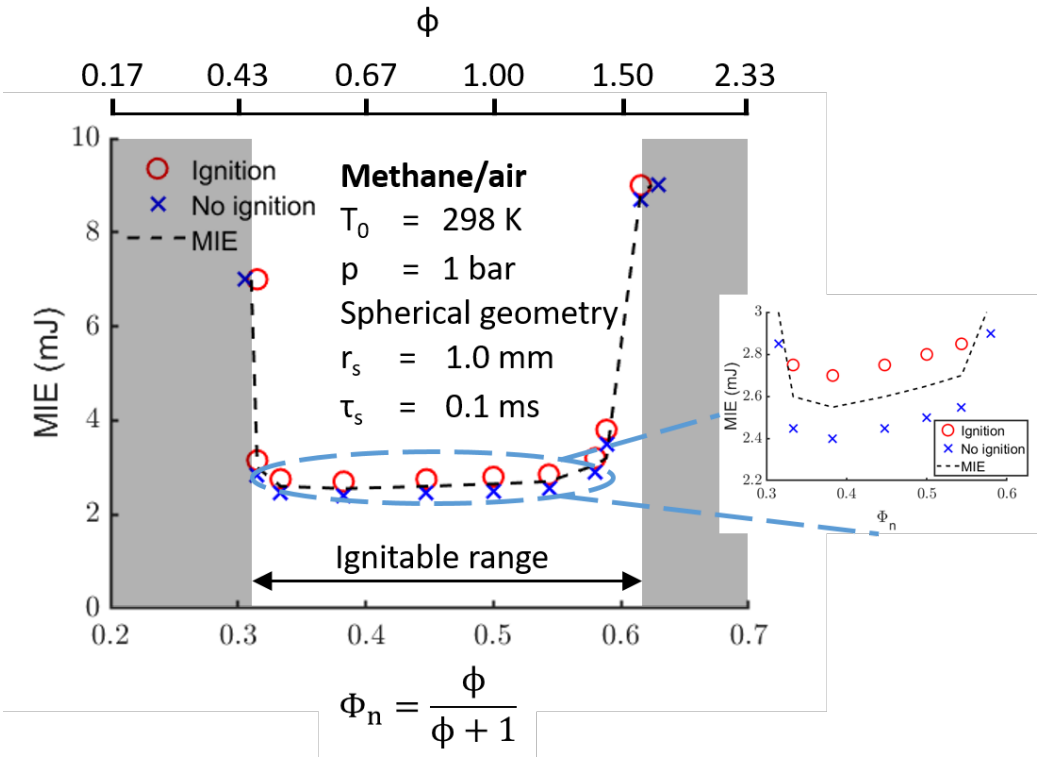

Figure 4.3: The dependence of MIE on equivalence ratio at 1 bar and $T_0 = 298\,\mathrm{K}$ for methane/air mixture with spherical geometry [129]

4.2 Dependence of MIE on Equivalence Ratio

After discussing the possible scenarios following ignition, the Minimum Ignition Energy (MIE) is defined as the minimum energy required for successful flame propagation. The next goal of this chapter is to analyze the key factors influencing MIE. With a relatively large ignition duration ($t_s = 100\,\mu$s), the influence of ignition duration on MIE is minimal. Since the mixture composition can affect the chemical reaction rate, this section first examines the dependence of MIE on the equivalence ratio, a key characteristic of the mixture composition.

The dependence of the MIE on equivalence ratio for a methane/air mixture with a spherical ignition kernel ($r_s = 1.0\,$mm) under atmospheric conditions is shown Fig. 4.3.

Here, to present the both the rich side ($\phi > 1$) and the lean side ($\phi < 1$) of the ignitable range in a nealy symmetrical manner, a normalized equivalence ratio is introduced [71]:

$$\Phi_n = \frac{\phi}{\phi + 1} \tag{4.1}$$

The MIE of methane under atmospheric conditions is only weakly dependent on the equivalence ratio within the ignitable range, with the MIE on the lean side slightly lower than on the rich side. The minimum value of MIE = 2.70 mJ is reached at $\phi = 0.6$, which is about 5% smaller than the MIE for the stoichiometric mixture (MIE = 2.80 mJ). This is mainly because the specific heat capacity (c_p) of the lean CH_4/air mixture is smaller than that of the rich CH_4/air mixture. With the same ignition energy, the lean CH_4/air mixture can be heated to a higher temperature than the rich CH_4/air mixture, as shown in Fig. 4.4.

However, as ϕ approaches the flammability limit, MIE increases rapidly. This is mainly due to the slower chemistry of mixtures near the flammability limit compared to stoichiometric mixtures [100]. Fig. 4.5 shows the temperature and HRR profiles of stoichiometric ($\phi = 1$) and near-limit rich mixture ($\phi = 1.4$) of CH_4/air under atmospheric conditions. The flame front is defined as the position of the HRR peak. A flame-centered coordinate system, denoted by $r - r_f$, is employed, with the origin of the x-axis defined as the position of the flame front. As can be observed in Fig. 4.5, the peak HRR for the near-limit rich mixture is almost 10 times smaller than that for the stoichiometric mixture. This reduction in HRR is primarily due to the lack of oxidizing agents in the near-limit rich mixture, which decreases the efficiency of the chemical reactions. Additionally, the excess fuel molecules can act as third-body collision partners, accelerating third-body chain termination

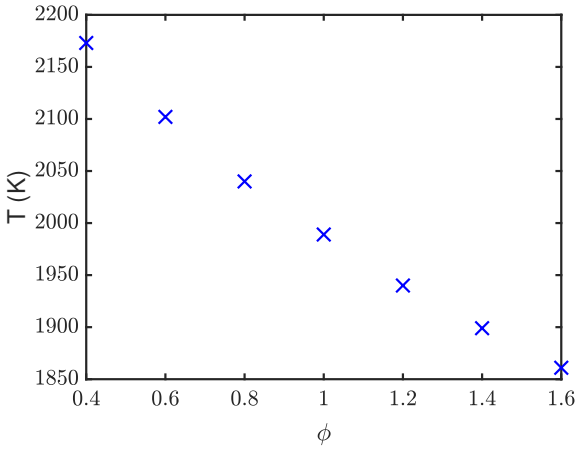

Figure 4.4: Temperature at the center of the ignition volume at the end of ignition duration in dependence of equivalence ratio for methane/air mixture under atmospheric conditions

reactions and further inhibiting heat release. Furthermore, the high overall activation energy E_a for the near-limit rich mixture lowers the rate coefficient k as described by the Arrhenius law [110]:

$$k = A \cdot exp(-\frac{E_a}{RT}) \tag{4.2}$$

On the other hand, the larger flame thickness of the near-limit mixture compared to the stoichiometric mixture shows the importance of diffusion for the rich mixture. Higher ignition energy is needed for the near-limit mixture (compared to the stoichiometric mixture) to compensate for the heat loss through diffusion.

The flammability limits of methane under atmospheric conditions, estimated using spherical geometry with $r_s = 1.0\,\text{mm}$, are LFL = 0.46 and UFL = 1.60. The measured flammability limits in experiments are typically reported in mole fractions of methane, ranging from 3.8% to 5.0% for the lean side and from 15.8% to 16.9% for the rich side, depending on the experimental methods used [21, 102, 117]. This corresponds to flammability ranges in equivalence ratios from $\phi = 0.376$ to $\phi = 0.501$ on the lean side and from $\phi = 1.787$ to $\phi = 1.937$ on the rich side. On the rich side, the RFL predicted using spherical geometry is closer to stoichiometry than the RFL measured in experiments. This is mainly because the flame geometry in experiments lies between a cylinder and a sphere. Simulations conducted with spherical geometry overpredicted the curvature effect on the rich side. On the lean side,

since the Lewis number of lean methane/air mixtures is slightly below unity, the flame is less sensitive to curvature effects, compared to the rich mixtures, whose Lewis number is slightly greater than 1. As a result, the LFL predicted using spherical geometry shows good agreement with experimental data.

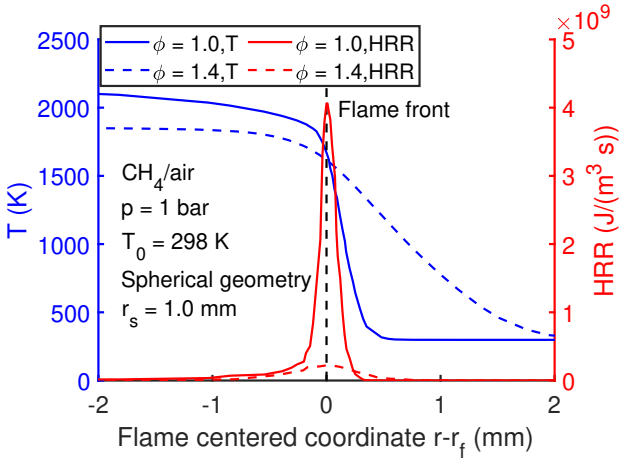

Figure 4.5: Temperature and heat release rate profiles of stoichiometric ($\phi = 1$, solid line —) and rich mixture ($\phi = 1.4$, dotted line – –) of CH_4/air

In summary, the dependence of MIE on the equivalence ratio exhibits a U-shape. This trend is primarily due to the slow chemical reactions occurring in near-limit mixtures and is consistent with other MIE investigations [74, 80]. Furthermore, the estimation of flammability limits for methane/air mixtures using induced ignition simulations in spherical geometry shows good agreement with experimental data.

4.3 Dependence of MIE on Ignition Geometry

In addition to mixture composition, ignition parameters such as ignition geometry also have a significant impact on MIE. In our in-house code INSFLA [80], one-dimensional simulations can be performed using spherical, cylindrical, and planar geometries. When numerically investigating the induced ignition process with different geometries, it is important to note that, as is explained in Sec. 3.1.1, the calculated MIE for one-dimensional induced ignition with different geometry has different units: J for sphere, J/m for infinite cylinder, and J/m^2 for infinite slab. For comparison of MIE with different geometries, the ignition energy density q_s, as defined in Sec. 3.1.1, is employed. Another advantage of using the minimum ignition energy density

instead of MIE is to allow comparison between different ignition radii. Since ignition energy depends not only on the physical and chemical behavior of the fuel/air mixture but also on the ignition volume, which is directly related to ignition radius, using q_s eliminates the influence of ignition volume. This allows one to concentrate on the chemical and physical effects during ignition.

The dependence of $q_{s,min}$ on ϕ is shown for spherical, cylindrical, and planar geometries with two different ignition radius $r_s = 1.0\,\text{mm}$ and $r_s = 0.5\,\text{mm}$ in Fig. 4.6 and Fig. 4.7.

It is first observed that within the ignitable range, $q_{s,min}$ shows only a weak dependence on ϕ, the geometry and ignition radius. Within the ignitable range, $q_{s,min}$ for a small ignition radius is slightly higher than that for a large ignition radius because the large temperature gradient at a small ignition radius causes greater heat loss from the ignition kernel to the fresh mixture, compared to at a large ignition radius.

Approaching the ignitable range, $q_{s,min}$ for small ignition radius ($r_s = 0.5\,\text{mm}$) exhibits a more rapid increase than for large ignition radius ($r_s = 1.0\,\text{mm}$), especially for spherical geometry. The main reason of this is that, for curved geometries with small ignition radius, the flame curvature at early phase of flame propagation is large, diffusion becomes important [80]. For mixtures near the flammability limit, chemical reactions become slow and are very sensitive to disturbances. The competition between heat release through chemical reactions and heat conduction out of the reaction zone may cause flame extinction. For flame kernel with large curvature, higher ignition energies are needed compared to small curvature or no curvature (planar geometry) for the flame to live through the critical phase.

Comparing the flammable range calculated with different geometries, it can be observed that the geometry used in simulations also affects the lean and rich flammability limits. Here, by using the ignition energy density instead of the ignition energy, the influence of ignition volume is eliminated. Table 4.1 displays the flammability limits estimated in simulations with various geometries and those measured in experiments.

For the lean side, where the Lewis number of the mixture is slightly below 1, the mixture is not very sensitive to curvature. Both curved geometries provide reasonable predictions of the LFL, with the LFL predicted by the planar geometry being slightly too lean.

However, on the rich side, where the mixture has a Lewis number greater than 1, it is more sensitive to curvature effects. The RFL measured in experiments lies between those estimated with spherical and cylindrical geometries, suggesting that the flame geometry in experiments lies between these two curved geometries. The RFL estimated with planar geometry significantly

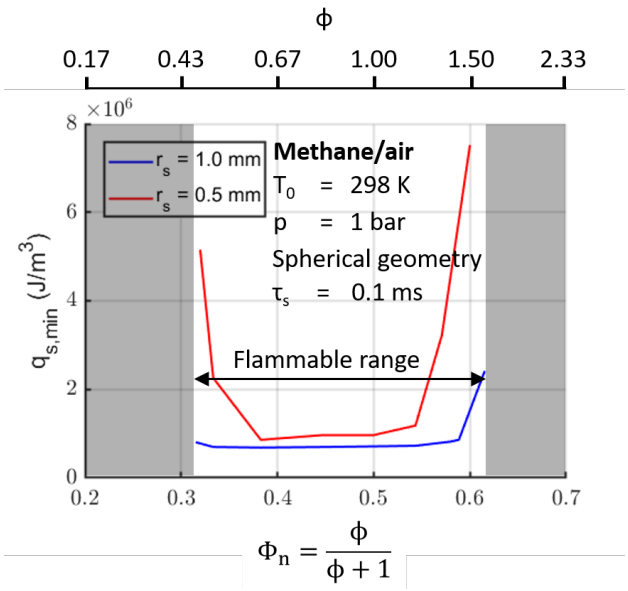

(a) Spherical geometry

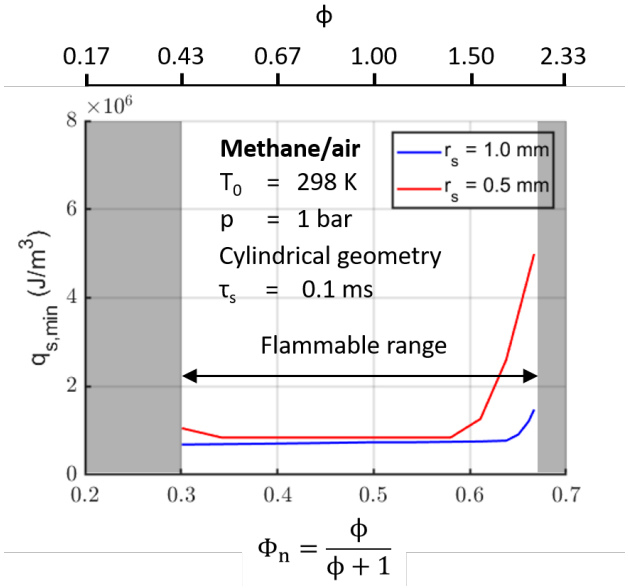

(b) Cylindrical geometry

Figure 4.6: The dependence of minimum ignition energy density on equivalence ratio at 1 bar and $T_0 = 298\,\mathrm{K}$ for methane/air mixture with curved geometries [129]

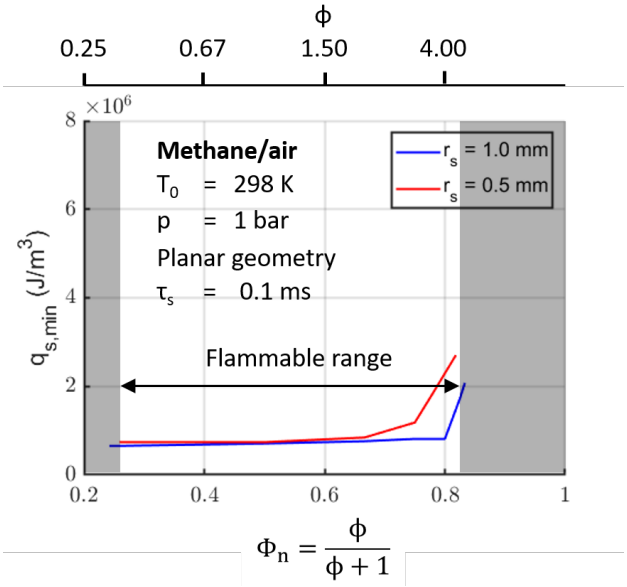

Figure 4.7: The dependence of minimum ignition energy density on equivalence ratio at 1 bar and $T_0 = 298\,\mathrm{K}$ for methane/air mixture with planar geometry

Table 4.1: Flammability limits estimated in simulations and measured in experiments

	Geometry/Ref.	LFL	RFL
Simulation	Spherical	0.46	1.6
	Cylindrical	0.43	2
	Planar	0.32	5
Experiment	[21, 102, 117]	0.38-0.50	1.79-1.94

exceeds the experimental measurements, underscoring the importance of considering curvature effects in simulations.

In this chapter, the induced ignition process of methane was examined. As a key component of natural gas, understanding methane's behavior is crucial for the development of efficient and safe combustion systems using natural gas. Additionally, as the smallest hydrocarbon fuel, methane serves as an ideal starting point for studying the induced ignition of all hydrocarbon fuels. The results confirm the U-shaped dependency of MIE on the equivalence ratio and highlight the significant influence of geometry on the induced ignition process.

5 Induced ignition of PRF

Primary reference fuels (PRF, binary mixture of iso-octane, C_8H_{18} and n-heptane, C_7H_{16}) are important gasoline surrogate fuels. Therefore, investigating the ignition and early flame propagation process is important for practical applications.

The Research Octane Number (RON) is a critical characteristic of a fuel, representing the knocking tendency equivalent to a Primary Reference Fuel (PRF) with the corresponding percentage of iso-octane by volume in a blend [7, 42]. The importance of RON is related to the knock phenomena in gasoline engines, where a high compression ratio can cause undesirable ignition in the end gas [67]. Due to differences in molecular structure and chemical kinetics, n-heptane has a much higher knock tendency than iso-octane [79, 123]. Consequently, RON is often used to define the knocking tendency of gasoline fuels. For example, a fuel with RON = 50 has the same knocking tendency as a PRF mixture containing 50% iso-octane and 50% n-heptane. In this work, PRFs are investigated: Pure iso-octane corresponds to RON = 100, while pure n-heptane corresponds to RON = 0. Any RON value between 0 and 100 represents mixtures of iso-octane and n-heptane.

The numerical investigation of ignition processes of PRFs is more complicated than that of small hydrocarbon fuels like methane, for two main reasons:

- The chemical kinetics of PRFs are more complex compared to methane. This complexity arises in the high-temperature branch from the hierarchical structure of hydrocarbon oxidations, where the oxidation mechanisms of PRFs include both the oxidation mechanisms of methane and the reactions for the decomposition of higher hydrocarbons [123]. Additionally, the low-temperature chemistry of large hydrocarbons contributes to an even larger chemical mechanism [123].

- The diffusion process of PRF/air mixtures are more complex compared to methane/air mixtures. This complexity arises from the larger molecules of iso-octane or n-heptane, compared to methane. While the Lewis number of methane/air mixtures is close to one for both lean and

rich mixtures, the Lewis number of PRF/air mixture is smaller than one for rich mixtures and greater than one for lean mixtures (for example, $Le \approx 3$ for PRF/air mixtures at $\phi = 0.8$ [112]). This means that for the ignition and early flame propagation process of lean PRF/air mixtures, which is attractive for its low emission and high performance, flame extinction can happen because of the stretch effect [71].

In the past, several chemical mechanisms for PRFs have been developed. One of the most well-known detailed mechanisms is published by Lawrence Livermore National Laboratory (LLNL), known as the LLNL mechanisms [31]. The LLNL mechanism for PRFs is an assembly of the detailed LLNL mechanisms for iso-octane [29] and n-heptane [30]. Due to the inclusion of several hundred species and several thousand elementary reactions, calculations using LLNL detailed mechanisms can take up to several days. To reduce computation time, semi-detailed mechanisms have been developed. In this work, a mechanism based on a semi-detailed chemical kinetics model for toluene reference fuels (TRF) was used, which includes 137 species and 633 reactions [5], and also includes the PRF mechanism. This mechanism has been validated with homogeneous charge compression ignition experiments and is widely used for simulations of gasoline surrogate fuels (e.g., see [64]).

Even though the mechanisms were validated with properties like IDT, the impact of the choice of mechanism on the simulations of induced ignition processes remains an open question. To this end, in this work, the MIE was first calculated using the mechanism from Andrae et al., the LLNL mechanism, and another mechanism by Wang et al.[122] for a lean n-heptane/air mixture with $\phi = 0.8$, $T_0 = 373$ K, and $p_0 = 1$ bar, with a spherical ignition source of radius $r_s = 1.5$ mm and duration $\tau_s = 0.1$ ms. As shown in Table 5.1, the MIE calculated using the three different mechanisms only differs by about 0.5%. Additionally, with the same ignition energy, the maximum temperature at the end of the ignition duration is also similar. One possible explanation is as follows: Since the thermodynamic properties of species in different mechanisms are comparable, the result that the temperature at the end of the calculation is comparable is not surprising. After the ignition energy was shut off, auto-ignition (or ignition failure) occurs in the ignition volume [123]. Given that the IDT calculated by different mechanisms is comparable, it is also not surprising that the MIE calculated with different mechanisms is comparable. This indicates that the choice of mechanism has only a minor influence on the calculated MIE, making the use of the mechanism from Andrae et al. a reasonable choice over the LLNL mechanism.

Table 5.1: MIE and the maximum temperature at the end of the ignition duration with $E_{ig} = 7.2$ mJ for three different mechanisms

Mechanism	LLNL [31]	Andrae et al. [5]	Wang et al. [122]
MIE [mJ]	7.00	6.80	7.15
T_{max} [K]	1364	1369	1377

In the past few decades, the auto-ignition properties (see, e.g., [2, 13, 33]) and steady-state flame propagation properties (see, e.g., [54, 76]) of PRF/air mixtures and their RON dependence have been thoroughly investigated. However, fewer studies focus on the transition from an ignition kernel to a self-sustained flame for PRFs. Does the MIE of PRF/air mixtures also depend on RON? How does the interaction between chemical reactions and diffusion affect the induced-ignition process of PRF/air mixtures? Does pressure play a role in the induced-ignition process of PRF/air mixtures? Is it possible to model the stochastic nature of the induced-ignition process with one-dimensional simulations? These questions, despite their importance for practical implementations and safety issues, remain open.

To gain a deeper understanding of the ignition and early flame propagation processes of PRF/air mixtures, this work conducts a numerical investigation. The focus is on the dependence of the minimum ignition energy (MIE) on various parameters, such as the equivalence ratio, RON, ignition radius, strain rate, and stochastic behavior. These parameters are crucial for characterizing the ignition conditions and initial flame development.

In this chapter, the results of these numerical investigations are presented. The obtained numerical results are validated using experimental data from the literature. This comprehensive analysis aims to contribute to a better understanding of the ignition mechanisms and early flame propagation in PRF/air mixtures.

5.1 Flame Scenarios

For PRF, a greater variety of outcomes after ignition were observed compared to methane. As mentioned before, flame extinction can be observed in the ignition and early flame propagation process of PRFs. Additionally, particularly at elevated pressure, cool flame and two-stage ignition phenomena can be observed. The spatio-temporal temperature and CO_2 profiles are used in this section to describe the ignition and early flame propagation process, or the extinction, in different scenarios.

In total, five qualitatively different flame scenarios can be observed after ignition:

Type I	Ignition failure
Type II	Successful hot flame ignition and subsequent flame extinction
Type III	Successful hot flame ignition and self-sustained flame propagation
Type IV	Successful cool flame ignition and consequent flame extinction
Type V	Two stage ignition

For the ignition of PRF at atmospharic pressure, the low temperature chemistry is too weak to trigger a cool flame, only type I-III can be observed.

For the ignition of PRF at elevated pressure, the low temperature chemistry plays a more important role [5], compared to the ignition of PRF at 1 bar. A cool flame might be observed after ignition energy deposition, which may evolve into a self-sustained hot flame, or quench because of its low heat release rate. All five types can be observed.

Scenario I: Ignition Failure

Typical temperature and CO_2 profiles of scenario I, ignition failure, are shown in Fig. 5.1. Here, the ignition energy is $E = 6.70\,\mathrm{mJ}$. During the deposition of ignition energy, the temperature in the ignition volume increases. At the end of the ignition duration, the temperature in the ignition volume is about 1300 K. However, 1300 K still doesn't reach the minimum ignition temperature for iso-octane at 1 bar and 373 K; therefore, fast chemical reactions are not triggered. The evidence of the ignition failure is the absence of CO_2 formation; the peak of the CO_2 profile is about 3000 times smaller than the other cases below. The temperature in the ignition volume decreases after the ignition duration and drops back to 373 K at the end of the calculation.

Scenario II: Ignition and Subsequent Flame Extinction

The temperature and CO_2 profiles of scenario II, successful ignition and consequent flame extinction, are shown in Fig. 5.2. Here, the ignition energy is $E = 6.80\,\mathrm{mJ}$, which is $0.10\,\mathrm{mJ}$ higher than the ignition energy in scenario I. This results in a temperature at the center at the end of the ignition energy deposition about 40 K higher than in scenario I. This temperature is above the minimum ignition temperature. Flame initiation, which results in a

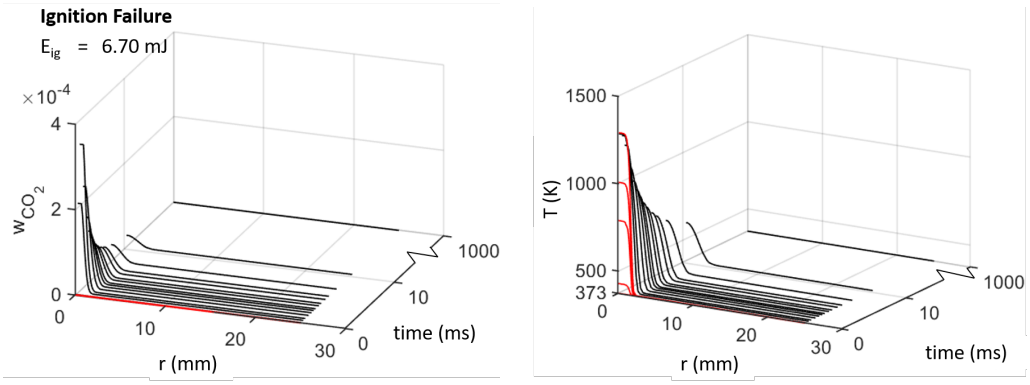

(a) CO_2 mass fraction profile **(b)** Temperature profile

Figure 5.1: The spatio-temporal profile of temperature and CO_2 mass fraction for the case with ignition failure for iso-octane/air mixture with $\phi = 0.8$ at 1 bar and 373 K in simulations, using spherical geometry with $r_s = 1.5$ mm and $\tau_s = 100\,\mu$s. Red lines represent temperatures and CO_2 mass fractions within the spark duration, black lines represent temperatures and CO_2 mass fractions after the spark duration

temperature increase of about 1000 K is observed. Additionally, a remarkable production of CO_2 (3000 times more than scenario I) is observed. However, in the early phase, the flame curvature with spherical geometry is very high, leading to large heat conduction to the unburnt mixture, causing the flame temperature to decrease. At a certain flame radius, the flame quenches, and the formed CO_2 diffuses away. At the end of the calculation, the temperature decreases back to 373 K, similar to scenario I. In this case, $\mathrm{MIE_{ini}} = 6.80\,\mathrm{mJ}$.

Scenario III: Flame Propagation

If the ignition energy keeps increasing (from $\mathrm{MIE_{ini}}$), the temperature at the center at the end of the ignition duration also keeps increasing. However, the temperature still decreases rapidly with flame extinction at the end. Until the ignition energy increases to $E = 16.30\,\mathrm{mJ}$, a self-sustained flame (scenario III) can be observed. The temperature and CO_2 profiles of scenario III are shown in Fig. 5.3. Here, the temperature at the center at the end of ignition duration is far greater than in the first two cases, reaching about 5000 K. Because the temperature in the ignition volume is brought to a very high value, flame initiation with massive formation of CO_2 is already observed during the energy deposition. After ignition duration, although the flame

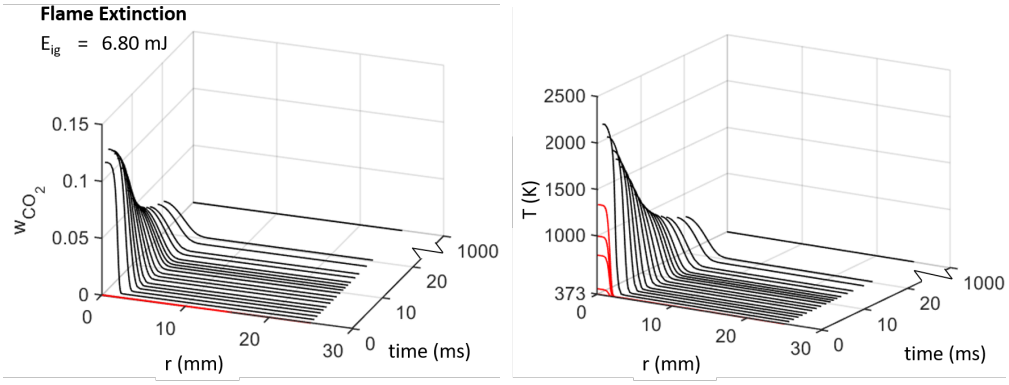

(a) CO_2 mass fraction profile **(b)** Temperature profile

Figure 5.2: The spatio-temporal profile of temperature and CO_2 mass fraction for the case with ignition failure for iso-octane/air mixture with $\phi = 0.8$ at 1 bar and 373 K in simulations, using spherical geometry with $r_s = 1.5$ mm and $\tau_s = 100\,\mu$s. Red lines represent temperatures and CO_2 mass fractions within the spark duration, black lines represent temperatures and CO_2 mass fractions after the spark duration

temperature also decreases due to curvature effect, the excess enthalpy form ignition source helps the flame survive through the critical phase and becomes self-sustained. In this case (iso-octane/air mixture at $p = 1$ bar and $T_0 = 373$ K, $\phi = 0.8$, using spherical geometry with $r_s = 1.5$ mm and $\tau_s = 100\,\mu$s), $\mathrm{MIE}_{\mathrm{prop}} = 16.30\,\mathrm{mJ}$.

One interesting observation of scenario III is that there seems to exist both a slow flame regime and a fast flame regime. As shown in Fig. 5.3, the flame initially propagates with a slow velocity, accompanied by a decrease in flame temperature. As the flame moves away from the center and the flame radius increases, the curvature of the flame front decreases. Once the flame reaches a critical radius, the flame temperature increases again, and a fast flame propagation can be observed.

To further prove the existence of fast and slow flame during the ignition of PRF flame, to explain the phenomenon, and to find out if it's responsible for the flame extinction, the flame movement caused by chemical reactions is examined. Here, as explained in Sec. 3.1, the Lagrangian coordinate ψ is used to eliminate the influence of thermal expansion and allow concentration on flame propagation. The cubic root of ψ_{r_f}, representing the Lagrangian coordinate at the flame front, is employed as a spatial indicator of flame propagation.

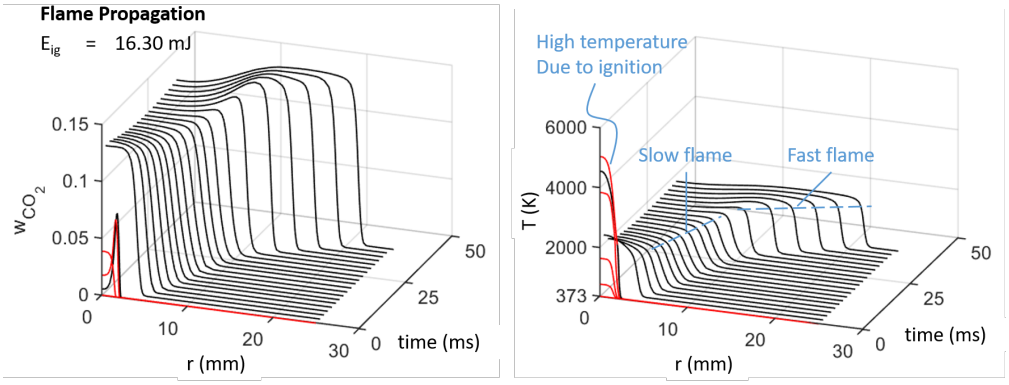

(a) CO_2 mass fraction profile **(b)** Temperature profile

Figure 5.3: The spatio-temporal profile of temperature and CO_2 mass fraction for the case with flame propagation for iso-octane/air mixture at 1 bar and 373 K in simulations. Red lines represent temperatures and CO_2 mass fractions within the spark duration, black lines represent temperatures and CO_2 mass fractions after the spark duration

As shown in Fig. 5.4, two parts of a nearly linear relationship with different slopes are observed for both iso-octane and n-heptane flames. The slopes here represent the flame propagation speed. This indicates the existence of a slow flame during the critical phase and a fast flame afterward. If the ignition energy is smaller than MIE_{prop}, the flame quenches, while if the ignition energy is greater than MIE_{prop}, the flame can overcome the stretch effect, reach the critical radius, and become a self-sustained flame.

Additionally, the difference between the n-heptane flame and the iso-octane flame can be observed. For the n-heptane flame, the fast flame propagates about 3 times faster than the slow flame, while for iso-octane, the fast flame is almost 6 times faster than the slow flame. The propagation speed of the fast flame for both fuels is similar, but the propagation speed of the n-heptane slow flame is faster than that of iso-octane. This implies different regimes of interaction between chemical reaction and transport processes between the two fuels, especially during the critical phase. This difference is further explained in the next section, where the dependence of MIE on RON is investigated.

Having confirmed the presence of both fast and slow flame phenomena, the next question relates to the underlying mechanisms behind this observation. For this purpose, temperature profiles and profiles of mass fractions of important species (OH, H_2O_2, and HO_2) are shown for both slow and fast flames

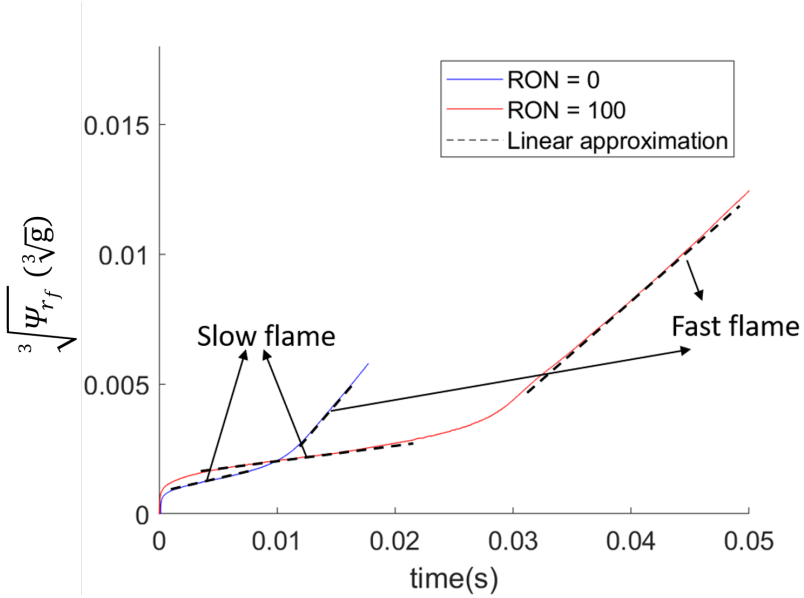

Figure 5.4: The flame front movement caused by chemical reactions for an iso-octane (RON=100) and for a n-heptane (RON = 0) flame, both at $\phi = 0.8$, $p = 1$ bar, $T_0 = 373$ K, using spherical geometry with $r_s = 1.5$ mm [128]

for iso-octane. In the case of the fast flame, the flame front is already far away from the center. For this reason, a flame-centered coordinate $r - r_f$ (r_f is the position of the flame front defined by the peak of HRR) in the vicinity of the flame front is used.

The difference between slow and fast flames can be clearly seen in Fig. 5.5. While for fast flames, the peak of OH mass fraction is significantly larger than for slow flames (about 2.5 times), the peaks of H_2O_2 and HO_2 mass fractions for both fast and slow flames are similar. This indicates that the slow and fast flames are governed by different mechanisms, as also mentioned in [79]. For the fast flames, OH is the governing intermediate species. For the slow flames, the production of OH via reactions related to HO_2 and H_2O_2 plays a more important role. These different mechanisms and flame structures are also observed in n-heptane flames and n-heptane/iso-octane blend flames.

As previously mentioned, at atmospheric pressure, the low-temperature chemistry of PRF is too weak, so only flame scenarios I-III can be observed. The determination of different scenarios following ignition energy deposition for PRF/air mixtures at atmospheric pressure is shown in Fig. 5.6. If the ignition energy is smaller than $\mathrm{MIE_{ini}}$, ignition is not successful. Once the ignition energy reaches $\mathrm{MIE_{ini}}$, a flame kernel is formed. However, the

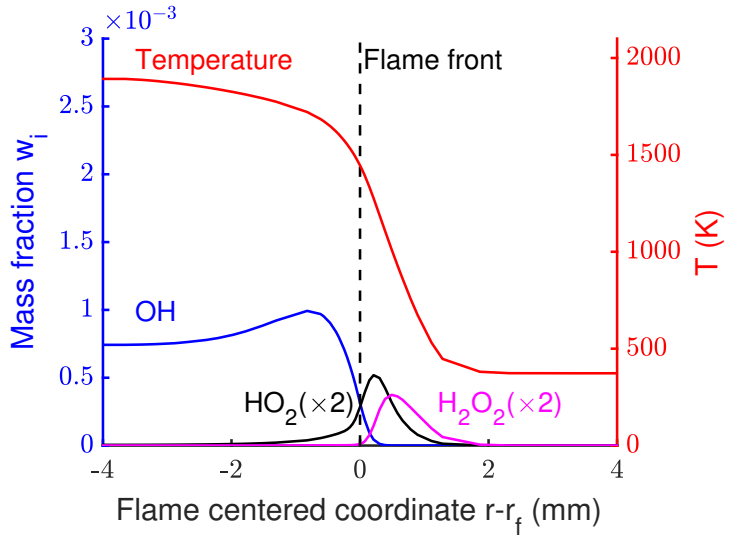

(a) Slow Flame

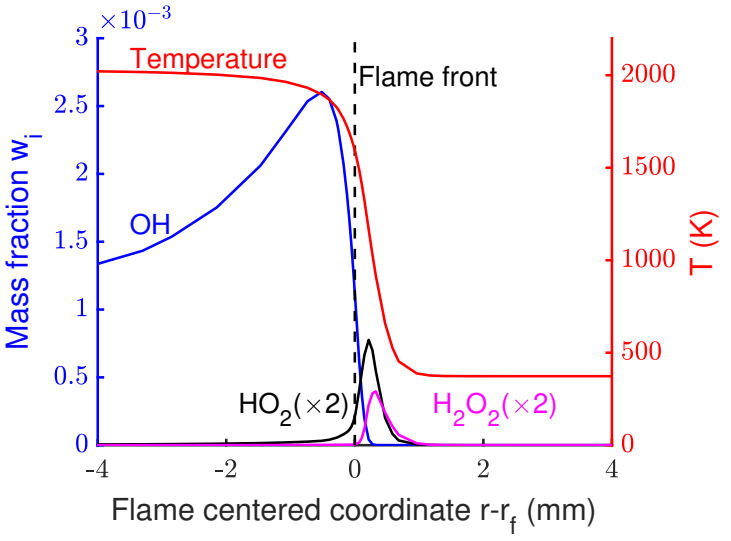

(b) Fast Flame

Figure 5.5: The temperature profile and mass fraction profiles of OH, H_2O_2, and HO_2 for the fast and slow flame of iso-octane at $\phi = 0.8$, $p = 1$ bar, $T_0 = 373$ K, using spherical geometry with $r_s = 1.5$ mm [128]

formation of a flame kernel doesn't guarantee self-sustained flame propagation; this only occurs if the ignition energy reaches MIE_{prop}. Otherwise, flame extinction can be observed.

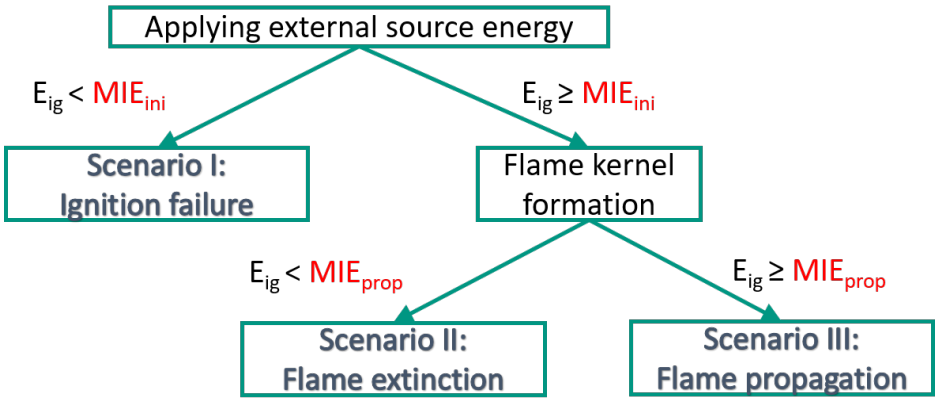

Figure 5.6: Determination of different scenarios following ignition energy deposition for PRF at atmospharic pressure

Scenario IV: Successful Cool Flame Ignition and Subsequent Flame Extinction

At elevated pressure, the low-temperature chemistry of PRF can initiate a cool flame. This cool flame may either quench due to the low heat release rate (Scenario IV) or evolve into a hot flame (Scenario V).

The temperature and CO_2 profiles of scenario IV, cool flame initiation, and consequent flame extinction, are shown in Fig. 5.7. With the help of the low-temperature chemistry of n-heptane, although the fresh mixture is only heated up to about 700 K, which is 600 K lower than the minimum ignition temperature at atmospheric pressure, a rise in temperature of about 100 K can be observed. This indicates the formation of a flame kernel inside which the reaction commences. The chemical reaction here is only weakly exothermal. The formed CO_2 is about 10 times larger than in the case of ignition failure but 50 times smaller than in the case of hot flame initiation, because the mixture gets only partially oxidized. This corresponds to the cool flame phenomenon [62]. Because of the low heat release rate of the cool flame and the strong diffusion caused by curvature, the flame finally quenches, with the temperature dropping back to 373 K (ambient temperature).

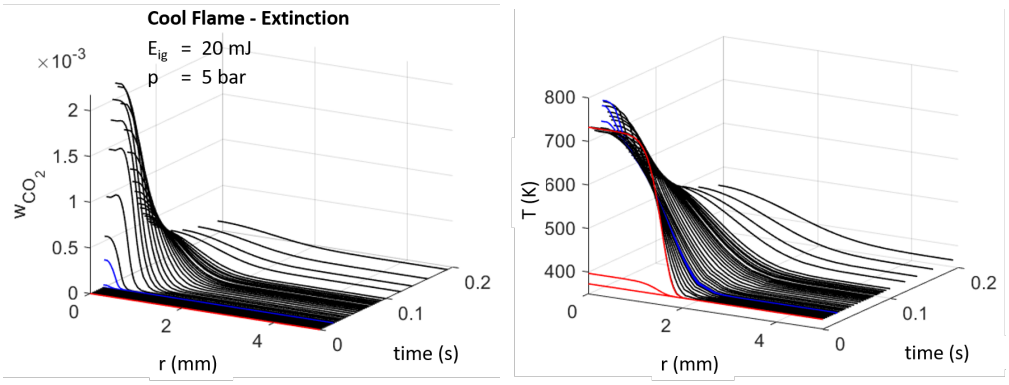

(a) CO_2 mass fraction profile **(b)** Temperature profile

Figure 5.7: The spatio-temporal profile of temperature and CO_2 mass fraction for the case with cool flame and flame extinction for n-heptane/air mixture at 5 bar and 373 K in simulations. Red lines represent temperatures and CO_2 mass fractions within the spark duration

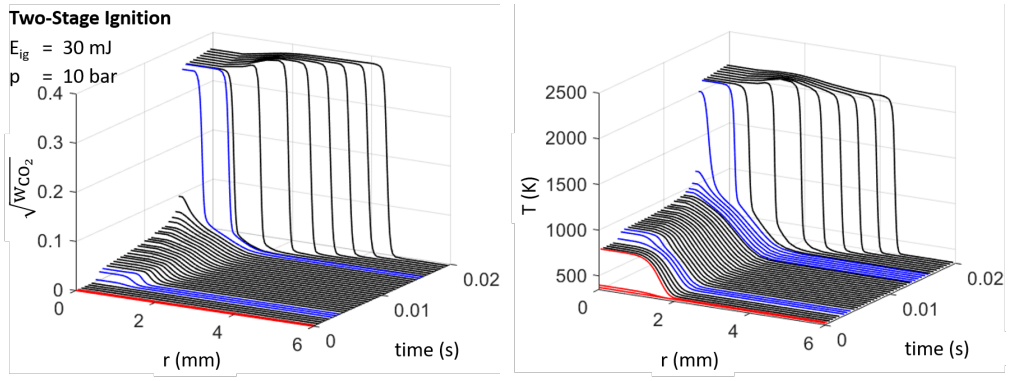

(a) CO_2 mass fraction profile **(b)** Temperature profile

Figure 5.8: The spatio-temporal profile of temperature and CO_2 mass fraction for the case with cool flame and flame extinction for n-heptane/air mixture at 10 bar and 373 K in simulations. Red lines represent temperatures and CO_2 mass fractions within the spark duration

Scenario V: Two Stage Ignition

The temperature and CO_2 profiles of scenario V, two-stage ignition, are shown in Fig. 5.8. Similar to flame scenario IV, a cool flame with about a 100 K temperature rise and partial oxidization of the mixture (indicated by the small amount of CO_2 formation) can be observed. However, instead of the extinction of the cool flame, another fast temperature rise of about 1500 K is observed. After the two-stage ignition, the cool flame becomes a self-sustained hot flame. The mixture in the hot flame is completely burnt, indicated by a much larger amount of CO_2 formation, compared to the cool flame.

The flame structure of the hot and cool flame of n-heptane is shown in Fig. 5.9. The difference is clearly observed: Although the peak of the OH mass fraction of the cool flame is about 1000 times smaller than the hot flame, the peak of the HO_2 and $C_7H_{15}O_2$ mass fraction of the cool flame is 3 times larger than the hot flame, and the peak of the H_2O_2 mass fraction of the cool flame is 10 times larger than the hot flame. This indicates the importance of the reactions with HO_2, H_2O_2, and $C_7H_{15}O_2$ radicals and confirms that the cool flame is dominated by the low-temperature chemistry of n-heptane.

5.2 Dependence of MIE on Equivalence Ratio

Having explored the various flame scenarios following ignition for primary reference fuels and defined the MIE, the next focus is to understand the influencing factors of MIE for PRFs. In investigations of other fuels (e.g., methane in this work, described in Chapter 4; and the work of Lewis and von Elbe [74]), equivalence ratio (ϕ) has been shown to affect MIE. New questions arise: How does the MIE of PRFs depend on ϕ? Is it quantitatively comparable to the MIE of methane? To answer these questions, the dependence of MIE on ϕ for iso-octane/air mixtures is explored in this section. Simulations are conducted at 1 bar and $T_0 = 298\,\mathrm{K}$, typical ambient temperature and pressure often used in experiments and simulations.

The dependence of MIE on equivalence ratio at 1 bar and $T_0 = 298\,\mathrm{K}$ for iso-octane/air mixture with spherical geometry ($\tau_s = 100\,\mu\mathrm{s}$, $r_s = 1.0\,\mathrm{mm}$) is shown in Fig. 4.3. Here, the MIE corresponds to $\mathrm{MIE}_{\mathrm{prop}}$, with the blue X corresponding to ignition failure/flame extinction, and the red O corresponding to flame propagation.

Compared to the dependence of MIE on ϕ for methane/air mixture under the same conditions (Fig. 4.3), similarities can be observed: Firstly, the dependence of MIE on ϕ for iso-octane/air mixtures also follows a U-shape.

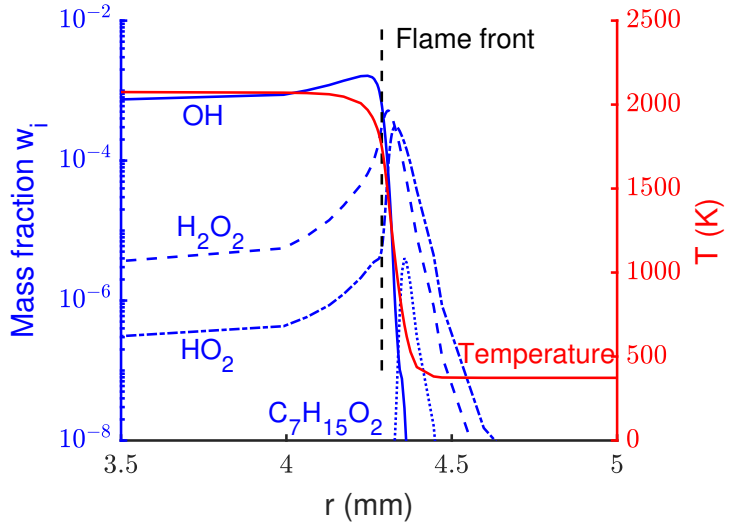

(a) Cool Flame

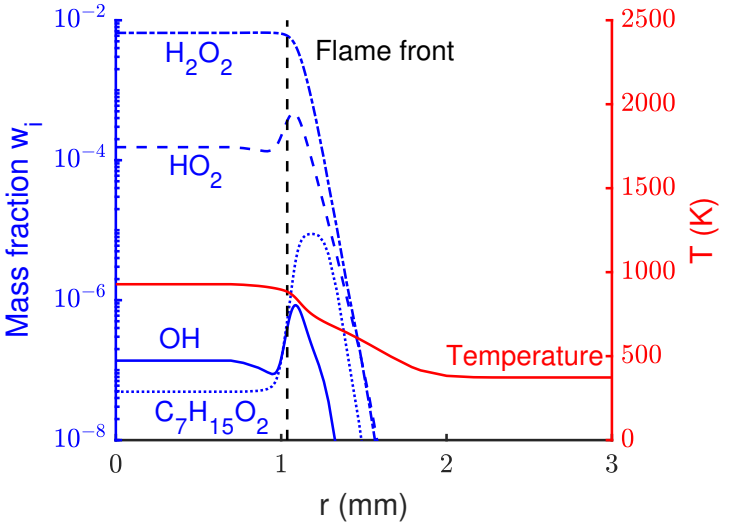

(b) Hot Flame

Figure 5.9: The temperature profile and mass fraction profiles of OH, H_2O_2, HO_2, and $C_7H_{15}O_2$ for the cool and hot flame of n-heptane at $\phi = 0.8$, $p = 10$ bar, $T_0 = 373$ K, using spherical geometry with $r_s = 1.5$ mm

Secondly, the MIE within the flammability limits for both mixtures are comparable. This agrees with the results from experiments (see, e.g., [88]). A possible explanation for the similarity of MIE for different hydrocarbons within the flammability limits is that, at 1 bar, the low temperature chemistry is weak. Iso-octane/air mixtures have to be heated up to 1200 K for successful ignition. At high temperature ranges, the decomposition of higher hydrocarbons to CH_3 and C_2H_5 radicals is fast compared to the rate-limiting reactions of CH_3 and C_2H_5 [123]. These reactions for both methane/air mixtures and iso-octane/air mixtures are the same.

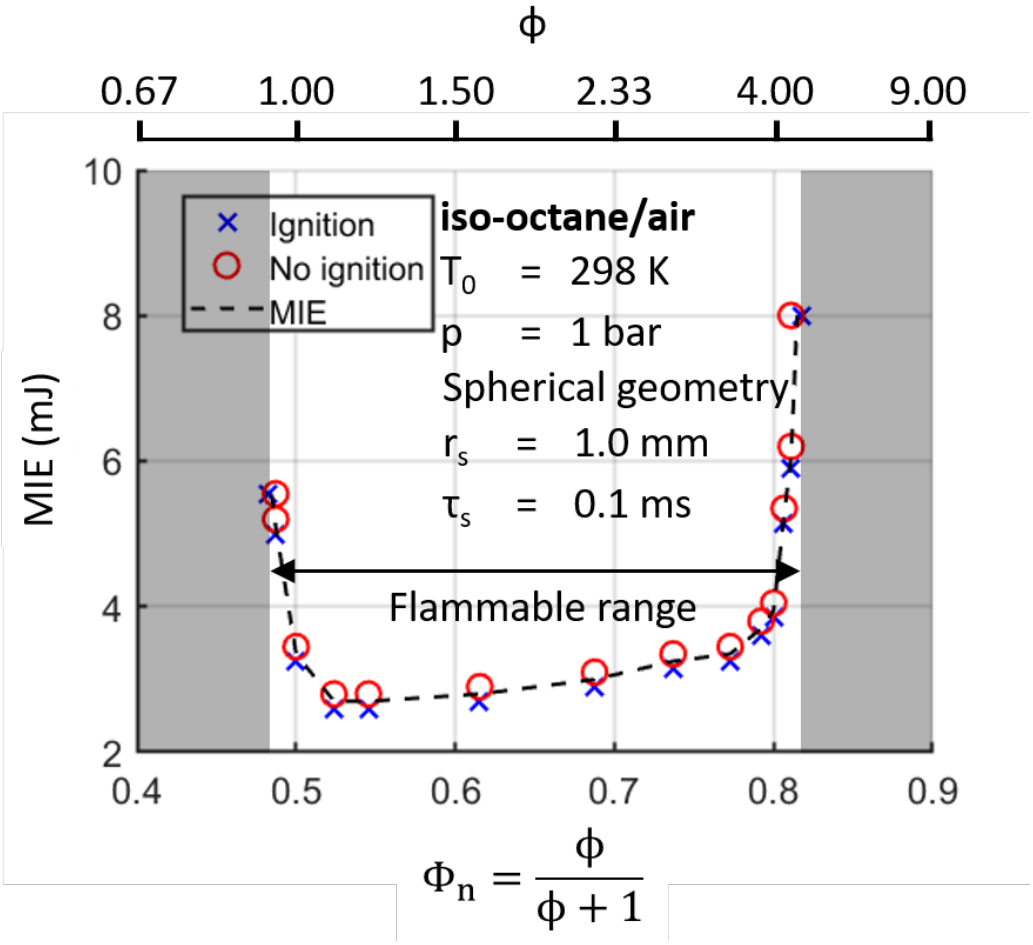

Figure 5.10: The dependence of MIE on equivalence ratio at 1 bar and $T_0 = 298\,\mathrm{K}$ for iso-octane/air mixture with spherical geometry [129]

Within the flammable range, the MIE increases with increasing ϕ. Similar to methane, this phenomenon is caused by the different specific heat capacity

for mixtures at different ϕ. As is shown in Fig. 5.11, with a same ignition energy $E = 2.80\,\mathrm{mJ}$, the temperature at the center of the ignition volume at the end of ignition duration decreases with increasing equivalence ratio. The stoichiometric mixture can be heated up to about 500 K higher than a mixture with $\phi = 4$.

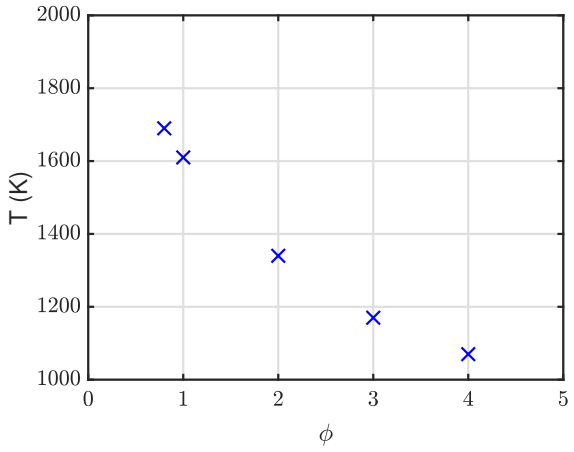

Figure 5.11: Temperature at the center of the ignition volume at the end of ignition duration in dependence of equivalence ratio for iso-octane/air mixture under atmospheric conditions

The flammability limits estimated in simulations are LFL = 0.92, and RFL = 4.5, expressed in equivalence ratio. Depending on the experimental apparatus used, the measured flammability limits in experiments are LFL = $0.62 - 0.87$, and RFL = $4.55 - 4.76$ in equivalence ratio [47, 61, 141]. The RFL estimated with a spherical geometry shows good agreement with the experiments. However, the LFL estimated with a spherical geometry is closer to stoichiometry compared to the LFL measured in the experiments. The reason here is that with spherical geometry, the stretch effect is over-predicted. Lean mixtures with Le > 1 are very sensitive to the stretch effect, with flame extinction frequently observed. In the experiments, flame extinction for lean mixtures can also be observed. This might be the reason that even the LFL measured in the experiments has a difference of about 30%. According to Liu et al. [55], for mixtures with an equivalence ratio $\phi < 0.8$, flame propagation can only be observed when using an ignition energy of $E = 3000\,\mathrm{mJ}$, which is several thousand times larger than the MIE for stoichiometric and rich mixtures. With such an enormously large ignition energy, turbulent flame can be observed, even though the ignition energy was deposited in quiescent

mixtures [55]. The next two sections will discuss in detail how the stretch effect affects the MIE of PRFs.

5.3 Dependence of MIE on Geometry

As explained earlier, the Lewis number of PRF/air mixtures varies significantly from lean to rich mixtures, making curvature a crucial factor in the induced ignition process. To accurately capture the curvature effect on the induced ignition of PRF/air mixtures, the dependence of MIE on ignition kernel geometry was investigated.

The dependence of minimum ignition energy density (for flame propagation) on equivalence ratio at 1 bar and $T_0 = 298\,\mathrm{K}$ for iso-octane/air mixture using curved geometries ((a) spherical geometry, (b) cylindrical geometry) with 2 ignition radii ($r_s = 0.5\,\mathrm{mm}$ and $r_s = 1.0\,\mathrm{mm}$) is shown in Fig. 5.12. Similar to the results of methane, in the range of $\phi = 1.5$ to $\phi = 3.0$, $q_{s,min}$ has only a weak dependence on ignition radius and on geometry. $q_{s,min}$ for small r_s is slightly higher because of diffusion. Starting from $\phi = 3.0$, $q_{s,min}$ increases as it approaches the rich flammability limit.

However, for $\phi < 1.5$, a notable dependence of $q_{s,min}$ on ϕ can be observed: $q_{s,min}$ increases rapidly with decreasing ϕ, especially for small r_s, even within the flammability limit. A surprising outcome is that for spherical geometry with $r_s = 0.5\,\mathrm{mm}$, flame propagation is never observed, even for the stoichiometric mixture, regardless of how large the ignition energy is. In contrast, for cylindrical geometry, the U-shaped curve is flatter and wider compared to spherical geometry with the same ignition radius. A possible reason is related to stretch.

These results illustrate the influence of stretch effect on the ignition and early flame propagation processes for iso-octane/air mixtures. With the definition of stretch rate in [71]:

$$\kappa_{sph} = \frac{2}{r_f}\frac{dr_f}{dt}, \tag{5.1}$$

and

$$\kappa_{cyl} = \frac{1}{r_f}\frac{dr_f}{dt}, \tag{5.2}$$

where r_f is the flame radius, the stretch rate of a cylindrical flame at same flame radius and same propagation speed is smaller than spherical flame. Thus, the stretch effect has a less pronounced influence on cylindrical flames

than on spherical flames. Consequently, the minimum ignition energy density required for cylindrical geometry at the same r_s and ϕ is smaller than for spherical geometry. Additionally, flame propagation can be observed at a smaller ϕ for cylindrical geometry compared to spherical geometry.

At the rich side, the estimated RFL for iso-octane/air mixtures demonstrates good agreement with experimental data, irrespective of geometry (excluding the case with spherical geometry and $r_s = 0.5\,\mathrm{mm}$). Conversely, at the lean side, the estimated LFL for iso-octane/air mixtures exhibits strong dependence on geometry and ignition radius. The experimental results of the LFL in Ref. [61] lie between the LFL estimated with spherical geometry and that estimated with cylindrical geometry. This result is not surprising, as experiments show the flame geometry is not perfectly cylindrical or spherical, but rather a three-dimensional shape between a sphere and a cylinder. The finding that the estimated RFL for iso-octane/air mixtures aligns well with experimental data, while the LFL depends on geometry, contrasts with the behavior observed in methane/air mixtures. The discrepancy arises from the opposite trend in the dependence of Le on ϕ between PRF/air and methane/air mixtures. Specifically, for lean methane/air and rich PRF/air mixtures, $Le < 1$, indicating minimal influence of stretch effect on the flame. Conversely, for rich methane/air and lean PRF/air mixtures, $Le > 1$, indicating significant sensitivity of the flame to the stretch effect.

5.4 Dependence of MIE on Ignition Radius

Since the ignition radius directly determines the ignition volume, it is a key factor influencing MIE. As an example, the dependence of MIE on ignition radius for rich iso-octane/air mixture at atmospheric conditions is shown in Fig. 5.13. In this case, $\mathrm{MIE_{prop}} = \mathrm{MIE_{ini}}$ decreases with decreasing ignition radius, closely following the $E \sim r_s^3$ trend, with slight discrepancies at small ignition radii. To heat the mixture within the ignition volume to the minimum ignition temperature, enabling flame kernel formation, a minimum ignition energy density is required. Given that $E_{ig} = V_{ig} \cdot q_{ig}$, and since q_{ig} is nearly independent of ignition radius, $\mathrm{MIE_{ini}}$ is expected to be quasi-proportional to V_{ig}, which scales with the cube of the ignition radius. For $r_s < 1$,mm, the ignition radius becomes so small that heat loss through conduction outside the ignition volume may result in a temperature decrease at the center. This increases the required $\mathrm{MIE_{ini}}$ to offset the heat loss and facilitate flame kernel formation, compared to cases with larger ignition radii. Additionally, since the rich iso-octane/air mixture has a Lewis number smaller than 1, the stretch

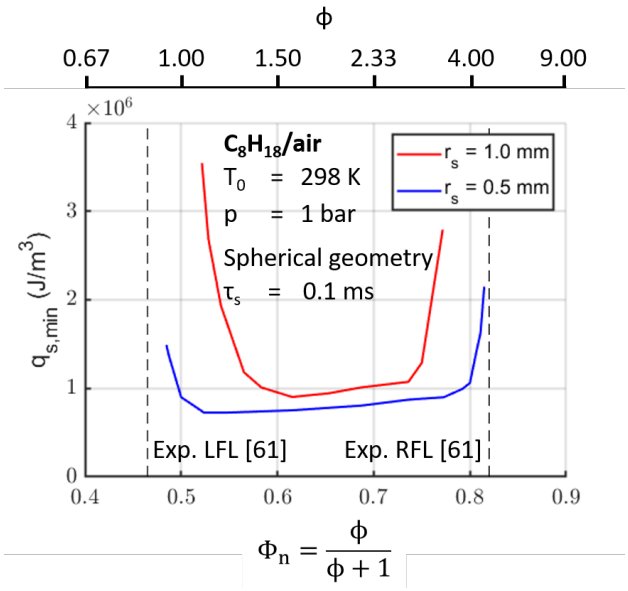

(a) Spherical geometry

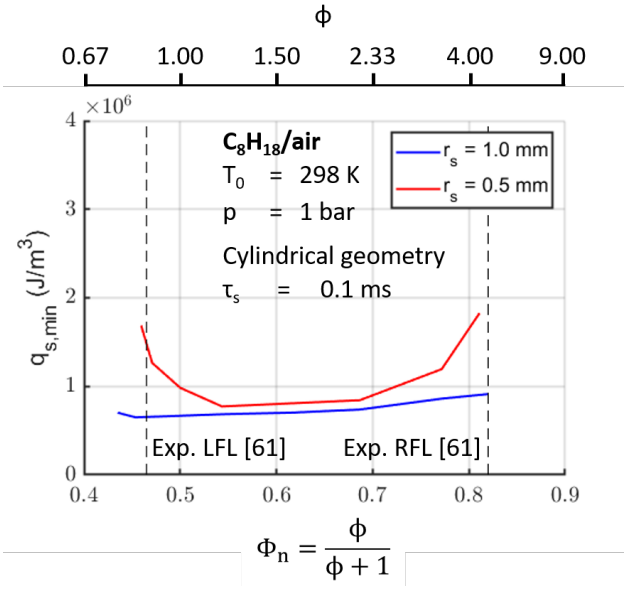

(b) Cylindrical geometry

Figure 5.12: The dependence of minimum ignition energy density on equivalence ratio at 1 bar and $T_0 = 298\,\mathrm{K}$ for iso-octane/air mixture with curved geometries [129]. Black dashed lines: LFL and RFL measured in experiments [61].

effect accelerates the outward propagation of the flame front. The successful formation of a flame kernel ensures self-sustained flame propagation [71], meaning that flame scenario II does not occur, and $\mathrm{MIE_{prop}} = \mathrm{MIE_{ini}}$.

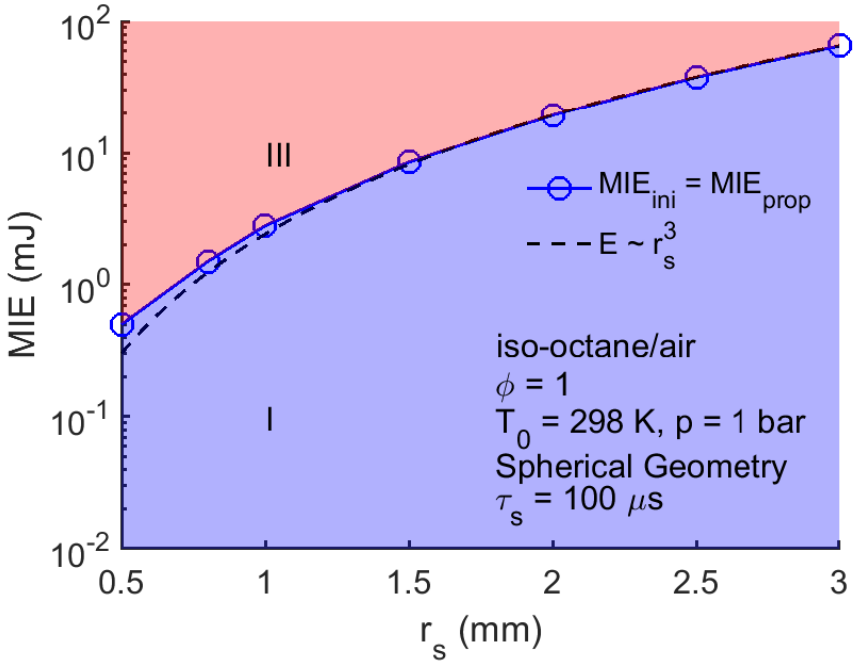

Figure 5.13: Dependence of MIE on ignition radius for rich iso-octane/air mixture at $T_0 = 298$ K and p = 1 bar

The dependence of MIE on ignition radius for $Le > 1$ mixtures is more complex compared to $Le < 1$ mixtures, as the ignition radius affects not only the ignition volume but also the curvature effect. As an example, stoichiometric iso-octane/air mixture under atmospheric conditions is shown in Fig. 5.14. At large ignition radii ($r_s > 1.2\,\mathrm{mm}$), similar to the rich mixture, $\mathrm{MIE_{prop}}$ equals $\mathrm{MIE_{ini}}$ and closely follows the $E \sim r_s^3$ curve and decreases with decreasing ignition radius. In this regime, a formed flame kernel is always self-sustained, and the primary factor influencing the dependence of MIE on ignition radius is the ignition volume. In the range $0.8\,\mathrm{mm} < r_s < 1.2\,\mathrm{mm}$, stretch effect starts to cause flame extinction, resulting in $\mathrm{MIE_{prop}}$ being higher than $\mathrm{MIE_{ini}}$ and nearly independent of the ignition radius. At small ignition radii ($r_s < 0.8$,mm), although ignition of the mixture is possible, flame propagation cannot be observed regardless of the ignition energy.

The stretch effect on early flame propagation process of iso-octane/air mistures is explained as followings. For mixtures with Le > 1, such as

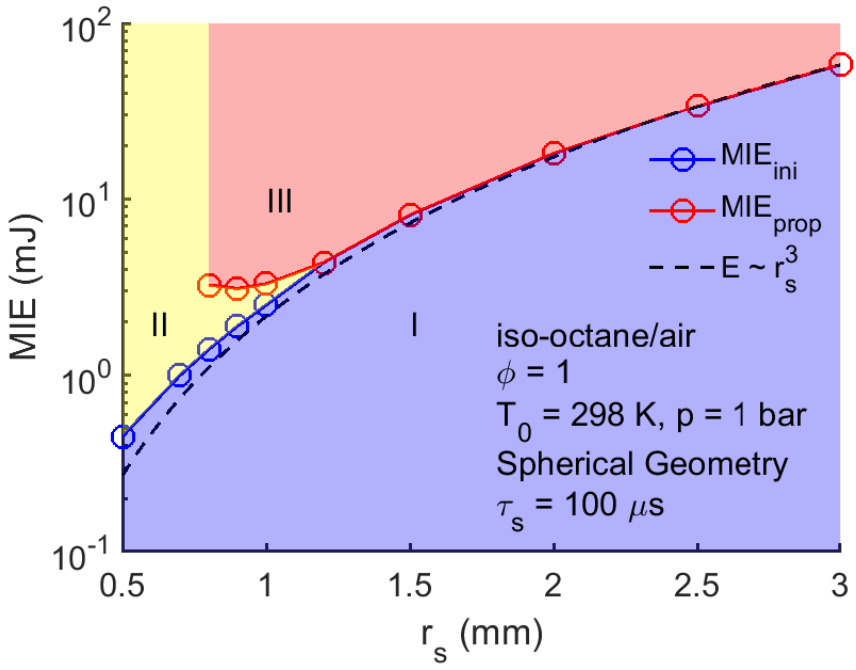

Figure 5.14: Dependence of MIE on ignition radius for stoichiometric iso-octane/air mixture at $T_0 = 298$ K and p = 1 bar [129]

stoichiometric and lean PRF/air mixture, the stretch effect causes a decrease in flame temperature, which might lead to flame extinction. Excess enthalpy from an external source must be supplied to help the flame survive during the critical phase. In this case, there exists a critical radius, beyond which the flame becomes self-sustained [24]. With the definition of the critical flame radius corresponding to the position where the propagation speed of the flame reaches its minimal value [24], the critical radius for a stoichiometric iso-octane/air mixture at atmospheric conditions with spherical geometry is about 3 mm, as shown in Fig. 5.15. For the case where $r_s = 1\,\text{mm}$, $\text{MIE}_{\text{ini}} = 2.70\,\text{mJ}$. However, with this ignition energy, the flame only reaches a radius of about 2 mm before quenching. As the ignition energy increases, the flame can reach a larger radius. However, as long as this radius remains smaller than the critical flame radius, the flame still quenches. When the ignition energy reaches 3.4 mJ, the flame can finally reach the critical radius and become self-sustained. In this case, the mixture in the ignition volume has to be heated up to 3000 K, which is about 700 K higher than the temperature reached when a flame kernel is formed and quenches. This results in a higher MIE_{prop} than the MIE_{ini}.

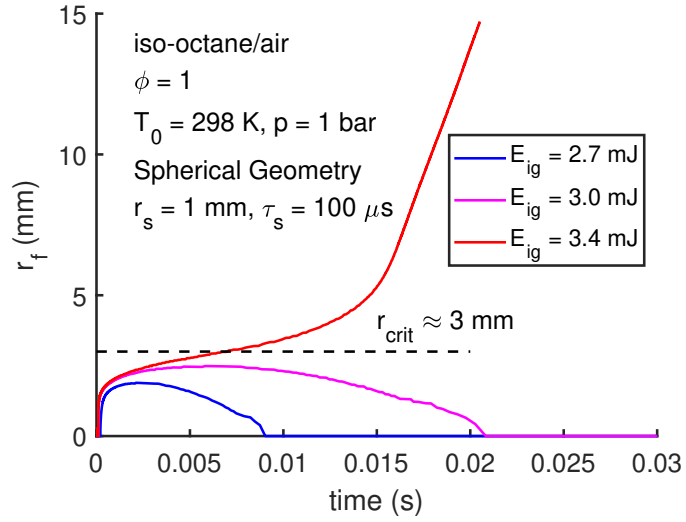

(a) Flame radius

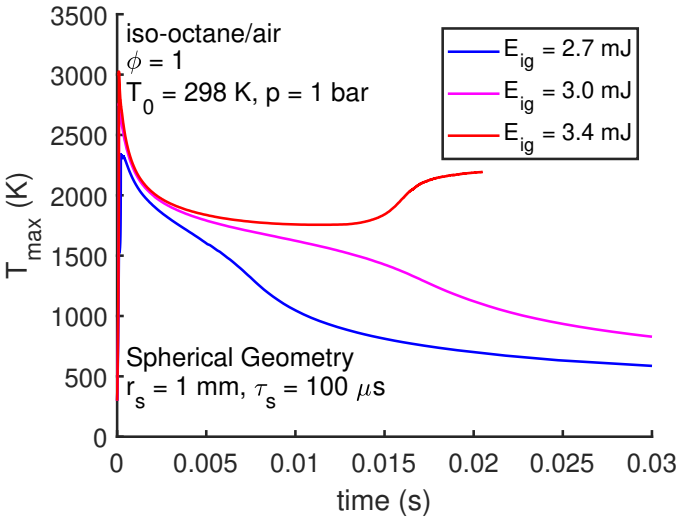

(b) Maximum Temperature

Figure 5.15: Temporal development of the flame radius and of the maximal temperature for stoichiometric iso-octane/air mixtures with a spherical source $r_s = 1\,\mathrm{mm}$ [129]

For a large r_s ($r_s > 1.2\,\text{mm}$), the flame radius after ignition duration is already very close to, or even larger than, the critical radius. In this case, MIE_{prop} equals MIE_{ini}.

However, if r_s further decreases ($r_s < 0.8\,\text{mm}$), flame propagation can not be observed, even the ignition energy is really large. As is shown in Fig. 5.16, even when the mixture in the ignition volume is heated up to about 10000 K, the flame still can't reach the critical radius $r_{crit} = 3\,\text{mm}$. In this case, although the mixture can be ignited, a flame propagation is not observed, no matter how large the ignition energy is.

5.5 Dependence of MIE on Pressure

Up to this point, the investigations have been conducted at 1 bar. However, in practical applications, induced ignition often occurs at elevated pressures. The question to be addressed in this section is how pressure affects the MIE.

The dependence of MIE on pressure for a lean n-heptane/air mixture is shown in Fig. 5.17. A small ignition radius ($r_s = 0.5\,\text{mm}$) is chosen because, with a larger ignition radius, the flame extinction scenario (scenario II) might not be observed even at low pressure.

At low pressures (1-5 bar), flame extinction can be observed due to the large diffusion caused by the curvature effect, $\text{MIE}_{\text{prop}} > \text{MIE}_{\text{ini}}$. MIE_{ini} increases almost proportionally with increasing pressure because the density of the mixture in the ignition volume increases proportionally with pressure. Consequently, the mass of the fresh mixture in the ignition volume also increases proportionally with pressure, while the ignition radius remains constant. On the other hand, MIE_{prop} decreases with increasing pressure. As pressure increases, the heat release from chemical reactions becomes faster and diffusion slows down. Consequently, the curvature effect becomes less significant with increasing pressure. The reduced significance of the curvature effect at 3 bar is illustrated in Fig. 5.18, which shows flame propagation at 1 bar and 3 bar. It is clearly observed that while the flame at atmospheric pressure experiences a critical phase, caused by the curvature effect, with slow flame speed until about 0.02 s, the flame at 3 bar starts to propagate at a high flame speed almost from the beginning. A similar conclusion, that the chemical heat release is stronger at higher pressures than at 1 bar, can also be illustrated by the results showing that the excitation time during ignition decreases with increasing pressure. The excitation time, which describes the period between the start of rapid heat release and the time of maximum power, indicates the speed of energy release [57, 78]. As a result, less excess

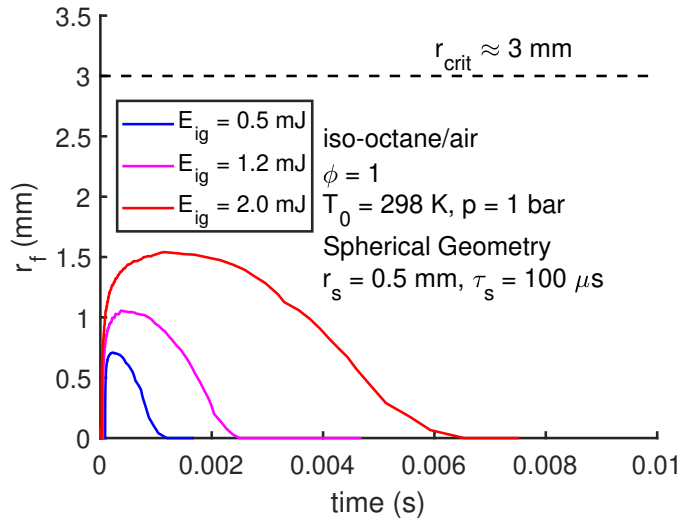

(a) Flame radius

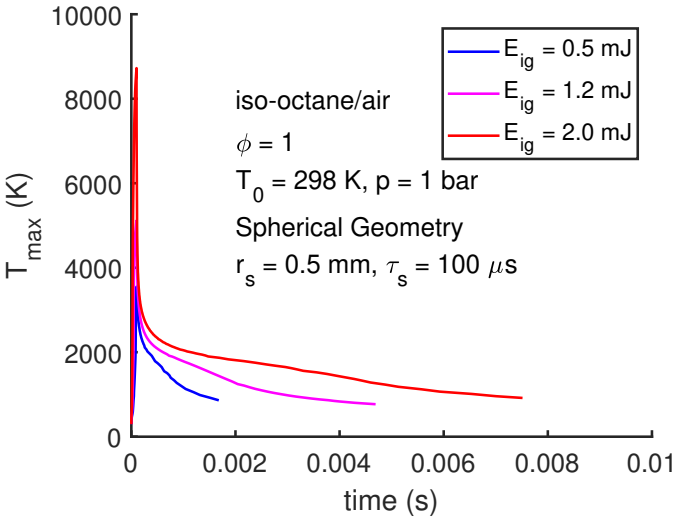

(b) Maximum Temperature

Figure 5.16: Temporal development of the flame radius and of the maximal temperature for stoichiometric iso-octane/air mixtures with a spherical source $r_s = 0.5\,\mathrm{mm}$ [129]

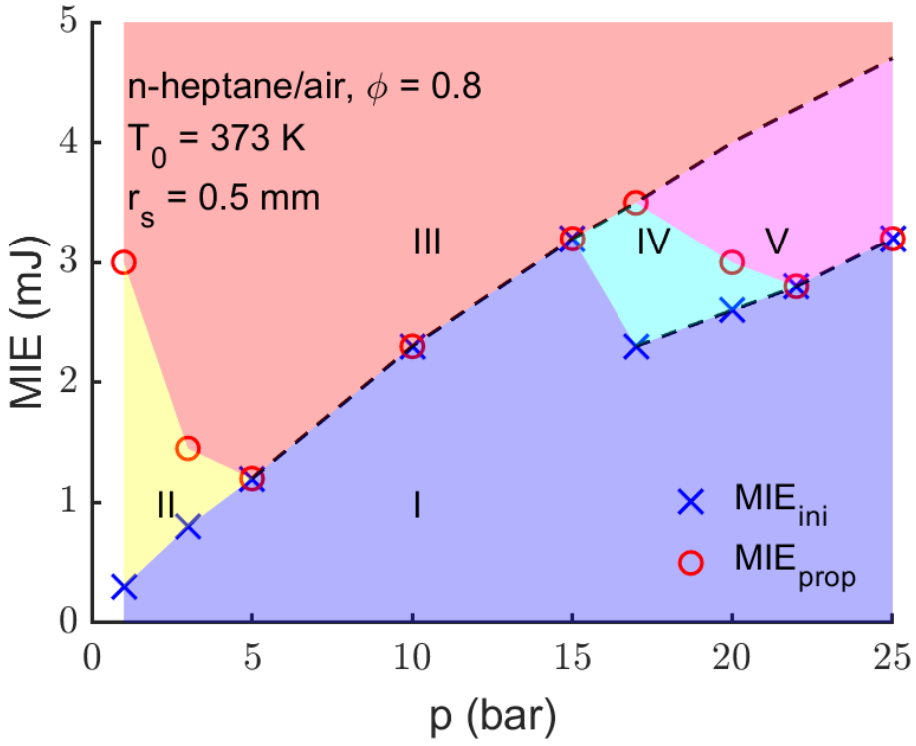

Figure 5.17: Dependence of MIE of a lean n-heptane/air mixture ($\phi = 0.8$) on pressure at $T_0 = 373$ K, using spherical geometry with $r_s = 0.5\,\mathrm{mm}$.

enthalpy from the ignition source is needed for flame propagation at high pressure (compared to 1 bar), resulting in a smaller $\mathrm{MIE_{prop}}$.

Starting from $p = 5$ bar, the curvature effect on the early flame propagation of n-heptane flame is negligibly small, and flame extinction is not observed. $\mathrm{MIE_{prop}}$ equals $\mathrm{MIE_{ini}}$ and increases with pressure due to the increasing density.

Starting from $p = 15$ bar, the low-temperature chemistry of n-heptane becomes significant, resulting in a sudden drop in $\mathrm{MIE_{ini}}$ because a cool flame can be initiated at a lower MIE compared to a hot flame. However, since the temperature of the cool flame is only about 700 K, the low-temperature reactions can only provide weak heat release, leading to cool flame extinction. Successful flame propagation still requires the ignition energy to reach the MIE of a hot flame.

The low-temperature chemistry also intensifies with increasing pressure. If the pressure reaches approximately 22 bar, the cool flame can persist, triggering a second stage of ignition and eventually transitioning into a hot

flame. Again, MIE_{prop} equals MIE_{ini} and increases with pressure due to the increasing density.

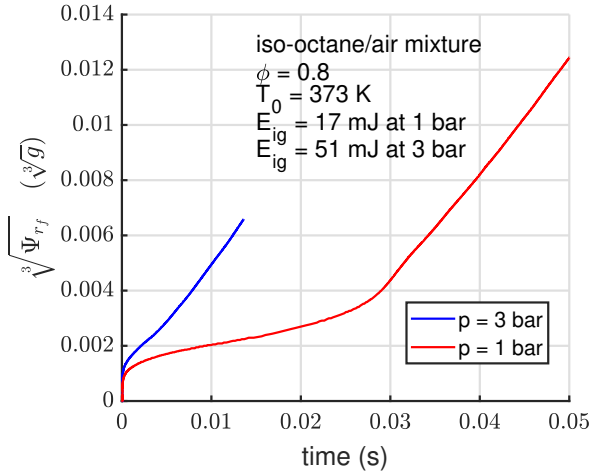

Figure 5.18: Flame propagation of lean n-heptane/air flame at 1 bar and at 3 bar

The selected ignition radius significantly influences the curvature effect and the occurrence of flame scenario II, flame extinction, as the curvature effect strongly relies on the curvature (which is the reciprocal of the radius) of the flame. The ignition radius, below which flame scenario II exists, decreases with pressure. At 1 bar, flame extinction for n-heptane flame can be observed below $r_s = 1$ mm, while at 5 bar, it can only be observed below $r_s = 0.5$ mm.

Similar results were also observed in the work of Maas et al.[80] for hydrogen/oxygen mixtures and from Yang et al.[136] for DME/air mixtures. However, in other investigations (see, e.g., [28, 105]), a contrary tendency (MIE decreases with increasing pressure) was observed. The reason is that, in numerical simulations, r_s is kept constant, resulting in a constant V_s. Consequently, the MIE increases as ρ increases with increasing pressure. On the other hand, in experiments, the gap between the electrodes is adjusted at each pressure to reach the MIE. At elevated pressures, ignition can be achieved with a much smaller gap compared to 1 bar. The mass of the mixture in the ignition volume shows a decreasing tendency with increasing pressure, and so does the MIE.

The determination of MIE_{prop} with varying r_s is shown at 5 bar as an example in Fig. 5.19. As explained in the last section, MIE_{prop} is proportional to r_s^3 at large r_s. At small r_s, however, the curvature effect causes flame extinction and results in a slower decrease in MIE_{prop} with decreasing r_s. At

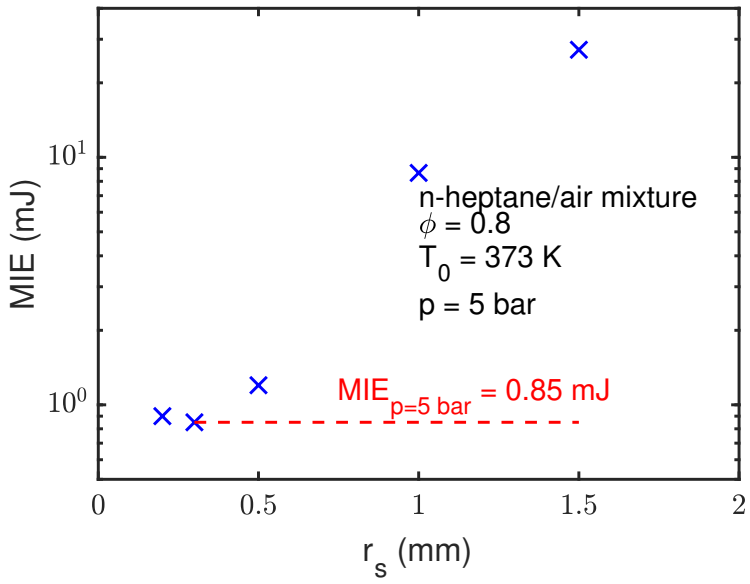

Figure 5.19: Determination of $\mathrm{MIE_{prop}}$ for lean n-heptane/air mixtures with $\phi = 0.8$ at $T_0 = 373$ K and $p = 5$ bar

about $r_s = 0.3$ mm, the $\mathrm{MIE_{prop}}$ reaches a minimal value. After that, even if r_s reduces, $\mathrm{MIE_{prop}}$ does not decrease any more. This $\mathrm{MIE_{prop}} = 0.85$ mJ is then defined as the $\mathrm{MIE_{p=5bar}}$.

With the definition of MIE at each pressure with varying ignition radii, the MIE shows a decreasing tendency with increasing pressure, as shown in Fig. 5.20, which is in agreement with the experimental results.

5.6 Dependence of MIE on RON

So far, the ignition characteristics of n-heptane/air and iso-octane/air mixtures have been extensively studied, revealing insights into how various ignition parameters influence these fuels. However, the ignition behavior of PRFs remains relatively unexplored, particularly regarding the impact of fuel mixture components representing by RON. To address this gap, this section investigates the influence of RON, on the MIE of PRFs.

In this section, the equivalence ratio of the fuel/air mixture is set to $\phi = 0.8$. This choice is based on two primary considerations: Firstly, lean combustion is widely recognized for its high efficiency and low emissions, making it an attractive technology for various applications. Secondly, it is essential to

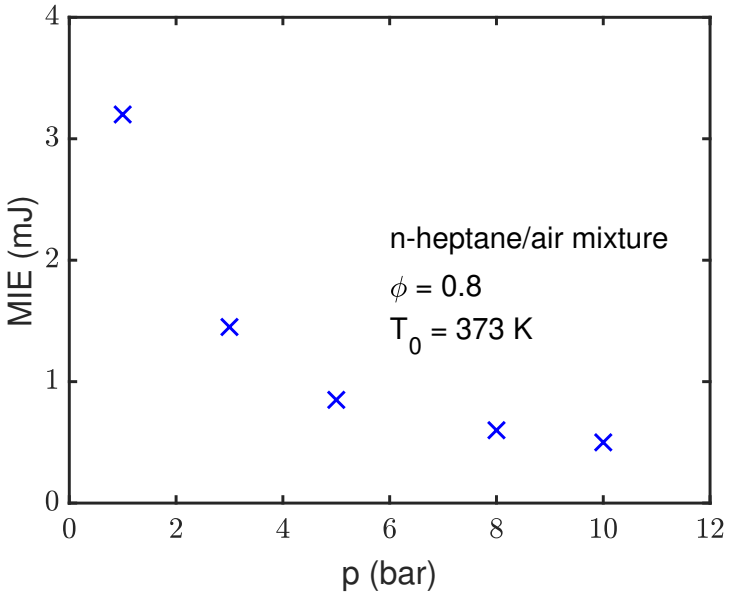

Figure 5.20: Dependence of MIE on pressure with varying ignition radii for lean n-heptane/air mixtures with $\phi = 0.8$ at $T_0 = 373$ K

investigate the stretch effect of lean PRF/air flames, particularly due to the mixture's large Lewis number ($Le \approx 3$ for $\phi = 0.8$ mixture according to [72]).

5.6.1 Dependence of MIE on RON at Atmospheric Pressure

The dependence of MIE on RON at $T_0 = 373$ K and p = 1 bar using spherical geometry with various ignition radii is shown in Fig. 5.21. Since the flame extinction is often observed, both MIE_{ini} and MIE_{prop} are shown in the figure.

For all investigated ignition radii, MIE_{ini} shows little dependence on RON. However, a distinct dependence on both RON and ignition radius is observed for MIE_{prop}:

- In cases with a large ignition radius ($r_s = 2.0$ mm), both MIEs coincide across the entire RON range. This suggests that the ignition radius is sufficiently large for all formed flame kernels to develop into self-sustained flames. Consequently, Flame scenario II does not occur, and MIE_{prop} remains relatively independent of RON.

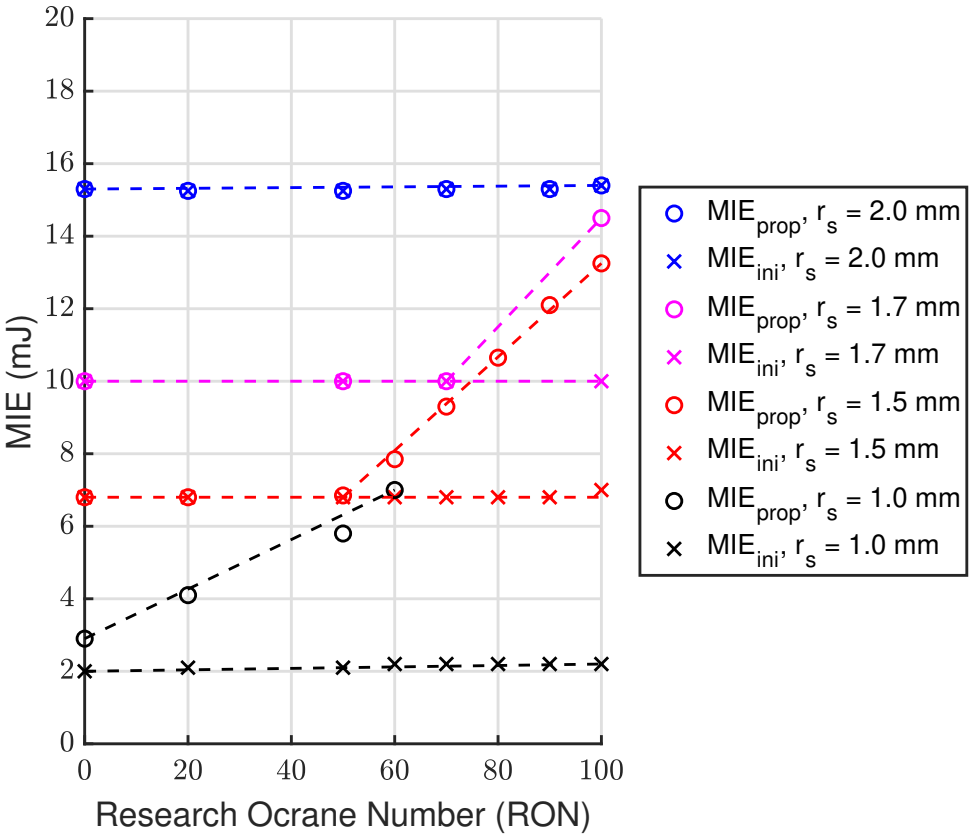

Figure 5.21: Dependence of MIE on RON at $T_0 = 373$ K and $p = 1$ bar, using spherical geometry with various ignition radii. Dashed lines are drawn to guide the eye.

- Conversely, for smaller ignition radii ($r_s = 1.7$ mm and $r_s = 1.5$ mm), an upturn occurs in the $\mathrm{MIE_{prop}}$ curve. The RON value at this upturn is defined as $\mathrm{RON_{lim}}$.
  - When $\mathrm{RON} \leq \mathrm{RON_{lim}}$, both MIEs coincide and do not vary with RON, indicating the absence of Flame scenario II.
  - For $\mathrm{RON} > \mathrm{RON_{lim}}$, $\mathrm{MIE_{prop}}$ increases with RON, while $\mathrm{MIE_{ini}}$ remains constant. This suggests the presence of Flame scenario II for mixtures with $\mathrm{RON} > \mathrm{RON_{lim}}$, indicating the need for excess external energy for steady flame propagation. The greater the proportion of iso-octane in the mixture, the greater the excess external energy required for sustaining a flame.

- In the case of $r_s = 1.0$ mm, flame extinction can be observed even for n-heptane/air mixtures. Here, $\mathrm{MIE_{prop}} > \mathrm{RON_{lim}}$ and increases with RON from RON = 0. Notably, the MIE data is limited to RON = 60. Beyond this value, flame quenching consistently occurs, even under conditions of infinitely high ignition energy, preventing the observation of a self-sustained flame.

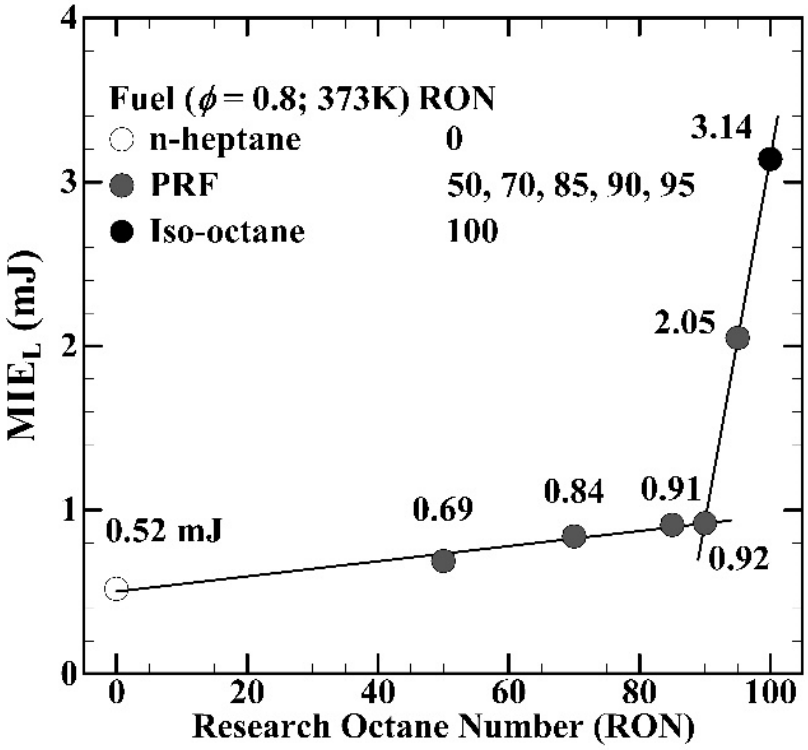

Figure 5.22: Dependence of MIE on RON at $T_0 = 373$ K and $p = 1$ bar in experiments. Dashed lines are drawn to guide the eye. [128]

The experimental results depicted in Fig. 5.22 corroborate numerical findings. As previously noted, the MIE measured in experiments corresponds to $\mathrm{MIE_{prop}}$ in simulations. Notably, the experimental data demonstrates a significant increase in MIE for PRF/air mixtures with RON > 90, indicating a distinct upturn. Conversely, for mixtures with RON $\leq$ 90, the increase in MIE is relatively minor. These experimental findings align with the concept of $\mathrm{RON_{lim}}$ identified in the simulations, suggesting a qualitative agreement between experimental and numerical results. Simulations with another mechanism, developed by Wang et al.[122], which would be provided in Appendix,

also confirmed the existence of the bend. However, quantitative comparisons are challenging due to differences in ignition and flame geometry and the complexities involved in estimating ignition radius in experimental setups.

To investigate the reason of this phenomenon, the influencing factors of MIE and their dependence of RON are investigated.

Specific heat capacity

A simple numerical experiment was conducted to compare the specific heat capacity of n-heptane and iso-octane, where all chemical reactions were eliminated from the reaction mechanism. In this experiment, the gas mixture was solely heated. Using a spherical geometry with $r_s = 1.5\,\mathrm{mm}$ and an external ignition energy of $E_{ig} = 6.9\,\mathrm{mJ}$, corresponding to the $\mathrm{MIE_{ini}}$ for iso-octane, the n-heptane/air mixture can be heated up to a temperature of $T = 1106\,\mathrm{K}$, while the iso-octane/air mixture can be heated up to a temperature of $T = 1093\,\mathrm{K}$. The negligible difference in temperature after heating (approximately 1%) indicates similar c_p values for both fuels.

Ignition Delay Time

At a temperature of $T = 1100\,\mathrm{K}$ and a pressure of $p = 1\,\mathrm{bar}$, the ignition delay time of the n-heptane/air mixture ($\phi = 0.8$) is $\tau_{ig} = 4.99\,\mathrm{ms}$, while for the iso-octane/air mixture ($\phi = 0.8$) it is $\tau_{ig} = 5.26\,\mathrm{ms}$, only about 5% larger than that of n-heptane.

Due to the similar c_p values and similar ignition delay times at same temperature (at high temperature ranges) of iso-octane and n-heptane, the $\mathrm{MIE_{ini}}$ almost does not depend on RON.

Curvature Effect

As explained in Chapter 3, flame extinction might be caused by the stronger dissipation of spherical geometry compared to planar geometry. To investigate the contribution of curvature effect on the dependence of MIE on RON, MIE with planar geometry is calculated. For planar geometry with infinite area, the ignition volume is adjusted to match that of spherical geometry.

Results presented in Fig. 5.23 clearly demonstrate that the curvature effect is a necessary condition for the existence of the upturn at $\mathrm{RON_{lim}}$ for $\mathrm{MIE_{prop}}$. Without curvature, both MIEs coincide across the entire range of RON, rendering flame scenario II nonexistent for all mixtures. However, since the curvature effect poses a challenge for all lean PRF/air mixtures, and

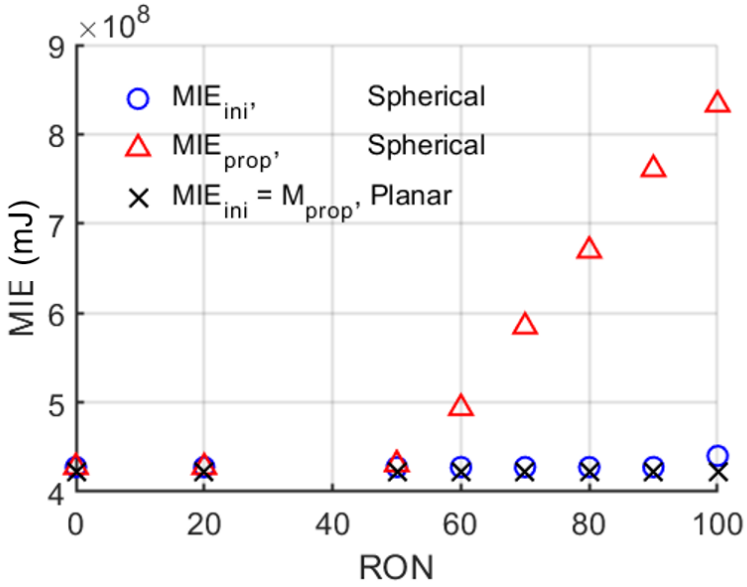

Figure 5.23: Dependence of MIE on RON for spherical and planar geometry, $\phi = 0.8$, $T_0 = 373$ K and $p = 1$ bar. [128]

flame scenario II is only observed for mixtures with RON $>$ RON$_{\text{lim}}$, it is not sufficient alone to explain the existence of the upturn.

Low Temperature Kinetics

In the high-temperature range, the chemical kinetics of all PRFs are similar. However, the chemical kinetics of n-heptane in the low-temperature range, where reactions with peroxidic radicals dominate, are much faster than those of iso-octane [17, 31].

To investigate whether these chemical reactions involving peroxidic radicals in the low-temperature range are the reason why PRF flames with RON $<$ RON$_{\text{lim}}$ can survive during the critical phase, all simulations were repeated under the same conditions. However, an edited reaction mechanism was used where all reactions involving peroxidic radicals were eliminated.

It can be clearly seen in Fig. 5.24 that both MIEs remain unaffected, regardless of whether reactions involving peroxidic radicals are present or not. This indicates that the upturn at RON$_{\text{lim}}$ at 1 bar cannot be attributed to the faster low-temperature kinetics of n-heptane.

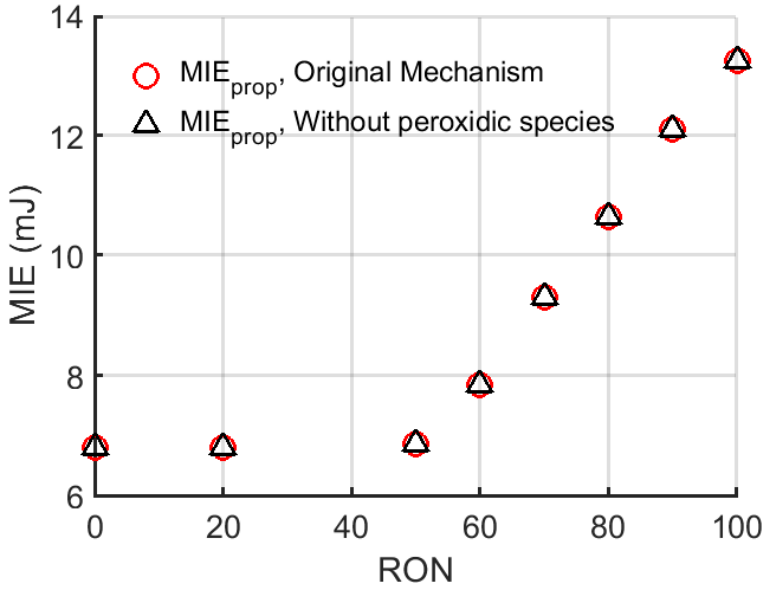

Figure 5.24: Dependence of MIE on RON for spherical geometry with the original mechanism and with the mechanism without low temperature chemistry, $\phi = 0.8$, $T_0 = 373$ K and $p = 1$ bar. [128]

Reaction Pathways of iso-octane and n-heptane

As described in Sec. 5.1, the PRF flame initially propagates slowly during the critical phase, where HO_2 and H_2O_2 radicals play significant roles. Once the flame reaches the critical radius, it propagates rapidly, with OH radicals dominating. Since flame extinction occurs during the critical phase, where HO_2 radicals are important for the production of OH, the consumption pathways of HO_2 radicals for iso-octane and n-heptane flames are investigated.

The primary HO_2 consumption reactions with the highest reaction rates for both iso-octane and n-heptane flames in the reaction mechanism of Andrae et al. [5] are listed below:

R636: $HO_2 + H \longrightarrow OH + OH$
R640: $HO_2 + O \longrightarrow OH + O_2$
R642: $HO_2 + OH \longrightarrow H_2O + O_2$
R644: $HO_2 + HO_2 \longrightarrow H_2O_2 + O_2$

The consumption rates of HO_2 for slow flames of iso-octane and n-heptane flame through these reactions are plotted against temperature in Fig. 5.25.

The reaction $HO_2 + H \longrightarrow OH + OH$ is the dominant reaction in the consumption of HO_2 for fast flames of both iso-octane and n-heptane. However,

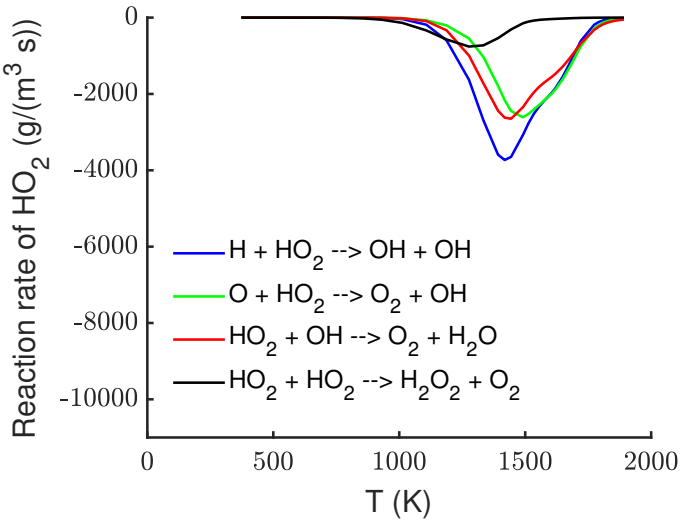

(a) slow iso-octane flame

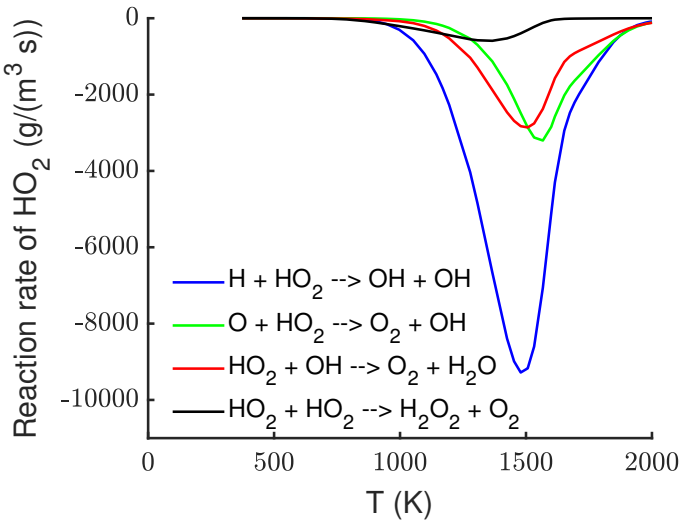

(b) slow n-heptane flame

Figure 5.25: The reaction rates of main HO_2 consumption reactions for a slow iso-octane flame and a slow n-heptane flame at $\phi = 0.8$, $T_0 = 373$ K, and $p = 1$ bar, with spherical geometry ($r_s = 1.5$ mm, $\tau_s = 100\,\mu$s) [128]

for slow flames, the pathways of HO_2 consumption differ, as illustrated in Fig. 5.25. For the n-heptane slow flame, despite the lower flame temperature leading to lower reaction rates for all reactions in the slow flame, the reaction $HO_2 + H \longrightarrow OH + OH$ still dominates the consumption of HO_2, with a peak reaction rate almost 4 times higher than that of the chain termination reaction $HO_2 + OH \longrightarrow H_2O + O_2$. The reaction $HO_2 + H \longrightarrow OH + OH$ produces two OH radicals at the expense of one H radical and one less reactive HO_2 radical, thereby accelerating the total reaction rate. In contrast, for the iso-octane flame, the peak reaction rate of $HO_2 + H \longrightarrow OH + OH$ is only 1.3 times higher than that of $HO_2 + OH \longrightarrow H_2O + O_2$. This indicates that for the iso-octane slow flame, $HO_2 + OH \longrightarrow H_2O + O_2$ plays a much more significant role. This chain termination reaction consumes one OH radical and one HO_2 radical to produce two stable species, H_2O and O_2. As discussed earlier, $HO_2 + H \longrightarrow OH + OH$ governs the production of OH radical for the slow flame. In the case of the iso-octane flame, the consumption of HO_2 through $HO_2 + OH \longrightarrow H_2O + O_2$, instead of $HO_2 + H \longrightarrow OH + OH$, reduces the radical pool and may eventually lead to flame extinction.

Now, a new question arises: why does $HO_2 + H \longrightarrow OH + OH$ dominate the HO_2 consumption for the n-heptane slow flame, while $HO_2 + OH \longrightarrow H_2O + O_2$ assumes a more significant role in the iso-octane slow flame? To answer this question, the formation pathway of H radical, which is also consumed in $HO_2 + H \longrightarrow OH + OH$, for iso-octane and n-heptane slow flame is investigated.

The primary H formation reactions with the highest reaction rates for n-heptane flame in the reaction mechanism of Andrae et al. [5] are listed below:

R617: $OH + H_2 \longrightarrow H + H_2O$
R664: $CO + OH \longrightarrow H + CO_2$
R680: $M + HCO \longrightarrow H + CO + M$
R708: $CH_3 + O \longrightarrow H + CH_2O$
R866: $M + C_2H_5 \longrightarrow H + C_2H_4 + M$

Among the above listed reactions, R617, R664, R680 and R708 are also the dominant H formation reactions for iso-octane flames. However, the reaction rate of $M + C_2H_5 \longrightarrow H + C_2H_4 + M$ in the iso-octane flame is considerably smaller compared to that in the n-heptane flame. This discrepancy arises from the substantial production of C_2H_5 during n-heptane oxidation, whereas less C_2H_5 is produced during iso-octane oxidation, with CH_3 being the main product [81]. While $M + C_2H_5 \longrightarrow H + C_2H_4 + M$ plays a role in generating H radicals, its peak occurs in the lower temperature

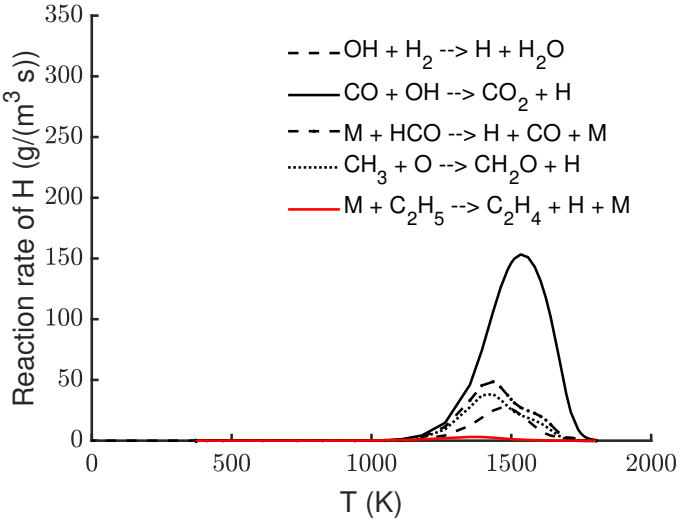

(a) slow iso-octane flame

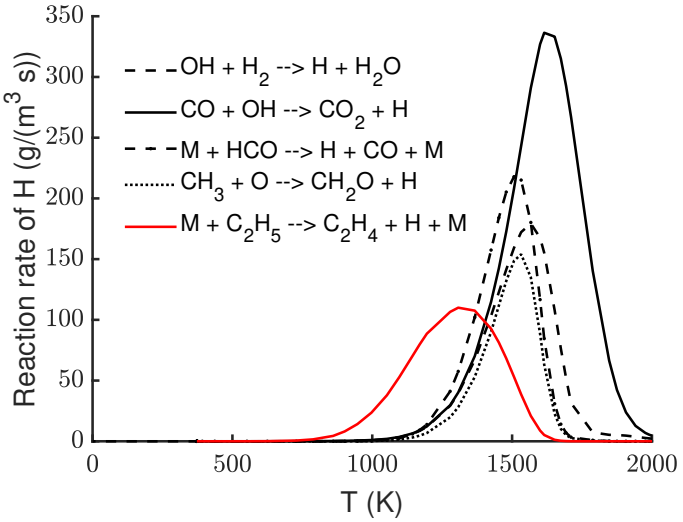

(b) slow n-heptane flame

Figure 5.26: Reaction rates of primary H formation reactions for slow iso-octane and slow n-heptane flames at $\phi = 0.8$, $T_0 = 373$ K, and $p = 1$ bar, with spherical geometry ($r_s = 1.5$ mm, $\tau_s = 100\,\mu$s) [128]

region (approximately 1200 K). Consequently, the reaction rate of M + C_2H_5 ⟶ H + C_2H_4 + M is not significantly affected in slow flames, where the flame temperature decreases due to curvature. Consequently, the reaction rate of M + C_2H_5 ⟶ H + C_2H_4 + M is not significantly affected in slow flames, where the curvature-induced decrease in flame temperature occurs.

During the critical phase, the large curvature induces enhanced diffusion of H radicals out of the reaction zone, consequently decreasing the concentration of H radicals within the reaction zone. In PRF flames with RON < RON_{lim}, the oxidation of n-heptane yields a substantial amount of C_2H_5 radicals, and the significant production of H radicals by M + C_2H_5 ⟶ H + C_2H_4 + M compensates for the rapid diffusion of H radicals. This ensures primary HO_2 consumption through the chain branching reaction: HO_2 + H ⟶ OH + OH, thereby enlarging the radical pool and facilitating the flame's survival through the critical phase. FConversely, in PRF flames with RON > RON_{lim}, less C_2H_5 is produced due to the smaller proportion of n-heptane in the fuel mixture. Without the additional H radicals generated by M + C_2H_5 ⟶ H + C_2H_4 + M, the lack of H radicals in the reaction zone retards the consumption of HO_2 through HO_2 + H ⟶ OH + OH, resulting in greater HO_2 consumption via the chain termination reactions R640: HO_2 + OH ⟶ H2O + O_2 and R644: HO_2 + HO_2 ⟶ H_2O_2 + O_2. Since OH radicals are primarily generated by HO_2 consumption reactions in slow flames, the direct consumption of HO_2 through chain termination reactions inhibits OH production and consequently retards radical pool growth, potentially leading to flame extinction. In such cases, a higher MIE_{prop} is required for sustained flame propagation. The higher the proportion of iso-octane in the fuel mixture (i.e., the higher the RON), the more HO_2 is consumed through chain termination reactions, necessitating a larger MIE_{prop} to supply the additional energy required for the flame to reach the critical radius.

5.6.2 Dependence of MIE on RON at Elevated Pressure

Due to its practical significance as the minimum energy required for a self-sustained flame, the dependence of MIE_{prop} on RON at different pressures is the focus of this section. As explained before, density in the ignition volume, which is proportional to the pressure, plays a significant role in MIE_{prop}. The only reason for this dependency is the fact that when the density becomes larger, more fresh mixture is heated during forced ignition, resulting in a lower temperature in the ignition volume. To focus on the interaction between chemical reactions and transport, the specific minimum ignition energy e_{min}, with a unit of J/g, is used in this section:

$$e_{min} = \frac{\mathrm{MIE_{prop}}}{\rho \cdot V_s} \tag{5.3}$$

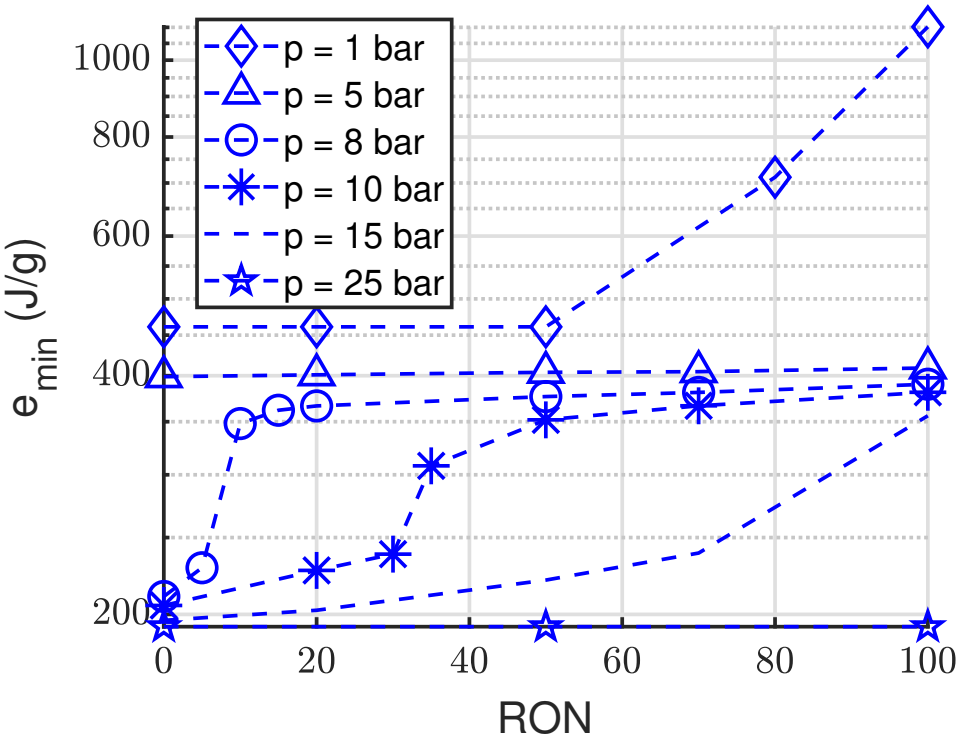

Figure 5.27: Dependence of e_{min} for flame propagation on RON for PRF/air mixtures with $\rho = 0.8$, using spherical geometry with $r_s = 1.5$ mm and $T_0 = 373$ K.

As shown in Fig. 5.27, the dependence of e_{min} on RON varies with different pressures. At 1 bar, this dependence results from the combined effects of curvature and the differing chemical mechanisms of n-heptane and iso-octane. At 5 bar, as the chemical heat release rate increases and diffusion slows down, flame scenario II cannot be observed for any PRF/air mixtures, and e_{min} no longer depends on RON.

Above 8 bar, the dependence of e_{min} on RON becomes evident again. e_{min} is first independent of RON at small RON values. Then, at about RON = 10, a sudden increase in e_{min} is evident. From about RON = 20, the rapid increase in e_{min} stops, and e_{min} becomes almost independent of RON again. As the pressure increases, the sudden increase of e_{min} shifts to higher RON. From $p = 25$ bar, the dependence of e_{min} on RON disappears again, and e_{min}

is almost constant throughout the RON range at a lower value (about 2 times smaller) compared to $p = 5$ bar.

To evaluate the role of LTC in ignition behavior at elevated pressures, we conducted simulations at 10 bar using a pseudo mechanism that excludes all reactions involving peroxidic species. This approach contrasts with the findings at 1 bar, where LTC was less critical. Results illustrated in Fig. 5.28 demonstrate that without LTC, the MIE's dependency on RON is eliminated, highlighting LTC's crucial role in ignition at higher pressures.

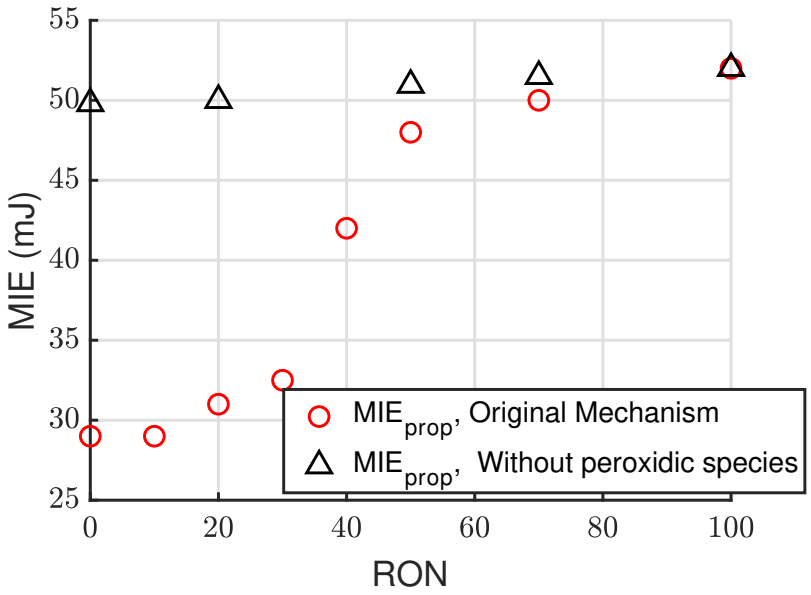

Figure 5.28: Dependence of MIE on RON at 10 bar, with or without peroxidic radicals, $\phi = 0.8$, $T_0 = 373$ K

Since the dependence of $e_{\min}$ on RON at elevated pressure lies in the LTC of PRFs, the cool flame structure of n-heptane and iso-octane was investigated. As is shown in Fig. 5.29, unlike the hot flame, where OH dominates the chain-branching reactions, H_2O_2, HO_2, and CH_2O species play a more important role in the cool flame for both mixtures. Significant differences in the flame structure for n-heptane and iso-octane cool flames can be observed. The peak concentrations of H_2O_2 and HO_2 species for the n-heptane cool flame are more than three times higher than those for the iso-octane cool flame. The importance of HO_2 and H_2O_2 for LTC can be seen in Fig. 5.30. Here, the reaction rates for primary OH formation reactions in a cool n-heptane flame are plotted against temperature. Plotting the reaction rates against the spatial coordinate was avoided due to the steep

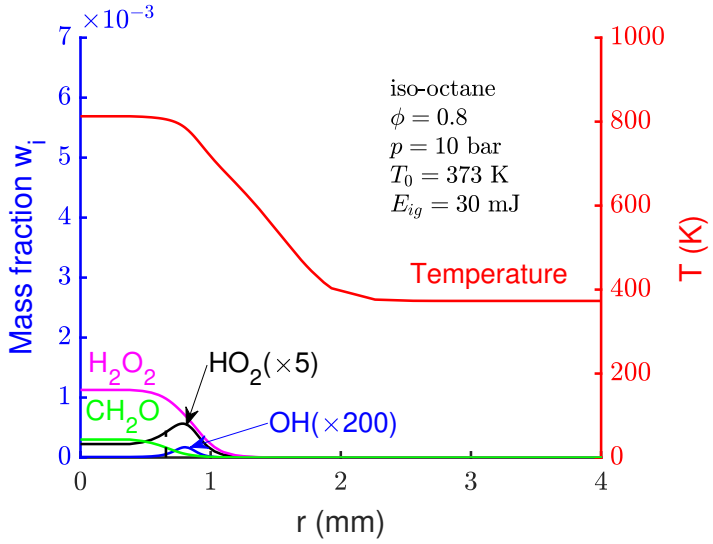

(a) cool iso-octane flame

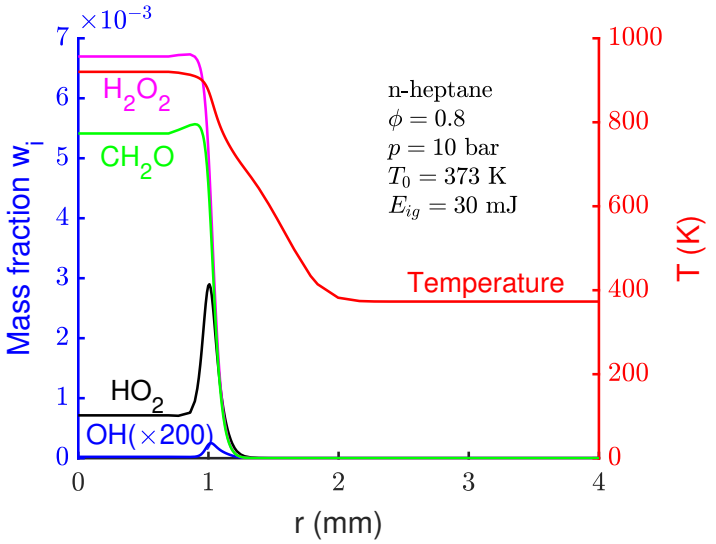

(b) cool n-heptane flame

Figure 5.29: The flame structure including the temperature profile and profile of the mass fraction of important species of cool n-heptane flame and cool iso-octane flame with $\phi = 0.8$, at $T_0 = 373$ K and $p = 10$ bar, with spherical geometry ($r_s = 1.5$ mm, $\tau_s = 100\,\mu$s).

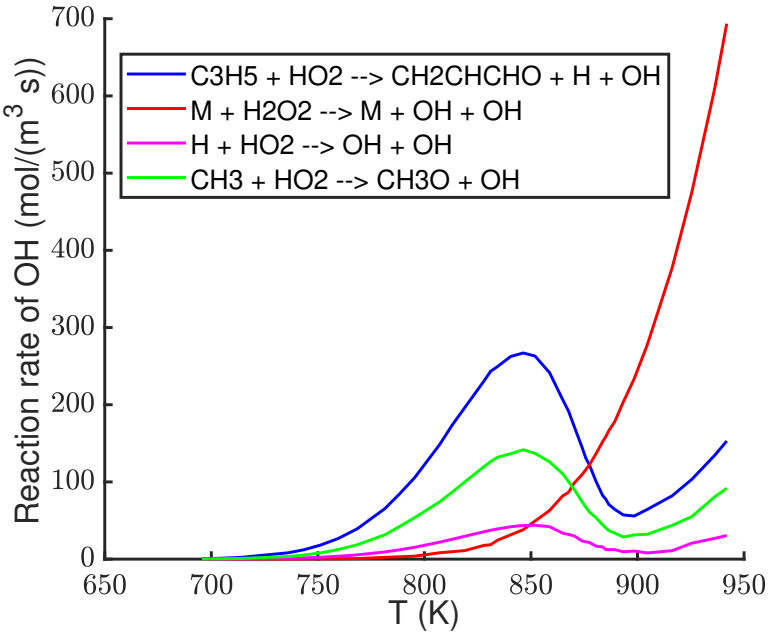

Figure 5.30: Reaction rate of important OH formation reactions for cool n-heptane flame, $\phi = 0.8$, $T_0 = 373$ K, $p = 10$ bar.

gradient that would result. HO_2 plays an important role in the formation of OH at low temperatures, with the reactions $CH_3 + HO_2 \longrightarrow CH_3O + OH$, $C_3H_5 + HO_2 \longrightarrow CH_2CHCHO + H + OH$, and $HO_2 + H \longrightarrow OH + OH$ being the most important OH formation reactions in the reaction zone. Additionally, the decomposition of H_2O_2 significantly aids the formation of OH in the temperature range of 900–950 K. Moreover, CH_2O is important for the heat release of the cool flame through the reaction $CH_2O + OH \longrightarrow HCO + H_2O$ [98].

This result confirms the more pronounced LTC of n-heptane flame compared to iso-octane flame. For the cool flame of PRF with small RON, the formed OH radical and the chemical heat release from the LTC of n-heptane helps it to evolve into a hot flame. This means, at 10 bar, for PRF/air mixtures with RON < 20, the MIE for a cool flame is enough for a self-sustained flame propagation. However, with the increase of iso-octane in the mixture, since the small amount important species retards the formation of OH and the chemical heat release, the cool flame quenches. Larger MIE is needed for the second stage ignition of PRF with large RON, hence the sudden increase of MIE exists. For the PRFs with RON > 50, the ignition energy still has to reach the MIE of the hot flame for a flame propagation.

With a further increase in pressure, the LTC of iso-octane becomes more pronounced. PRF with higher RON can achieve self-sustained flame propagation with only the MIE of the cool flame. The sudden increase in MIE shifts to higher RON values. At pressures of 25 bar and above, the LTC of iso-octane becomes so intense that even pure iso-octane can achieve self-sustained flame propagation with only the MIE of the cool flame. Consequently, the dependence of MIE on RON disappears.

5.7 Stochastic Behaviour of the Ignition Process

As explained in Sec. 2.3.1, unlike the simulation results, the MIE measured in experiments does not have a single threshold but exhibits stochastic behavior. An overlap region exists in which both flame propagation and flame extinction can occur. This is primarily due to the uncertainties in the ignition parameter in the experiments, which were not accounted for in the one-dimensional simulations. The schlieren images from the experiments in [10] show that the geometry of the ignition kernel varies across different tests. This variation affects the ignition volume and, consequently, the ignition energy density. These observations underscore the importance of considering uncertainties in ignition volume when simulating ignition processes.

To simulate the stochastic behavior of the ignition process in simulations, a normal distribution is applied to the ignition radius, as is shown in Fig. 5.31 This uncertainty significantly influences the energy density in the ignition volume and the curvature of the flame front, thereby impacting the early flame propagation process. Simulations were conducted with both cylindrical and spherical geometries, as the geometry of the ignition channel plays a crucial role in the early flame propagation process, as discussed in Section 5.3.

For its importance in practical safety issues, $\mathrm{MIE}_{\mathrm{prop}}$ is investigated in this chapter. A "go"case corresponds to successful ignition with consequent self-sustained flame propagation, while a "no-go"case corresponds to ignition failure or flame extinction.

The Minimum Ignition Energy (MIE) is then determined using the regression method, which is a popular approach for determining MIE in experiments (see e.g.,[36, 105, 119, 128]). The regression method is explained in detail in Chapter 2.

An example of the determination of the MIE at 50% ignitability for a PRF/air mixture with RON = 50, $\phi = 1.0$, using spherical geometry with

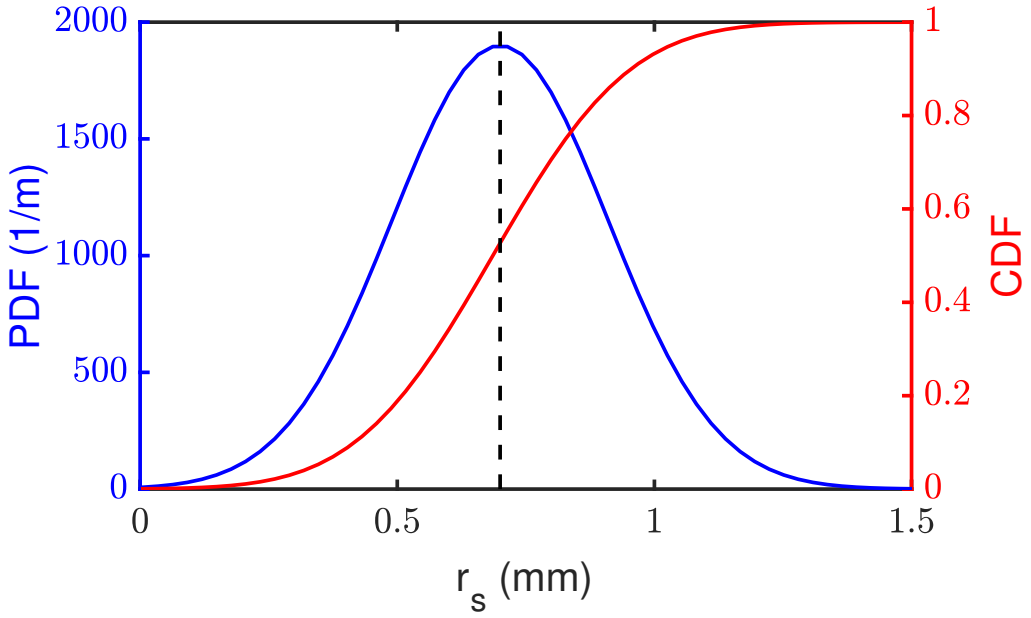

Figure 5.31: Normal distribution of the ignition radius.

$r_s = 0.7$ mm, at $p = 1$ bar and $T_0 = 373$ K is shown in Fig. 5.32. The overlapping region, where "go" and "no-go"cases coexist, from $E_{ig} = 0.75$ mJ to $E_{ig} = 0.95$ mJ is clearly seen. With the definition as the ignition energy at 50% probability of flame propagation, $\mathrm{MIE_{stoch}} = 0.93$ mJ. With a fixed ignition radius, the MIE for the PRF mixture with RON = 50 is $\mathrm{MIE_{fix}} = 0.80$ mJ, which means in this case, the uncertainty of the ignition radius causes an error in MIE of about 15%.

To explain the stochastic behavior of the ignition and early flame propagation process caused by the uncertainty of the ignition radius, the time evolution of maximum temperature and flame radius is shown in Fig. 5.33. Similar evolution of flame radius as a function of time is also observed in the experimental results of forced ignition for different fuels from Essmann et al [40]. The ignition energy, ignition radius, and ignition energy density for each case, along with the $\mathrm{MIE_{fix}}$ and minimal ignition energy density for the case with fixed $r_s = 0.7$ mm, are shown in Table 5.2.

For simulations of the ignition for PRF/air mixture with RON = 50, with spherical geometry and a fixed ignition radius $r_s = 0.7$ mm, the MIE is a threshold value $\mathrm{MIE_{fix}} = 0.80$ mJ, corresponding to $\mathrm{E_{ig}/V_s} = 0.56 \times 10^6$ J/m^3. For simulations with ignition radii, which are normally distributed, however,

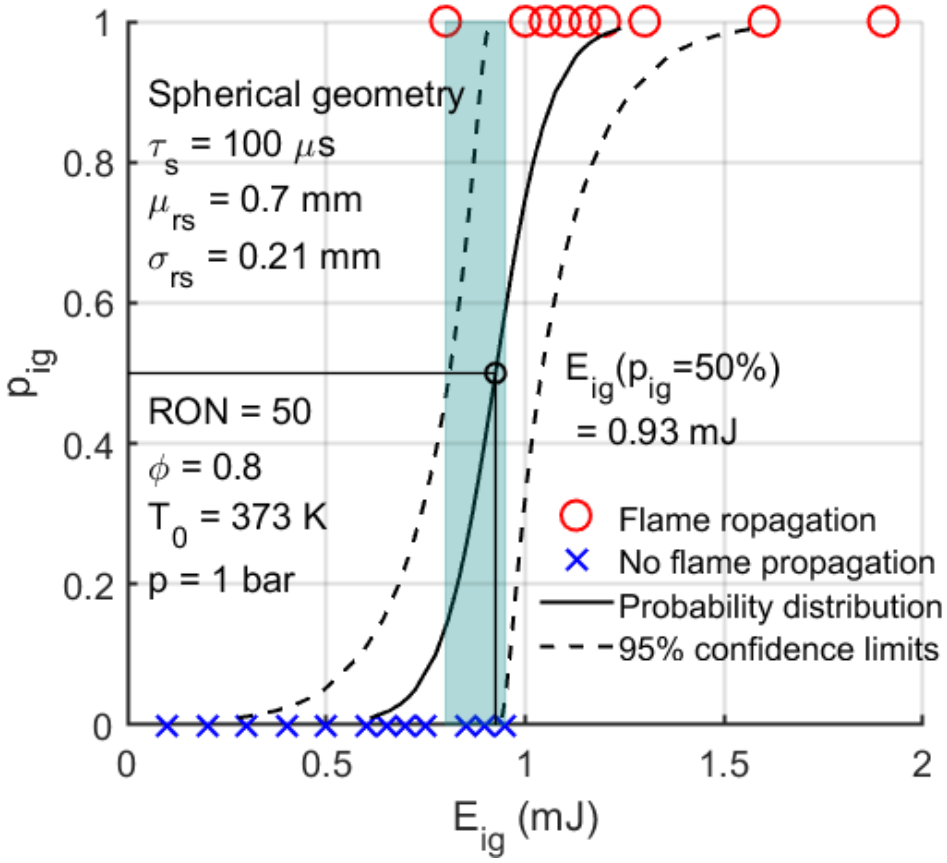

Figure 5.32: Determination of the MIE at 50% ignitability for PRF/air mixture with RON = 50, $\phi = 1.0$, using spherical geometry with $r_s = 0.7$ mm, at $p = 1$ bar and $T_0 = 373$ K.

Table 5.2: Ignition energy, ignition radius and ignition energy density for cases in Fig. 5.33.

Case	E_{ig} [mJ]	r_s [mm]	$E_{ig}/V_s \times 10^6$ [J/m^3]	Result
1	0.75	0.65	0.63	"go"
2	0.80	0.35	4.31	"no-go"
3	0.85	0.90	0.28	"no-go"
4	0.95	0.76	0.52	"no-go"
5	1.05	0.71	0.71	"go"
MIE_{fix}	0.80	0.70	0.56	

$E_{ig} > MIE_{stoch}$ is not the only criterion distinguishing "go"cases from "no-go"cases.

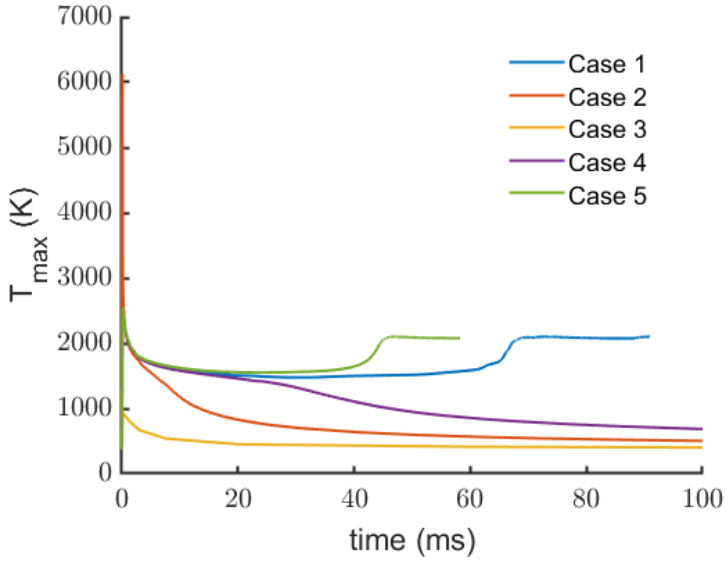

(a) Maximal temperature

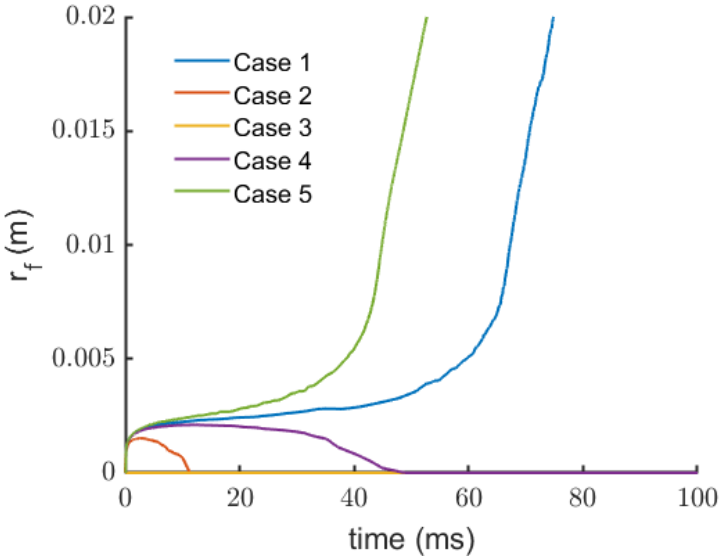

(b) Flame radius

Figure 5.33: Time evolution of maximum temperature and flame radius for PRF/air mixtures with RON $= 50$, $\phi = 1.0$, using spherical geometry with $r_s = 0.7$ mm, at $p = 1$ bar and $T_0 = 373$ K.

The uncertainty of r_s affects the ignition and early flame propagation process in two ways:

- **Ignition Energy Density**: The ignition energy density, $q_s \propto \frac{E_{ig}}{V_s} \propto \frac{E_{ig}}{r_s^i}$ (where $i = 3$ for spherical geometry and $i = 2$ for cylindrical geometry, $q_s \propto \frac{E_{ig}}{V_s}$ because the ignition energy density has a exponential form), implies that the ignition radius r_s directly influences the ignition energy density within the ignition volume. This, in turn, affects the temperature at the end of the ignition duration. This indicates that, when accounting for uncertainties in ignition radii, the ignition energy density, rather than just the ignition energy, must reach a critical value for a self-sustained flame to develop. Otherwise, the ignition may fail, or the flame kernel may form and then quench after a short period. For instance, in Case 3, a relatively large r_s results in $\frac{E_{ig}}{V_s} = 0.28\,\mathrm{J/m^3}$, which is only half the value for a fixed $r_s = 0.7\,\mathrm{mm}$. Consequently, even though $E_{ig} = 0.90\,\mathrm{mJ} > 0.80\,\mathrm{mJ} = \mathrm{MIE_{fix}}$, the mixture in the ignition volume heats up to only about 1000 K, below the minimum ignition temperature, leading to ignition failure. In Cases 1, 4, and 5, the ignition energy densities are similar, resulting in similar temperatures within the ignition volume. As discussed in Sec. 5.1, the PRF flame propagates slowly after ignition due to the comparable rates of heat release and heat loss (through conduction). The flame is thus highly sensitive to the temperature at the end of the ignition duration. While the flames in Cases 1 and 5, with ignition energy densities exceeding the minimum required value, reach the critical flame radius, the flame in Case 4 quenches.

- **Curvature Effect**: The ignition radius r_s also affects the curvature of the flame. A smaller r_s results in a smaller flame radius post-ignition, leading to a steep temperature gradient and significant heat loss through conduction. If the ignition radius is too small, even with ignition energy density larger than the critical value, the formed flame kernel quenches because of curvature effect. This explains the unexpected outcome in Case 2. Despite having an ignition energy density much higher than the minimum required value and achieving a mixture temperature of about 6000 K after the ignition duration, the flame kernel is too small to reach the critical radius due to the small r_s, causing the flame to quench.

With consideration of uncertainties of r_s, the MIE of stoichiometric PRF/air mixtures is calculated using both spherical geometry and cylindrical geometry.

For spherical geometry, the mean of the ignition radius is chosen to be $\mu_{r_s,\mathrm{sph}} = 0.7$ mm. For cylindrical geometry, the mean of the ignition radius is chosen to be $\mu_{r_s,\mathrm{cyl}} = 0.42$ mm. The purpose for the different mean ignition radii for the two geometries is to achieve comparable ignition volumes. This ensures that when comparing results between the two geometries, the effect of different ignition energy densities caused by varying ignition volumes can be eliminated, allowing focus on the differing curvature effects. Assuming the cylindrical ignition channel has a length of 2.5 mm, as suggested by Calcote et al. as the optimal gap between electrodes providing minimal value of Minimum Ignition Energy (MIE) for stoichiometric n-heptane/air mixtures at 1 bar [15], spherical and cylindrical ignition channels with mean ignition radii of $\mu_{r_s,\mathrm{sph}} = 0.7$ mm and $\mu_{r_s,\mathrm{cyl}} = 0.42$ mm, respectively, provide similar ignition volumes. The standard deviation for both cases is chosen to be $\sigma_{r_s} = 30\% \cdot \mu_{r_s}$. A relatively large standard deviation is chosen to investigate if the qualitative observations change with respect to the uncertainty of the ignition radius.

An interesting finding is that the results for n-octane have a wider overlapping region with a larger distance between the ignition energy at 5% and 95% ignitability, compared to iso-octane (for n-heptane, $E_{ig,95\%} - E_{ig,5\%} = 12.74$ mJ; for iso-octane, $E_{ig,95\%} - E_{ig,5\%} = 6.30$ mJ). This was also observed in the experiments of PRF ignition [128]. As explained in Sec. 5.4, the MIE of PRF/air mixtures first decreases with decreasing r_s, then, as diffusion becomes more significant, flame scenario II exists, the decreasing of MIE with decreasing r_s becomes slower. From a certain $r_{s,crit}$, MIE becomes constant. At about $r_s = 0.7$ mm, for the iso-octane/air mixture, the MIE stops decreasing with decreasing r_s; while for the n-heptane/air mixture, MIE still follows MIE $\propto r_s^3$ without the appearance of flame extinction. An error in r_s of 0.2 mm ($r_s = 0.5$ mm instead of $r_s = 0.7$ mm) results in an error in MIE of 3 mJ (about 50%) for n-heptane/air mixtures, and almost no error for iso-octane/air mixtures. This indicates that for experiments with a large ignition radius, special attention must be given to reducing the uncertainty of the ignition radius, as it causes significant error in the MIE. Conversely, for experiments with r_s near $r_{s,crit}$ for a given mixture under specific conditions, since the dependence of MIE on r_s becomes weaker, the uncertainty of r_s is less critical.

The figure (Fig. 5.35) illustrates the dependence of MIE on RON, considering fixed r_s and accounting for the uncertainty of r_s in both cylindrical and spherical geometries. It includes several experimental data points for MIE.

A significant observation from Fig. 5.35 is that, despite a relatively large uncertainty in r_s (30%), the qualitative trend of an upturn for simulations with

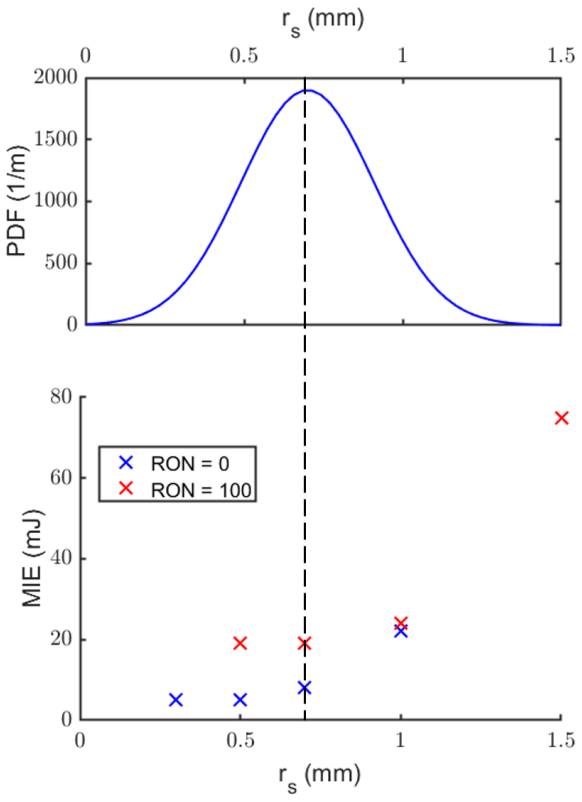

Figure 5.34: Dependence of MIE on r_s for iso-octane/air and n-heptane/air mixtures with $\phi = 1.0$, using spherical geometry, at $p = 1$ bar and $T_0 = 373$ K.

spherical geometry remains valid. Due to the smaller curvature in cylindrical geometry, flame extinction does not occur for all PRF/air mixtures, hence the observed upturn is absent.

Additionally, a noteworthy finding is the quantitative comparison with experimental results from Calcote et al. [15]. For the n-heptane/air mixture, the MIE observed in simulations closely matches that from Calcote et al.'s experiments. In contrast, for the iso-octane/air mixture, the experimental MIE from Calcote et al. falls between the values observed in simulations with spherical and cylindrical geometries.

Discrepancies in MIE values between simulations and experiments conducted by Metzler, and by Lewis and von Elbe are apparent. Several factors contribute to these discrepancies. Firstly, differences in the experimental apparatus can lead to variations in the parameter r_s of the ignition channel. In experiments, accurately estimating the ignition radius for simulations is

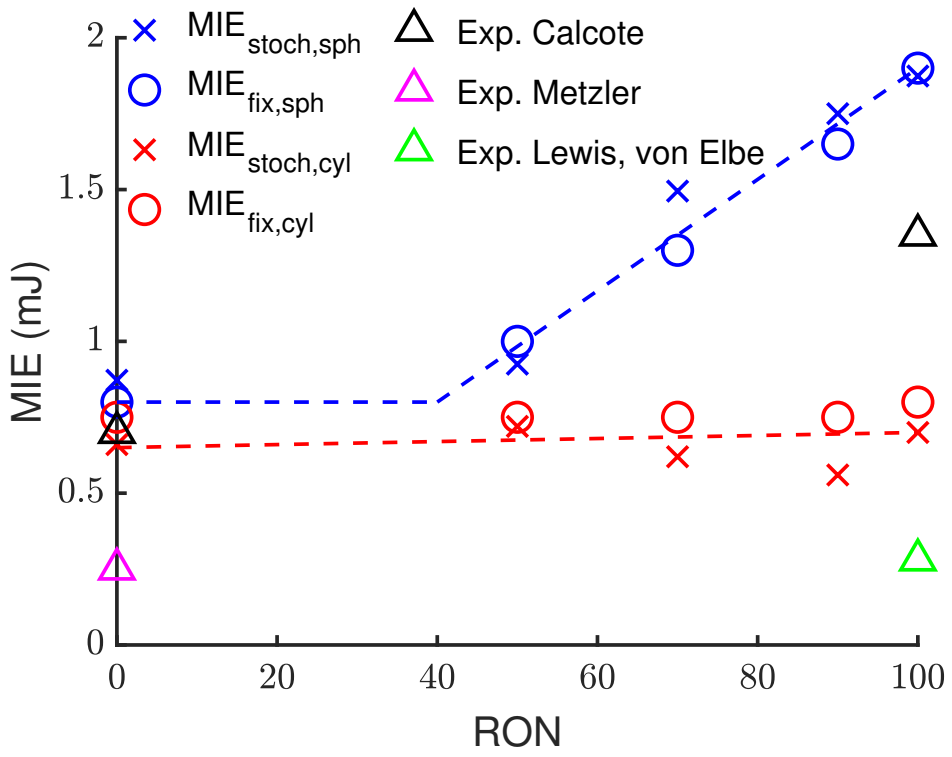

Figure 5.35: Dependence of MIE on RON with $\phi = 1.0$, using spherical geometry with $r_s = 0.7$ mm, at $p = 1$ bar and $T_0 = 373$ K. Lines are to guide the eyes. Experimental results: △: Calcote et al. [15];△: Metzler [87];△: Lewis, von Elbe [74].

challenging because the ignition kernel evolves during the ignition process. However, the MIE determined from simulations is highly sensitive to the ignition radius; even a small variation in the ignition radius can lead to a significant change in the ignition volume, which in turn affects the MIE.

Another significant factor is the methodology used to determine MIE in experiments. Moorhouse et al. [88] also found higher MIE values for various fuels in experiments compared to those reported by Lewis and von Elbe [74]. Moorhouse et al. attributed this difference to the criterion used by Lewis and von Elbe, who defined MIE as the energy level where flame propagation occurred in only 1 out of 100 experiments [88]. While direct evidence on the determination criteria of MIE in the experiments of Lewis and von Elbe is lacking in the literature, another study by Eckhoff et al., which assessed MIE at 50% ignitability for a propane/air mixture, also reported values 2-3 times larger than those reported by Lewis and von Elbe [36]. This also

indicates that the experiments of Lewis and von Elbe [74] may have employed a criterion for determining MIE that was overly conservative.

These observations underscore the variability in experimental apparatus and criteria used to determine MIE, which can result in significant discrepancies when comparing experimental results with each other and with simulation data. However, the qualitative agreement between experiments and simulations, with or without accounting for the uncertainty of r_s , highlights that the one-dimensional simulations accurately predict the underlying physics and the interaction between chemical heat release and transport processes during flame initiation and early propagation.

5.8 Dependence of MIE on Strain Rate

So far, the induced ignition characteristics of quiescent PRF/air mixtures have been investigated. Many practical combustion devices operate in turbulent flow [109], where the flame front is significantly strained and wrinkled by the turbulence. In such turbulent conditions, the ignition process is affected by strong diffusion, which increases the thickness of the flame front and reduces the energy available to heat the fresh mixture and initiate the flame [32]. Consequently, the minimum ignition energy (MIE) required for forced ignition in turbulent flow is higher than that in a quiescent mixture [60, 105]. Shy and co-workers found that there exists a MIE transition for turbulent spark ignition. Specifically, the MIE initially increases slowly with turbulence intensity. However, after reaching a certain threshold of turbulence intensity, the MIE increases rapidly with further increases in turbulence intensity [53, 60, 105]. A similar transition was also observed in experiments with laser-induced spark ignition [20] and numerical investigations using direct numerical simulation (DNS) [114]. Additionally, the time- and space-dependent turbulent fluctuations of the strain rate cause larger uncertainties during the forced ignition process, resulting in more significant stochastic behavior and a wider range between 50% ignitability and 100% ignitability compared to forced ignition in quiescent mixtures [53, 83, 105, 128].

Since the strain rate of the flow is one of the most important factors influencing forced ignition in turbulent flames, investigating the dependence of MIE on strain rate could provide useful insights into the underlying physics of turbulent ignition processes. To this end, Yu and co-workers have studied the spark ignition processes of laminar strained premixed flames of NH_3/H_2[139] and CH_4[138]. In this work, laminar strained premixed lean

PRF/air flames with a counterflow configuration are investigated, focusing on the dependence of MIE on strain rate.

To compare the simulation results (MIE against strain rate) with the experimental results (MIE against turbulence intensity), a relationship between the strain rate of the flame front and the turbulence intensity must be established. In this work, the turbulence intensity is converted to the strain rate using the expression in the work of Meneveau and Poissot [85]. Here, the rate of growth of the active flame surface $\langle\kappa\rangle$ is expressed as a function of turbulence intensity and $\frac{L}{l_F}$, which is the ratio of the integral length scale and the laminar flame thickness [85]:

$$\langle\kappa\rangle = \sqrt{\frac{\langle\epsilon\rangle}{\nu}}\mathrm{Re}^{-1/2}\frac{c_{ms}}{ln2} \times \int_0^{p_{max}} C\left(e^{-p}\frac{L}{l_F}\right)e^{p(2/3-\mu/9)}dp \tag{5.4}$$

Here, Re is the Reynolds number, which is directly correlated to turbulence intensity: $\mathrm{Re} = u' \cdot L/\mu$, where u' is the turbulence intensity, L is the integral length scale, and μ is the kinematic viscosity. $\langle\epsilon\rangle$ is the turbulent dissipation rate and $c_{ms} = 0.28$ is a constant calculated by Yeung et al. [137]. $p = ln(L/r)$ is an integration variable with r the votex size. The turbulence intensity u' and the integral length scale L vary across different experiments.

In the experiments conducted by Jiang et al., turbulence is generated using two counter-rotating vortical fans. The resulting turbulence intensity, u' , has a linear correlation with the frequency of the fans, f (with unit of ms^{-1}) [60]:

$$u' = 0.0462f \tag{5.5}$$

The integral length scale is also determined in terms of the fan frequency [60]:

$$L = 10.7f^{0.34} \tag{5.6}$$

Fig. 5.36 shows the dependence of the MIE on strain rate for a lean isooctane/air mixture with an equivalence ratio $\phi = 0.8$. In this context, the MIE is normalized with respect to the MIE of ignition in a quiescent mixture with one-dimensional planar geometry $\Gamma = \mathrm{MIE(a)}/\mathrm{MIE}_0$, with $\mathrm{MIE}_0 = 510\,\mathrm{J/m^2}$.

The most important conclusion from Fig. 5.36 is that the simulation accurately predicted the MIE transition at $a = 60\,\mathrm{s}^{-1}$, corresponding to an RMS turbulent fluctuation $u' = 1.73\,\mathrm{m/s}$. The simulation results exhibit only about a 5% difference compared to the experimental data. The simulations were repeated for PRF with RON = 95, a MIE transition also exists at $a = 80\,\mathrm{s}^{-1}$, corresponding to an RMS turbulent fluctuation $u' = 2.36\,\mathrm{m/s}$, with about a 3% difference compared to the experimental data of Shy et al. ($u' = 2.3\,\mathrm{m/s}$) [106]. This close agreement between simulations and experiments

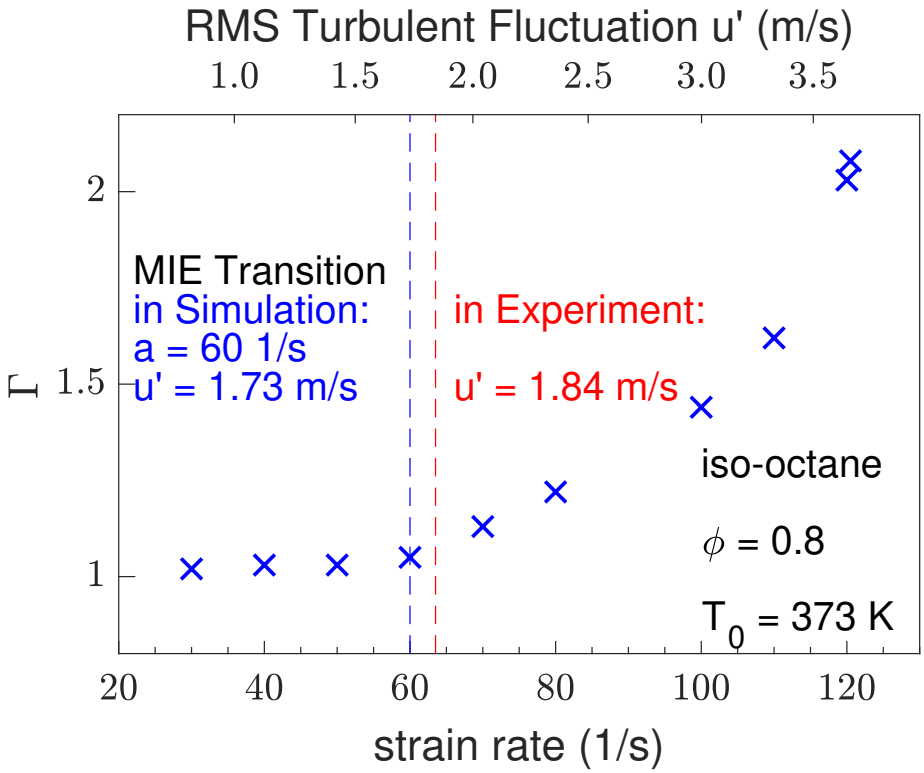

Figure 5.36: Dependence of MIE on strain rate for lean iso-octane/air mixtures with $\phi = 0.8$, $T_0 = 373$ K and $p = 1$ bar. Transition in experiments from Jiang et al. [60]

indicates that simulations using a laminar counterflow configuration can effectively describe the effects of turbulence with qualitative precision.

To explain the existance of the MIE transition, the temporal evolution of maximum temperature for an iso-octane/air mixture with $a = 110\,\mathrm{s}^{-1}$ at different ignition energies is shown in Fig. 5.37. Here, even for cases with $E_{ig} <$ MIE ($E_{ig} = 7.65$ mJ and $E_{ig} = 7.90$ mJ, represented by dotted lines), flame initiation can still be observed. However, the presence of flow velocity and flame strain leads to significant negative values of heat conduction and heat convection. If the net sum of chemical heat release and heat loss is negative, the flame temperature decreases, potentially leading to flame extinction. As ignition energy increases, the temperature at the end of the ignition duration also rises, resulting in a higher positive chemical heat release rate in the reaction zone. When the ignition energy reaches the minimum ignition energy, the net sum of the chemical heat release rate and the thermal diffusion rate remains positive, allowing the flame to stabilize at a location

where the flame speed matches the normal flow velocity. The larger the strain rate, the more energy is needed for the flame to sustain. At small strain rate, however, with weaker thermal diffusion and stronger chemical heat release [139], the formed flame kernel always has a net positive sum of heat release and heat loss. Consequently, flame extinction is not observed, a successful initiated flame can finally become a stable flame. For this reason, an MIE transition exists at the strain rate where flame extinction begins to occur. This result has a good agreement with the DNS results for turbulent ignition of methane/air mixtures from Turquand d'Auazy et al. [114].

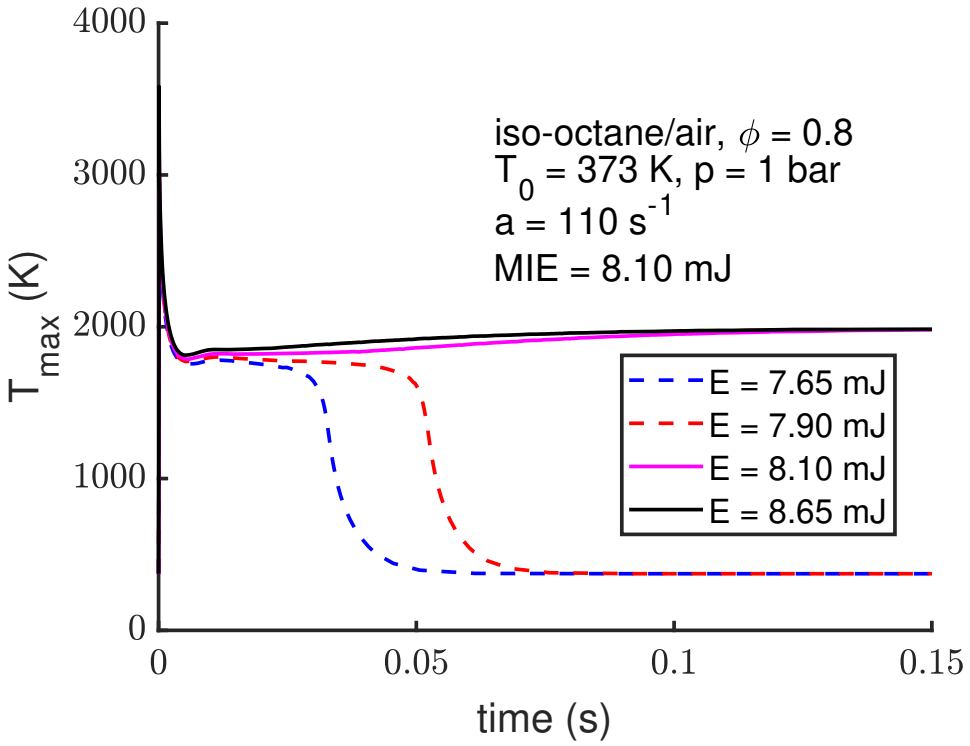

Figure 5.37: Temporal evolution of maximum temperature for iso-octane/air mixtures with $\phi = 0.8$, at $a = 110\,\mathrm{s}^{-1}$, $T_0 = 373$ K and $p = 1$ bar.

Quantitative discrepancies with the experiments of Jiang et al. [60] can be observed. The increase in MIE before and after the MIE transition in the experiments is steeper than in the simulations. Specifically, the MIE at $a = 60\,\mathrm{s}^{-1}$ in simulations is only 6% larger than the MIE for a quiescent mixture. In contrast, the MIE in experiments at the MIE transition is already four times larger than the MIE for a quiescent mixture.

This discrepancy can be explained as follows: in simulations, the MIE transition for a lean iso-octane/air mixture already takes place at a low strain rate of $a = 60\,\mathrm{s}^{-1}$, which corresponds to a low flow velocity $v = 1.2\,\mathrm{m/s}$. With a short ignition duration $\tau_s = 100\,\mu\mathrm{s}$, the resulting length scale of 0.12 mm is an order of magnitude smaller than the ignition radius of 1.0 mm. The influence of the mass flow on the MIE is small.

In fact, a similar tendency, where MIE is almost constant until the MIE transition, was also observed in the DNS results for methane from Turquand d'Auazy et al.[114] and in the experimental results for methane from Cardin et al.[20]. Turquand d'Auazy et al. argued that this discrepancy might be caused by the spark ignition energy measurement, suggesting that the results from Cardin et al., which use laser ignition, have a better quantitative agreement with the simulations [114].

Another possible reason, according to Turquand d'Auazy et al., is the stochastic behavior during ignition in a turbulent flow [114]. To check the influence of the stochastic behavior during ignition in a turbulent flow on the MIE, simulations were repeated with consideration of the uncertainty of the strain rate. A normal distribution with the standard deviation of a equal to 30% of the mean of a was applied to the strain rate. The MIE was then calculated at 50% ignitability using regression method.

As shown in Fig.5.38, with a normally distributed strain rate, the MIE increases slightly faster with increasing strain rate compared to the results with a fixed strain rate. However, the increase of $\Gamma = \mathrm{MIE}/\mathrm{MIE}_{\mathrm{laminar}}$ with normally distributed strain rate is still much slower compared to the experimental results from Jiang et al.[60]. Despite the spark ignition energy measurement issue mentioned by Turquand d'Auazy et al. [114], another possible reason for this quantitative discrepancy could be that, even with a normally distributed strain rate, the strain rate in a single simulation remains constant, whereas in experiments, the strain rate exhibits stochastic behavior over time and space. Local extinction may occur in experiments, necessitating a larger MIE for successful flame propagation. Additionally, the flame front in experiments is not only strained but also curved, which intensifies diffusion due to the curvature effect. This phenomenon might also contribute to the requirement of a larger MIE for successful flame propagation.

The existence of the MIE transition in simulations of a laminar strained counterflow flame and in experiments of forced ignition in a turbulent flow highlights that the underlying physics and the interaction between chemical kinetics and transport can be qualitatively predicted using a laminar strained flame configuration. This holds true, at least in the flamelet regime of turbulent flames.

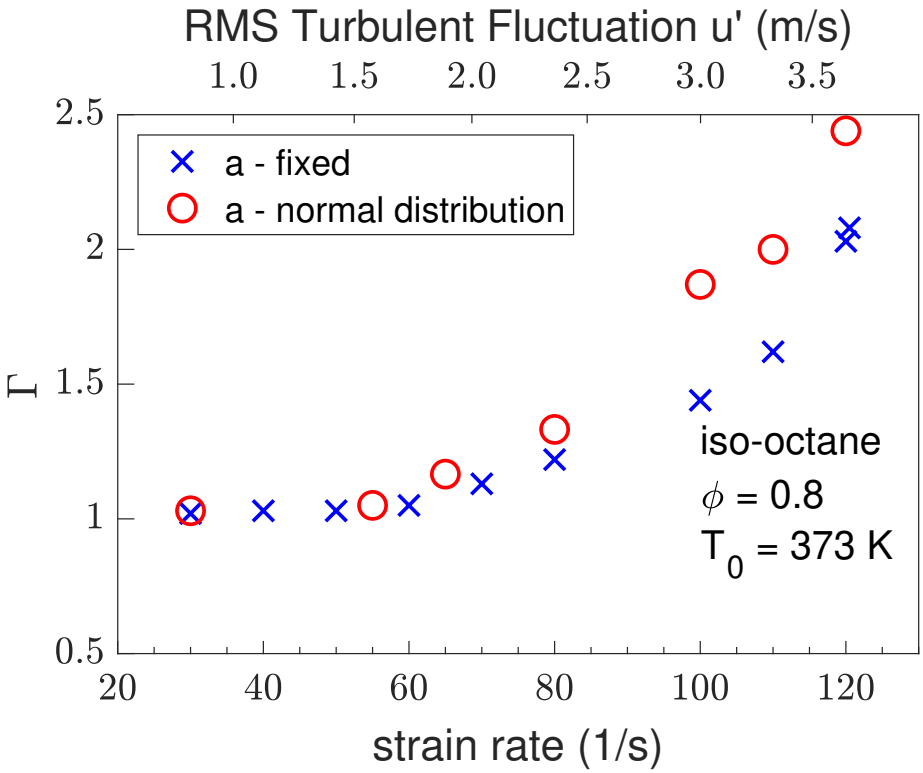

Figure 5.38: Dependence of MIE on strain rate for lean iso-octane/air mixtures with $\phi = 0.8$, $T_0 = 373$ K and $p = 1$ bar, with fixed strain rate, and with normally distributed strain rate.

In conclusion, this chapter investigates the induced ignition of PRF/air mixtures. The results highlight the influence of chemical kinetics (such as the different reaction pathways of straight-chain and branched-chain alkanes and the low-temperature chemistry of large hydrocarbon fuels) and transport processes (such as the curvature effect) on the ignition and early flame propagation of PRF flames. Phenomena observed in the experiments are accurately captured by simulations, with quantitative differences in MIE between the experiments and simulations, primarily due to the challenging estimation of the ignition radius. The stochastic behavior of the ignition process is also numerically investigated, taking into account the uncertainties of the ignition parameters. Although quantitative discrepancies in MIE are caused by the stochastic research, they do not qualitatively affect the ignition process of PRF.

6 Induced ignition of Ammonia

Utilizing carbon-free fuels like ammonia contributes to mitigating climate change. Therefore, studying and optimizing ammonia combustion is crucial for achieving a net-zero carbon emission society and facilitating the transition to sustainable energy technology [1].

However, due to its low chemical reactivity, ammonia exhibits a small laminar flame speed [37, 49, 65, 99], narrow flammability limits [66], and requires a large MIE for flame initiation [34]. To enhance the flame and ignition characteristics of ammonia, additives such as methane and hydrogen are often considered. With its high reactivity and absence of CO_2 emissions, hydrogen is one of the most attractive additives for enhancing ammonia flames.

In the past, numerous experimental and numerical studies have been carried out to investigate the auto-ignition and flame propagation behaviors of ammonia flames, including IDT [14, 96], flammability limits [22, 26], laminar flame speed [49, 56, 95]. The influence of hydrogen addition to ammonia flames on IDT and laminar flame speed has also been intensively investigated. Numerical and experimental studies confirm that the high chemical reactivity and high diffusivity of hydrogen enhances the combustion of ammonia, resulting in increased laminar flame speed and decreased ignition delay time [23, 75, 120].

The chemical kinetics of ammonia have been intensively investigated over the last decades, and numerous mechanisms have been developed. However, most published mechanisms for ammonia can only accurately predict the characteristics of ammonia flames under specific conditions. A comprehensive understanding of the critical reactions in ammonia combustion is still in progress [4]. While most validation efforts for ammonia mechanisms focus on IDT and laminar flame speed, simulations of the transition from induced ignition to self-sustained flame propagation (or the lack thereof) can also provide valuable information for improving the modeling of ammonia and validating the mechanisms. In this work, a popular ammonia mechanism developed by Shrestha et al.[104] is used, which includes 34 species and 278 reactions and provides a good prediction of the ignition delay time (IDT)[63]. Another mechanism developed by Otomo et al. [91] is used to investigate the

influence of different mechanisms on the simulation of induced ignition in ammonia/air mixtures.

In this chapter, the results of numerical studies on the induced ignition of ammonia are provided and discussed. This includes the influence of considering radiation in the numerical model on the simulation results, the dependence of the MIE on the equivalence ratio, and the impact of hydrogen addition on the induced ignition of ammonia. The simulation results are validated against experimental results.

6.1 Flame Scenarios

Similar to the chapters on methane and PRF, the initial task in investigating the induced ignition of ammonia/air mixtures is to explore the possible outcomes after ignition. Because of the slow chemistry of ammonia, flame extinction might also occur during the induced ignition process. The flame scenarios of ammonia flames are similar to those of hydrocarbon flames at atmospharic conditions, whose temperature profiles can be found in Chapter 5:

Type I **Ignition failure**: The ignition energy is insufficient for the formation of a flame kernel, resulting in a decrease in temperature within the ignition volume after the ignition duration.

Type II **Successful ignition followed by flame extinction**: The ignition energy is sufficient to form a flame kernel, causing the temperature within the ignition volume to initially increase after the ignition duration. However, due to the slow chemistry of ammonia, the flame eventually quenches, and the temperature at the center returns to the initial value.

Type III **Successful ignition and self-sustained flame propagation**: The ignition energy is sufficient to form a self-sustained flame, maintaining a high temperature at the center.

6.2 Effect of Thermal Radiation

For the experiments on laminar ammonia flames, the slow laminar flame speed results in a longer residence time of the flame in the combustion chamber compared to hydrocarbon fuels [41]. During the flame propagation of an ammonia flame in the combustion chamber, the ammonia flame is very

sensitive to heat loss through radiation due to its slow chemical heat release. Many studies have investigated the effect of thermal radiation on laminar ammonia flame propagation. The conclusion is that thermal radiation is crucial for an accurate prediction of the laminar flame speed of ammonia flames. Radiation has a greater impact on the flame speed of pure ammonia flames compared to methane flames or ammonia/hydrogen mixtures [41, 90].

Meanwhile, the influence of thermal radiation on the induced ignition process, i.e., the transition from a flame kernel to a self-sustained flame (or to flame extinction), remains less explored. In this work, the simple optically thin approximation model (OTM) is considered. Although reabsorption is not included in the OTM, the underlying physics can already be indicated by comparing simulations with adiabatic and radiative models.

Here, the volumetric radiative heat loss $\dot{q}_{rad}$ is given as:

$$\dot{q}_{rad} = 4 \cdot k \cdot \sigma \cdot (T^4 - T_b^4) \tag{6.1}$$

with σ the Stefan-Boltzmann constant ($\sigma = 5.669 \times 10^{-8}\,\mathrm{W/(m^2 \cdot K^4)}$). T_b is the environmental temperature, which is set to be the temperature of the unburnt gas mixture. k is the total Planck mean absorption coefficient, which is determined by considering the contribution of radiation species i as

$$k = \sum p_i a_{p,i} \tag{6.2}$$

where p_i is the partial pressure and $a_{p,i}$ is the Planck mean absorption coefficient of radiation species i, which describes the total emission from a medium [142]. The radiating species considered in this work are H_2O, NO, N_2O, and NH_3, which are the important radiation species according to [41, 90] The Planck mean absorption coefficient of the radiating species can be found in [90].

The influence of radiative heat loss on the early flame propagation process can be observed in Fig. 6.1. Note that the displayed time and spatial coordinates are different in Fig. 6.1(a) and Fig. 6.1(b) because the effect of radiative heat loss takes a long time. For the case with the adiabatic model, the temperature in the center remains constant once the flame becomes self-sustained. However, for the case with the radiative model, the temperature in the center keeps decreasing while the flame propagates away from the center. The reason is that the burnt mixture in the center doesn't participate in the chemical reactions. In the simulation with the adiabatic model, there is no heat loss at the center, so the temperature of the burnt mixture remains constant. In the simulations with the radiative model, however, radiative heat loss causes a temperature decrease at the center.

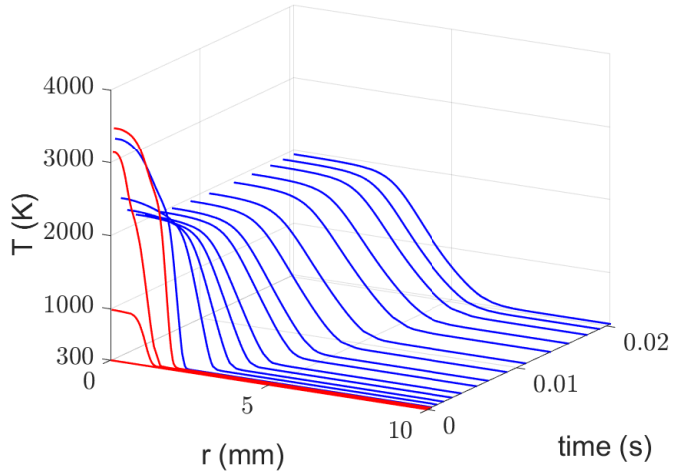

(a) Adiabatic

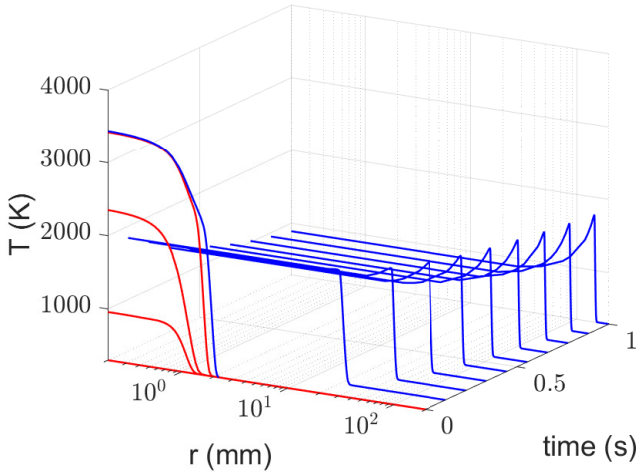

(b) Radiative

Figure 6.1: The spatio-temporal profile of temperature for the case with successful ignition for stoichiometric ammonia/air mixture at 1 bar and 300 K in simulations. Red lines represent temperature within the spark duration, black lines represent temperatures after the spark duration [130]

Fig. 6.2 shows the flame structure of a spherical ammonia/air flame under atmospheric conditions. It can be observed that for the flame with radiation, the flame temperature is lower and the flame thickness is larger compared to the adiabatic flame. The mass fraction of OH for the flame with radiation is smaller than that in adiabatic flame. This indicates that in the flame with radiation, with its lower temperature, more reactive species like OH are needed for the formation of H_2O. In contrast, in the adiabatic flame, H_2O can be formed through reactions with less reactive species like O. The consumption of OH for the formation of H_2O leads to a reduction of reactive species and a further decrease in the flame temperature of the flame with radiation. The formation of H_2O at the expense of OH species in the flame with radiation of ammonia is also observed in [90].

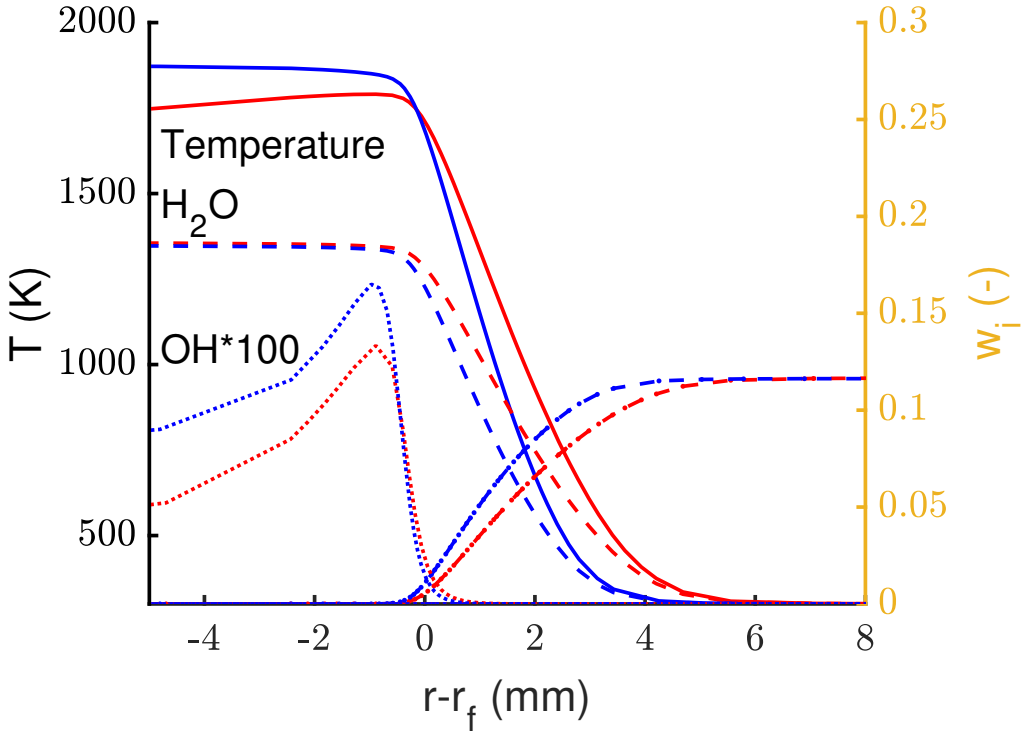

Figure 6.2: The flame structure of lean spherical ammonia/air flame ($\phi = 0.8$) at atmospheric conditions with radiation (red) and without radiation (blue) using flame centered coordinates

In the next section, the effect of radiative heat loss on the minimum ignition energy (MIE) and flammability limits of ammonia/air mixtures under atmospheric conditions will be discussed.

6.3 Dependence of MIE on Equivalence Ratio

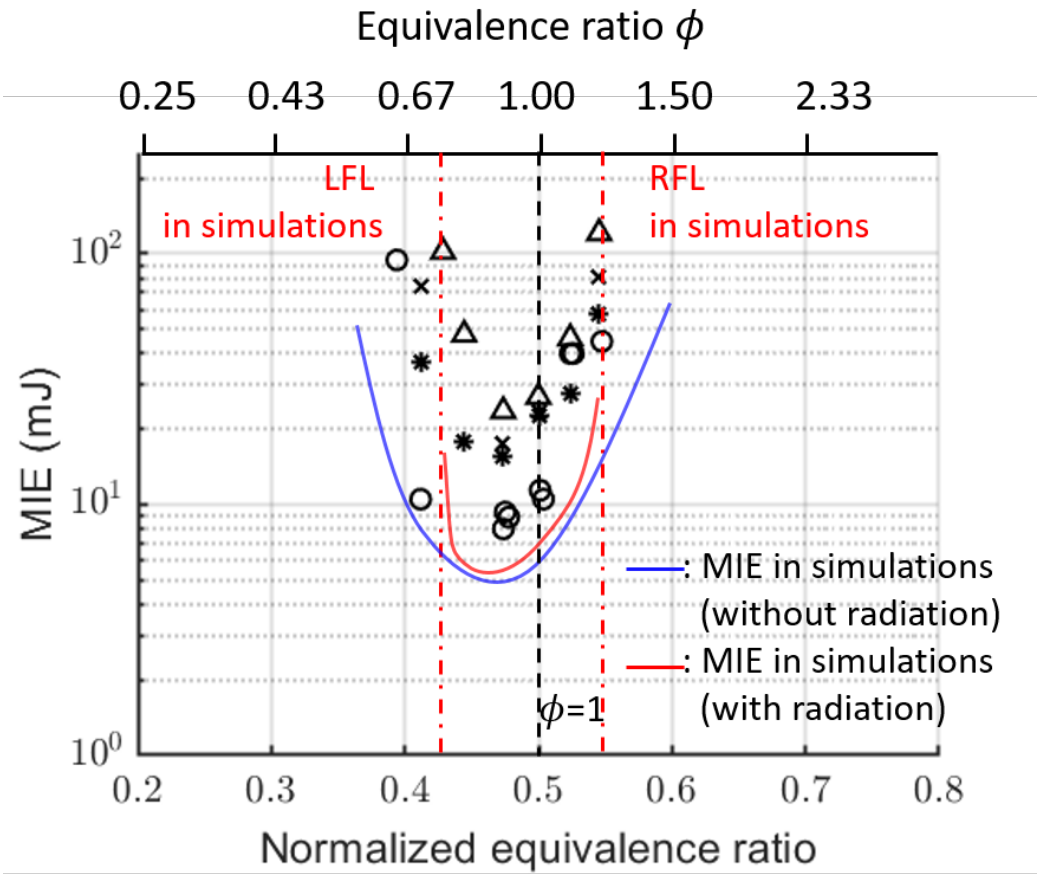

$$\phi_n = \frac{\phi}{1+\phi}$$

Figure 6.3: The dependence of MIE on equivalence ratio at 1 bar and $T_0 = 300\,\mathrm{K}$ for ammonia/air mixture with spherical geometry [130]. Comparison with experimental results for pure ammonia are represented by ○: Verkamp et al. [118]; ∗: Lesmana [73]; x: Sadaghiani et al. [101]

Since the mixture composition strongly affects the induced ignition process, the dependence of MIE on the equivalence ratio is crucial. The dependence of MIE on ϕ for ammonia/air mixtures is shown in Fig. 6.3 with comparison to experimental results at atmospheric condition.

Similar to the results of the hydrocarbon fuels, which are described in the previous chapters, the MIE of ammonia/air mixture also has a U-shape form. However, the calculated MIE of ammonia/air mixtures is much larger

than that of methane/air and PRF/air mixtures under the same conditions. For example, with $T_0 = 300\,\mathrm{K}$, $p = 1\,\mathrm{bar}$, and $r_s = 1\,\mathrm{mm}$, the MIE of a stoichiometric ammonia/air mixture is about 7 mJ, while for stoichiometric methane/air or iso-octane/air mixtures, MIE $\approx 3\,\mathrm{mJ}$. This is mainly due to the slow chemical reaction of ammonia. For stoichiometric ammonia/air mixtures, while a flame kernel can be observed at an ignition energy of 3.5 mJ, the flame always quenches until MIE $\approx 7\,\mathrm{mJ}$ because the HRR from chemical reactions is lower than the heat losses, such as heat conduction. At MIE $\approx 7\,\mathrm{mJ}$, the high temperature after energy deposition (about 3500 K) ensures self-sustained flame propagation.

In both experiments and simulations, the lowest Minimum Ignition Energy (MIE) is observed on the lean side, around $\phi = 0.9$ [130]. One possible reason is that the specific heat capacity of lean mixtures is higher than that of rich mixtures (as shown in Fig. 6.4).

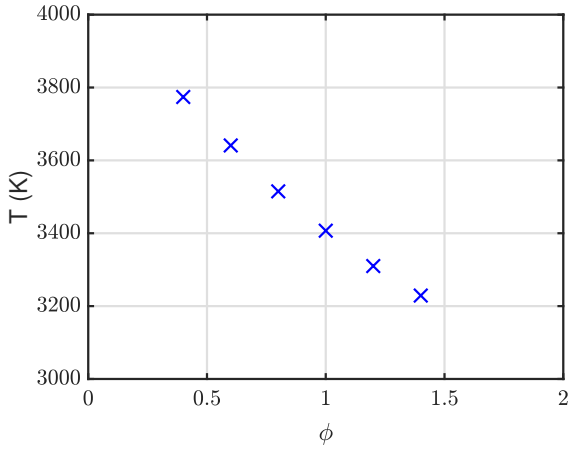

Figure 6.4: Temperature at the center of the ignition volume at the end of ignition duration in dependence of equivalence ratio for ammonia/air mixture under atmospheric conditions

Another important observation in Fig. 6.3 is that the MIE value in experiments is higher than in simulations [130]. Similar to the induced ignition of PRF, this discrepancy may also be attributed to the difficulty in accurately estimating the ignition radius, which can significantly affect the MIE. Furthermore, the geometry of the flame kernel in experiments is not ideally spherically symmetric but instead has a shape that cannot be described using one-dimensional geometry. Another possible reason for the discrepancy between MIE values in experiments and simulations is that some heat losses in experiments (such as heat conduction to the cold electrodes, buoyancy,

etc.) are not included in the one-dimensional simulation. Due to the small flame speed, the residence time of the ammonia flame in the combustion vessel during experiments is longer compared to hydrocarbon fuels, giving the heat losses more time to affect and even quench the flame. The heat losses in experiments cause a larger MIE than in simulations [130]. Another important reason for the discrepancy between MIE values in experiments and simulations is related to the experimental techniques. Some experiments use high speed cameras and define successful ignition when a flame is visible, while other experiments use the pressure increase as the criterion for successful ignition. However, some weak ammonia flames might not be clearly visible. Additionally, the pressure increase in the experiments might not have a clear threshold between flame propagation and ignition failure. The significant influence of experimental techniques on the MIE measured for ammonia/air mixtures is also indicated by the fact that MIE values measured in different experiments can vary significantly, sometimes by a factor of 3-4.

The influence of radiative heat loss on the Minimum Ignition Energy (MIE) for ammonia/air mixtures is evident in the provided figures. Specifically, Fig. 6.3 illustrates how the MIE changes with and without considering radiative effects. Near stoichiometric conditions, the difference in MIE between the two scenarios is minor, but as the mixture becomes leaner or richer (moving away from stoichiometry), the MIE with radiation considered increases significantly compared to without radiation. This suggests that radiative heat loss has a more pronounced impact on mixtures near the flammability limits [130]. This is because, near the flammability limits, the slow chemical reactions make the early flame highly sensitive to any heat losses, including radiative heat loss.

The flammable range calculated with the adiabatic flame model is LFL = 0.6 and RFL = 1.5, which is larger than the flammable range measured in all experiments. However, when considering radiation, the flammable range in simulations, LFL = 0.78 and RFL = 1.2, shows better agreement with the experiments. This again confirms the importance of accounting for radiation in the simulation of ammonia/air flames [130].

To investigate the influence of different chemical kinetics chosen for the simulations on the MIE for ammonia/air mixtures, simulations are repeated with another mechanism developed by Otomo et al.[91]. Results confirm the importance of accounting for radiation effects in the simulations. Calculations with both mechanisms considering radiation effects deliver comparable flammability limits with the experiments, while with adiabatic flames, the flammable range calculated with both mechanisms is larger than in the experiments. Although the MIE calculated with both mechanisms shows

discrepancies on the rich side, the underlying physics that the ammonia flame near the flammability limits is more sensitive to radiation effects than the flame around stoichiometry is correctly predicted with both mechanisms [130].

6.4 Effect of Hydrogen Addition

As described in the last section, the MIE of pure ammonia is much larger than that of hydrocarbon fuels, indicating that pure ammonia is hard to ignite due to its slow chemical kinetics. To enhance the ignition and early flame propagation process of ammonia, hydrogen is considered as an additive.

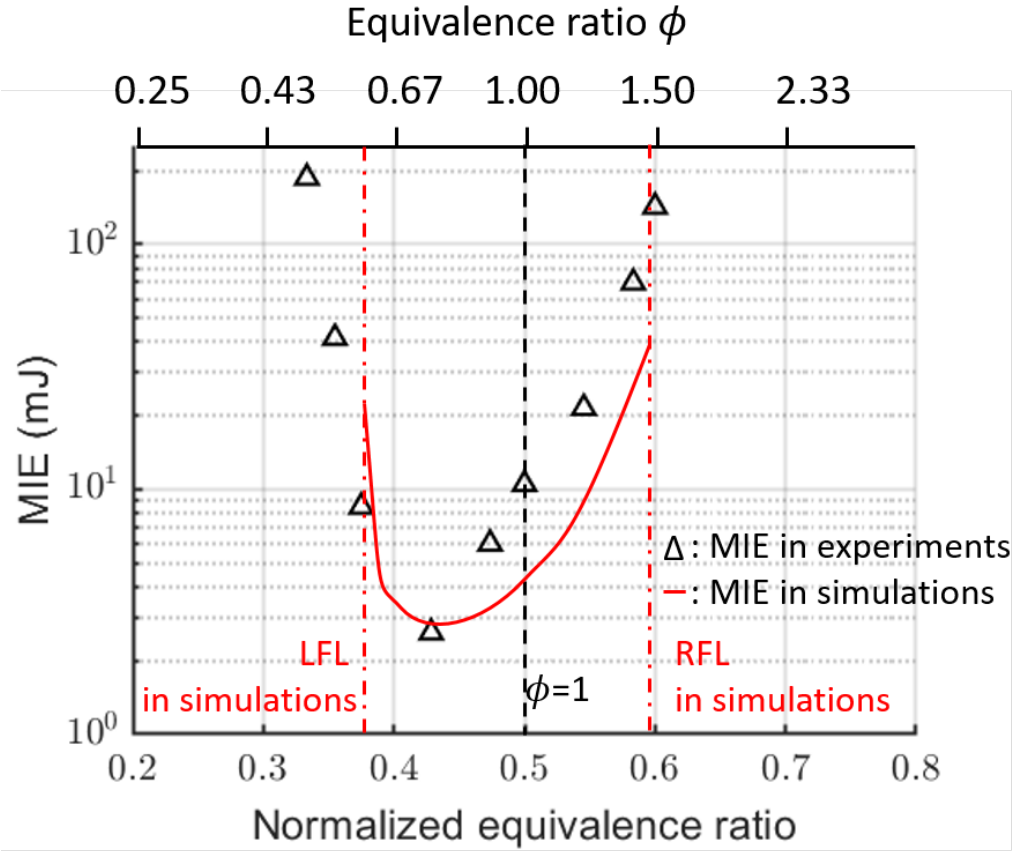

Figure 6.5: The dependence of MIE on equivalence ratio at 1 bar and $T_0 = 300\,\mathrm{K}$ for 90 % NH_3/ 10 % H_2/air mixture with spherical geometry [130].

Fig. 6.5 shows the dependence of MIE on ϕ for 90 % NH_3/ 10 % H_2/air mixture with spherical geometry.

Similar to ammonia/air mixtures, the radiative heat loss also has a significant effect on mixtures near the flammability limits, resulting in a narrower and more experimentally comparable flammable range for the radiative simulations compared to the adiabatic simulations [130].

The influence of hydrogen addition is clearly observed in both experiments and simulations. With only 10% hydrogen, the MIE of the stoichiometric mixture decreases from 27 mJ to 10.5 mJ in experiments, and from 7 mJ to 2.5 mJ in simulations. At the same time, the flammable range with hydrogen addition is significantly larger than that of pure ammonia, both in simulations and experiments [130]. This demonstrates the enhancement of the chemical reactivity of the ammonia flame with hydrogen addition, a finding also observed in the work of Fernández-Tarrazo et al. [44] using simulations.

A rather surprising finding is that, although the MIE for pure ammonia in simulations is much smaller than in experiments throughout the flammable range, the MIE for a 10% H_2/90% NH_3 mixture in simulations and experiments is comparable on the lean side [130]. A possible explanation is that, with the enhancement of chemical reactivity due to hydrogen addition, the critical time for a 10% H_2/90% NH_3 flame is much shorter than that for pure ammonia. This means that for a 10% H_2/90% NH_3 flame, the heat losses in experiments (such as heat conduction to the electrodes, buoyancy, etc.) which are not included in the simulations, have less time to influence and quench the flame. Hence, the MIE in simulations and experiments is more comparable than that of pure ammonia [130]. As shown in Fig. 6.6, the flame of the 10% H_2/90% NH_3 mixture almost propagates at a fast speed from the beginning, whereas for pure ammonia flame, it takes about 0.02 s before the flame propagates at a fast speed. Additionally, the strong chemical reactivity of the 10% H_2/90% NH_3 flame makes detecting flame propagation with a high-speed camera easier than with an ammonia flame, where the chemical reactions might be weak, resulting in a weak and not clearly visible flame.

This chapter investigates the induced ignition of ammonia and ammonia/hydrogen blends. The results underscore the importance of incorporating radiation into the numerical model: when radiation is considered, the flammable range in simulations becomes comparable to that observed in experiments. Another key conclusion is that adding hydrogen significantly enhances ignition and early flame propagation of ammonia while reducing the MIE. However, accurately estimating the MIE in simulations for ammonia

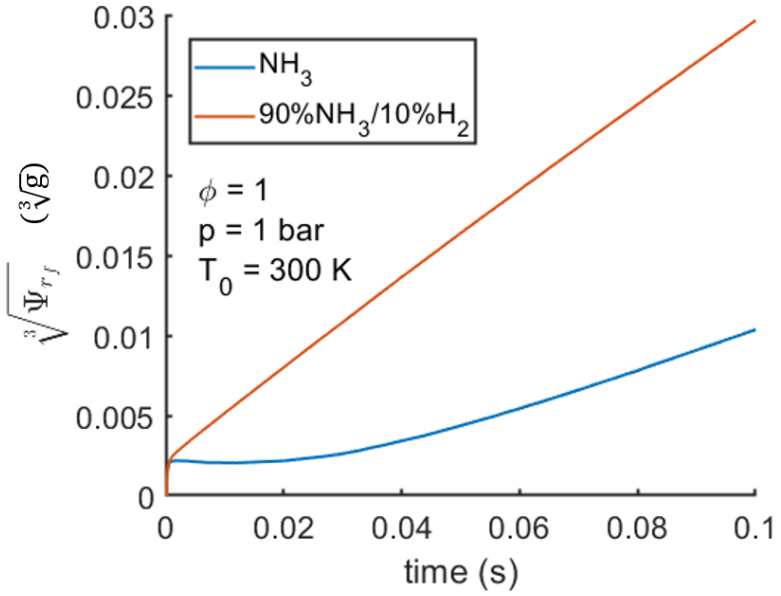

Figure 6.6: Temporal evolution of $\Psi_{(r_f)}$ for NH_3 flame and $90\%NH_3/10\%H_2$ flame at $\phi = 1$ [130].

remains challenging, primarily due to difficulties in precisely determining the ignition radius.

7 Conclusion and Outline

This dissertation aimed to simulate the forced ignition and early flame propagation of hydrocarbon fuels (methane and PRF) and non-carbon fuels (mixtures of ammonia and hydrogen) using one-dimensional geometries, detailed chemical kinetics, and transport models. The study focused on Minimum Ignition Energy (MIE) due to its critical role in enhancing combustion efficiency and ensuring safety by preventing misfires. By investigating the dependence of MIE on various ignition parameters, the underlying physics during ignition and early flame propagation were thoroughly examined.

The primary objective of this research was to understand the influence of various parameters on the Minimum Ignition Energy (MIE) of different fuel mixtures. This involved conducting one-dimensional simulations to predict ignition behavior under controlled conditions. The simulations accurately replicated several phenomena observed in experiments. Notably, the results underscored the significant impacts of parameters such as mixture composition, pressure, and ignition geometry on MIE.

The first fuel used for the numerical investigation of induced ignition is methane, a key component of natural gas and the smallest hydrocarbon fuel. The results demonstrate that the relationship between MIE and the equivalence ratio follows a U-shaped trend, indicating that ignition becomes more challenging for mixtures that deviate from stoichiometry.

For primary reference fuel (PRF), important gasoline surrogate fuel consisting of iso-octane and n-heptane mixtures, the ignition and early flame propagation processes were notably influenced by the complex interplay between chemical kinetics and transport phenomena. Because of the large Lewis number for lean PRF/air mixtures, the ignition and early flame propagation process is significantly influenced by differential diffusion and curvature effect. The geometry and radius of the ignition channel was found to significantly influence the ignition process. Additionally, the chemical kinetics also plays an important role for the ignition and early flame propagation process of PRF. At 1 bar, an upturn in MIE dependence on Research Octane Number (RON) was observed in experiments. This upturn was accurately replicated in one-dimensional simulations. This phenomenon was attributed to significant diffusion effects due to curvature and differing chemical reaction pathways of

n-heptane and iso-octane. At elevated pressure, low-temperature chemistry also significantly affects the ignition process.

The stochastic nature of ignition radii, impacting ignition energy density and flame curvature, was identified as a crucial parameter contributing to the stochastic ignition behavior observed in experiments. Simulations incorporating a normal distribution for ignition radii revealed quantitative differences in MIE compared to those with fixed ignition radii, yet the experimentally observed phenomenon of the existence of upturn in MIE dependence on RON persisted.

Another significant finding was the observation of a MIE transition in both experimental forced ignition within turbulent flows and simulated forced ignition within laminar strained flames. This transition was attributed to flame extinction occurring beyond a critical strain rate. In turbulent flames in the flamelet regime, the increase in flame surface area, corresponding to the straining of the flame front, was identified as the primary influencing factor. This discovery reinforces the suitability of a laminar strained flame model for elucidating the fundamental mechanisms underlying turbulent flames in the flamelet regime.

In addition to conventional fossil fuels, renewable fuels like ammonia are gaining more attention for their potential to achieve zero carbon emissions. However, the low reactivity of ammonia presents challenges for ignition and makes it highly sensitive to heat losses. In this research, one-dimensional simulations are also conducted for ammonia and ammonia/hydrogen blend. The adiabatic flame simulation of ammonia showed a significantly wider range compared to experimental results. Conversely, simulations incorporating radiative heat loss closely matched experimental observations, emphasizing its significant impact on accurately predicting ignition behavior. Additionally, the introduction of highly reactive hydrogen into ammonia/air mixtures resulted in a substantial reduction in MIE. This enhancement underscores the potential for improving the ignition characteristics of ammonia-based fuels by augmenting their reactivity with hydrogen.

The findings of this study align closely with existing literature on forced ignition, emphasizing the sensitivity of MIE to factors such as mixture composition and ignition geometry. This research contributes to the field by offering a detailed quantitative analysis of these dependencies and validating predictions against experimental data. The insights gained are essential for both theoretical understanding and practical applications, potentially guiding the design of more efficient and safer combustion systems.

While the one-dimensional simulation approach with detailed kinetics and transport models effectively captured essential phenomenon of forced ignition

and early flame propagation in experiments, limitations were acknowledged. Three-dimensional effects such as buoyancy, non-symmetric flow fields, and non-ideal geometries (spherical/cylindrical) were not fully accounted for in one-dimensional simulations, potentially leading to quantitative discrepancies in MIE. Future research could expand upon this work by exploring multi-dimensional simulations and investigating the ignition behavior of a broader range of fuel mixtures under diverse environmental conditions.

In conclusion, this dissertation advances the understanding of forced ignition and early flame propagation in both hydrocarbon and non-carbon fuel/air mixtures. By accurately predicting the dependence of MIE on various parameters, this work provides valuable insights applicable to improving combustion efficiency and safety. Continued research in this area, particularly exploring complex scenarios bridging simulations with real-world applications, remains crucial for further advancements.

8 Liste eigener Veröffentlichungen und Konferenzbeiträge

Eigene Veröffentlichungen

- Yu, C., Li, X., Wu, C., Neagos, A. and Maas, U. "Automatic Construction of REDIM Reduced Chemistry with a Detailed Transport and Its Application to CH4 Counterflow Flames". In: *Energy & Fuels* 34.12 (2020), pp. 16572–16584.
- Wu, C., Schießl, R. and Maas, U. "Numerical studies on minimum ignition energies in methane/air and iso-octane/air mixtures". In: *Journal of Loss Prevention in the Process Industries* 72 (2021), p. 104557.
- Wu, C., Chen, Y.-R., Schießl, R., Shy, S. S. and Maas, U. "Numerical and experimental studies on minimum ignition energies in primary reference fuel/air mixtures". In: *Proceedings of the Combustion Institute* 39.2 (2023), pp. 1987–1996.
- Wu, C., Chen, Y.-R., Mai, V. T., Schießl, R., Shy, S. S., Yu, C. and Maas, U. "Experimental and numerical investigation of the induced ignition process in ammonia/air and ammonia/hydrogen/air mixtures". In: *Proceedings of the Combustion Institute* 40.1 (2024), p. 105466.

Konferenzbeiträge

- Wu, C. and Schießl, R. "Studies on the lean flammability limits of hydrogen/methane/air turbulent flames in a combustion bomb". In: *9th European Combustion Meeting*. Lisboa, Portugal, 2019.
- Wu, C., Yu, C. and Schießl, R. "Experimental and simulation studies on the influence of hydrogen addition on the lean flammability limits

of methane/air mixtures". In: *27th International Colloquium on the Dynamics of Explosions and Reactive Systems*. Beijing, China, 2019.

- Wu, C., Schießl, R. and Maas, U. "Numerical studies on minimum ignition energies in methane/air and iso-octane/air mixtures". In: *13th Symposium International Symposium on Hazards, Prevention and Mitigation of Industrial Explosions*. Braunschweig, Germany, 2020.
- Wu, C., Schießl, R. and Maas, U. "Numerical studies on minimum ignition energy of primary reference fuels". In: *10th European Combustion Meeting*. Napoli, Italy, 2021.

Bibliography

[1] Aika, K. “Brief Review of the Japanese Energy Carrier Program and an Energy Science View of Fuel Ammonia”. In: *CO2 Free Ammonia as an Energy Carrier: Japan’s Insights*. Ed. by Aika, K. and Kobayashi, H. Singapore: Springer Nature Singapore, 2023, pp. 3–16.

[2] AlAbbad, M., Javed, T., Khaled, F., Badra, J. and Farooq, A. “Ignition delay time measurements of primary reference fuel blends”. In: *Combustion and Flame* 178 (2017), pp. 205–216.

[3] Aleiferis, P. G. and Behringer, M. K. “Flame front analysis of ethanol, butanol, iso-octane and gasoline in a spark-ignition engine using laser tomography and integral length scale measurements”. In: *Combustion and Flame* 162.12 (2015), pp. 4533–4552.

[4] Alnasif, A., Mashruk, S., Shi, H., Alnajideen, M., Wang, P., Pugh, D. and Valera-Medina, A. “Evolution of ammonia reaction mechanisms and modeling parameters: A review”. In: *Applications in Energy and Combustion Science* 15 (2023), p. 100175.

[5] Andrae, J., Brinck, T. and Kalghatgi, G. “HCCI experiments with toluene reference fuels modeled by a semidetailed chemical kinetic model”. In: *Combustion and Flame* 155.4 (2008), pp. 696–712.

[6] Appel, J., Bockhorn, H. and Frenklach, M. “Kinetic modeling of soot formation with detailed chemistry and physics: laminar premixed flames of C2 hydrocarbons”. In: *Combustion and Flame* 121.1 (2000), pp. 122–136.

[7] *Standard Test Method for Research Octane Number of Spark-Ignition Engine Fuel*. Standard. ASTM International, Mar. 2000.

[8] Ballal, D. and Lefebvre, A. “The influence of spark discharge characteristics on minimum ignition energy in flowing gases”. In: *Combustion and Flame* 24 (1975), pp. 99–108.

[9] Ballal, D. R. and Lefebvre, A. H. “The influence of flow parameters on minimum ignition energy and quenching distance”. In: *Proceedings of the Combustion Institute* 15.1 (1975), pp. 1473–1481.

[10] Bane, S. *Spark Ignition: Experimental and Numerical Investigation With Application to Aviation Safety*. Dissertation. California Institute of Technology, 2010.

[11] Barnard, J. and Bradley, J. *Flame and Combustion*. New York: Chapman and Hall, 1985.

[12] Bradley, D., Gaskell, P., Sedaghat, A. and Gu, X. "Generation of PDFS for flame curvature and for flame stretch rate in premixed turbulent combustion". In: *Combustion and Flame* 135.4 (2003), pp. 503–523.

[13] Bradley, D. and Head, R. "Engine autoignition: The relationship between octane numbers and autoignition delay times". In: *Combustion and Flame* 147.3 (2006), pp. 171–184.

[14] Cai, T., Zhao, D., Chan, S. H. and Shahsavari, M. "Tailoring reduced mechanisms for predicting flame propagation and ignition characteristics in ammonia and ammonia/hydrogen mixtures". In: *Energy* 260 (2022), p. 125090.

[15] Calcote, H. F., Gregory, C. A., Barnett, C. M. and Gilmer, R. B. "Spark Ignition. Effect of Molecular Structure." In: *Industrial & Engineering Chemistry* 44.11 (1952), pp. 2656–2662.

[16] Calcote, H. F., Gregory, C. A., Barnett, C. and Gilmer, R. B. "Spark Ignition. Effect of Molecular Structure." In: *Industrial & Engineering Chemistry* 44 (1952), pp. 2656–2662.

[17] Callahan, C., Held, T., Dryer, F., Minetti, R., Ribaucour, M., Sochet, L., Faravelli, T., Gaffuri, P. and Rani, E. "Experimental data and kinetic modeling of primary reference fuel mixtures". In: *Symposium (International) on Combustion* 26.1 (1996), pp. 739–746.

[18] Candel, S. and Poinsot, T. "Flame Stretch and the Balance Equation for the Flame Area". In: *Combustion Science and Technology* 70 (Mar. 1990), pp. 1–15.

[19] Cant, R. and Bray, K. "Strained laminar flamelet calculations of premixed turbulent combustion in a closed vessel". In: *Symposium (International) on Combustion*. Vol. 22. 1. Seattle, USA, 1989, pp. 791–799.

[20] Cardin, C., Renou, B., Cabot, G. and Boukhalfa, A. M. "Experimental analysis of laser-induced spark ignition of lean turbulent premixed flames: New insight into ignition transition". In: *Combustion and Flame* 160.8 (2013), pp. 1414–1427.

[21] Cashdollar, K. L., A. Zlochower, I., Green, G. M., Thomas, R. A. and Hertzberg, M. "Flammability of methane, propane, and hydrogen gases". In: *Journal of Loss Prevention in the Process Industries* 13.3 (2000), pp. 327–340.

[22] Checkel, M. D., Ting, D. S.-K. and Bushe, W. K. "Flammability limits and burning velocities of ammonia/nitric oxide mixtures". In: *Journal of Loss Prevention in the Process Industries* 8.4 (1995), pp. 215–220.

[23] Chen, J., Jiang, X., Qin, X. and Huang, Z. "Effect of hydrogen blending on the high temperature auto-ignition of ammonia at elevated pressure". In: *Fuel* 287 (2021), p. 119563.

[24] Chen, Z., Burke, M. P. and Ju, Y. "On the critical flame radius and minimum ignition energy for spherical flame initiation". In: *Proceedings of the Combustion Institute* 33.1 (2011), pp. 1219–1226.

[25] Chi, C., Sreekumar, S. and Thévenin, D. "Data-driven discovery of heat release rate markers for premixed NH_3/H_2/air flames using physics-informed machine learning". In: *Fuel* 330 (2022), p. 125508.

[26] Ciccarelli, G., Jackson, D. and Verreault, J. "Flammability limits of NH_3–H_2–N_2–air mixtures at elevated initial temperatures". In: *Combustion and flame* 144.1-2 (2006), pp. 53–63.

[27] Coward, H. F. and Jones, G. W. "Limits of Flammability of Gases and Vapors". In: *US Bureau of Mines Bulletin*. 1952.

[28] Cui, G., Zeng, W., Li, Z., Fu, Y., Li, H. and Chen, J. "Experimental study of minimum ignition energy of methane/air mixtures at elevated temperatures and pressures". In: *Fuel* 175 (2016), pp. 257–263.

[29] Curran, H., Gaffuri, P., Pitz, W. and Westbrook, C. "A comprehensive modeling study of iso-octane oxidation". In: *Combustion and Flame* 129.3 (2002), pp. 253–280.

[30] Curran, H., Gaffuri, P., Pitz, W. and Westbrook, C. "A Comprehensive Modeling Study of n-Heptane Oxidation". In: *Combustion and Flame* 114.1 (1998), pp. 149–177.

[31] Curran, H., Pitz, W., Westbrook, C., Callahan, G. and Dryer, F. "Oxidation of automotive primary reference fuels at elevated pressures". In: *Symposium (International) on Combustion*. Vol. 27. 1. Colorado, USA, 1998, pp. 379–387.

[32] De Soete, G. “The influence of isotropic turbulence on the critical ignition energy”. In: *Symposium (International) on Combustion*. Vol. 13. 1. Utah, USA, 1971, pp. 735–743.

[33] Desantes, J., García-Oliver, J., Vera-Tudela, W., López-Pintor, D., Schneider, B. and Boulouchos, K. “Study of ignition delay time and generalization of auto-ignition for PRFs in a RCEM by means of natural chemiluminescence”. In: *Energy Conversion and Management* 111 (2016), pp. 217–228.

[34] Dimitriou, P. and Javaid, R. “A review of ammonia as a compression ignition engine fuel”. In: *International Journal of Hydrogen Energy* 45.11 (2020), pp. 7098–7118.

[35] *DIN 51 649: Bestimmung der Explosionsgrenzen von Gasen und Gasgemischen in Luft*. Beuth Verlag, Berlin, 1986.

[36] Eckhoff, R., Ngo, M. and Olsen, W. “On the minimum ignition energy (MIE) for propane/air”. In: *Journal of Hazardous Materials* 175.1 (2010), pp. 293–297.

[37] Elbaz, A. M., Giri, B. R., Issayev, G., Shrestha, K. P., Mauss, F., Farooq, A. and Roberts, W. L. “Experimental and Kinetic Modeling Study of Laminar Flame Speed of Dimethoxymethane and Ammonia Blends”. In: *Energy & Fuels* 34.11 (2020), pp. 14726–14740.

[38] Elbaz, A. M., Wang, S., Guiberti, T. F. and Roberts, W. L. “Review on the recent advances on ammonia combustion from the fundamentals to the applications”. In: *Fuel Communications* 10 (2022), p. 100053.

[39] Esser, C., Maas, U. and Warnatz, J. “Chemistry of the auto-ignition in hydrocarbon-air mixtures up to octane and its relation to engine knock”. In: *International Symposium on Diagnostics and modeling of combustion in reciprocating engines, Japan Society of Mechanical Engineers*. 1985.

[40] Essmann, S., Markus, D., Grosshans, H. and Maas, U. “Experimental investigation of the stochastic early flame propagation after ignition by a low-energy electrical discharge”. In: *Combustion and Flame* 211 (2020), pp. 44–53.

[41] Faghih, M., Valera-Medina, A., Chen, Z. and Paykani, A. “Effect of radiation on laminar flame speed determination in spherically propagating NH3-air, NH3/CH4-air and NH3/H2-air flames at normal temperature and pressure”. In: *Combustion and Flame* 257 (2023), p. 113030.

[42] Fahim, M. A., Alsahhaf, T. A. and Elkilani, A. "Chapter 5 - Catalytic Reforming and Isomerization". In: *Fundamentals of Petroleum Refining*. Ed. by Fahim, M. A., Alsahhaf, T. A. and Elkilani, A. Amsterdam: Elsevier, 2010, pp. 95–122.

[43] Fells, I. and Rutherford, A. "Burning velocity of methane-air flames". In: *Combustion and Flame* 13.2 (1969), pp. 130–138.

[44] Fernández-Tarrazo, E., Gómez-Miguel, R. and Sánchez-Sanz, M. "Minimum ignition energy of hydrogen–ammonia blends in air". In: *Fuel* 337 (2023), p. 127128.

[45] Frankel, M. L. and Sivashinsky, G. I. "On Effects Due To Thermal Expansion and Lewis Number in Spherical Flame Propagation". In: *Combustion Science and Technology* 31.3-4 (1983), pp. 131–138.

[46] G. Goyal, U. M. and Warnatz, J. "Simulation of the Behavior of Rich Hydrogen-Air Flames Near the Flammability Limit". In: *Combustion Science and Technology* 105.4-6 (1995), pp. 183–193.

[47] Galmiche, B., Halter, F. and Foucher, F. "Effects of high pressure, high temperature and dilution on laminar burning velocities and Markstein lengths of iso-octane/air mixtures". In: *Combustion and Flame* 159.11 (2012), pp. 3286–3299.

[48] Goyal, T. and Samimi-Abianeh, O. "Methane Laminar Flame Speed Measurement at High Gas Temperature Using Rapid Compression Machine-Flame (RCM-Flame)". In: *Industrial & Engineering Chemistry Research* 61.28 (2022), pp. 9981–9990.

[49] Hayakawa, A., Goto, T., Mimoto, R., Arakawa, Y., Kudo, T. and Kobayashi, H. "Laminar burning velocity and Markstein length of ammonia/air premixed flames at various pressures". In: *Fuel* 159 (2015), pp. 98–106.

[50] Hirschfelder, J. O., Curtiss, C. F. and Bird, R. B. "Molecular Theory of Gases and Liquids". In: *Physics Today* 8.3 (Mar. 1955), pp. 17–17.

[51] Hosmer Jr, D. W., Lemeshow, S. and Sturdivant, R. X. *Applied logistic regression*. New Jersey: John Wiley & Sons, 2013.

[52] Hu, E., Huang, Z., He, J. and Miao, H. "Experimental and numerical study on laminar burning velocities and flame instabilities of hydrogen–air mixtures at elevated pressures and temperatures". In: *International Journal of Hydrogen Energy* 34.20 (2009), pp. 8741–8755.

[53] Huang, C., Shy, S., Liu, C. and Yan, Y. "A transition on minimum ignition energy for lean turbulent methane combustion in flamelet and distributed regimes". In: *Proceedings of the Combustion Institute* 31.1 (2007), pp. 1401–1409.

[54] Huang, Y., Sung, C. and Eng, J. "Laminar flame speeds of primary reference fuels and reformer gas mixtures". In: *Combustion and Flame* 139.3 (2004), pp. 239–251.

[55] "Hydrogen effect on lean flammability limits and burning characteristics of an isooctane–air mixture". In: *Fuel* 266 (2020), p. 117144.

[56] Ichikawa, A., Hayakawa, A., Kitagawa, Y., Kunkuma Amila Somarathne, K., Kudo, T. and Kobayashi, H. "Laminar burning velocity and Markstein length of ammonia/hydrogen/air premixed flames at elevated pressures". In: *International Journal of Hydrogen Energy* 40.30 (2015), pp. 9570–9578.

[57] J. W. Meyer, L. M. C. and Oppenheim, A. K. "Study of Exothermic Processes in Shock Ignited Gases by the use of Laser Shear Interferometry". In: *Combustion Science and Technology* 8.4 (1973), pp. 185–197.

[58] James A. Miller Mitchell D. Smooke, R. M. G. and Kee, R. J. "Kinetic Modeling of the Oxidation of Ammonia in Flames". In: *Combustion Science and Technology* 34.1-6 (1983), pp. 149–176.

[59] Javed, T., Lee, C., AlAbbad, M., Djebbi, K., Beshir, M., Badra, J., Curran, H. and Farooq, A. "Ignition studies of n-heptane/isooctane/toluene blends". In: *Combustion and Flame* 171 (2016), pp. 223–233.

[60] Jiang, L. J., Shy, S. (, Nguyen, M. T., Huang, S. Y. and Yu, D. W. "Spark ignition probability and minimum ignition energy transition of the lean iso-octane/air mixture in premixed turbulent combustion". In: *Combustion and Flame* 187 (2018), pp. 87–95.

[61] Jones, G. and Gilliland, W. *Extinction of Gasoline Flames by Inert Gases*. Report of investigations. U.S. Department of the Interior, Bureau of Mines, 1946.

[62] Ju, Y. "Understanding cool flames and warm flames". In: *Proceedings of the Combustion Institute* 38.1 (2021), pp. 83–119.

[63] Kawka, L., Juhász, G., Papp, M., Nagy, T., Zsély, I. G. and Turányi, T. "Comparison of detailed reaction mechanisms for homogeneous ammonia combustion". In: *Zeitschrift für Physikalische Chemie* 234.7-9 (2020), pp. 1329–1357.

[64] Killingsworth, N., Powell, T., O'Donnell, R., Filipi, Z. and Hoffman, M. *Modeling the effect of thermal barrier coatings on HCCI engine combustion using CFD simulations with conjugate heat transfer*. Tech. rep. SAE Technical Paper, 2019.

[65] Kobayashi, H., Hayakawa, A., Somarathne, K. K. A. and Okafor, E. C. "Science and technology of ammonia combustion". In: *Proceedings of the Combustion Institute* 37.1 (2019), pp. 109–133.

[66] Kondo, S., Takizawa, K., Takahashi, A., Tokuhashi, K. and Sekiya, A. "A study on flammability limits of fuel mixtures". In: *Journal of Hazardous Materials* 155.3 (2008), pp. 440–448.

[67] Konig, G. and Sheppard, C. G. W. "End Gas Autoignition and Knock in a Spark Ignition Engine". In: *SAE Transactions* 99 (1990), pp. 820–839.

[68] Law, C. K. "A Compilation of Experimental Data on Laminar Burning Velocities". In: *Reduced Kinetic Mechanisms for Applications in Combustion Systems*. Ed. by Peters, N. and Rogg, B. Berlin, Heidelberg: Springer Berlin Heidelberg, 1993, pp. 15–26.

[69] Law, C. "Dynamics of stretched flames". In: *Symposium (International) on Combustion*. Vol. 22. 1. Seattle, USA, 1989, pp. 1381–1402.

[70] Law, C. and Egolfopoulos, F. "A kinetic criterion of flammability limits: The C-H-O-inert system". In: *Symposium (International) on Combustion*. Vol. 23. 1. Orleans, France, 1991, pp. 413–421.

[71] Law, C. K. *Combustion Physics*. Cambridge: Cambridge University Press, 2006.

[72] Lawes, M., Ormsby, M. P., Sheppard, C. G. and Woolley, R. "The turbulent burning velocity of iso-octane/air mixtures". In: *Combustion and Flame* 159.5 (2012), pp. 1949–1959.

[73] Lesmana, H. "Ignition and Combustion Characteristics of Partially Dissociated NH_3 in Air". English. PhD thesis. The University of Western Australia, 2021.

[74] Lewis, B. and von Elbe, G. *Combustion, Flames and Explosions of Gases*. New York: Elsevier, 1987.

[75] Li, J., Huang, H., Kobayashi, N., Wang, C. and Yuan, H. "Numerical study on laminar burning velocity and ignition delay time of ammonia flame with hydrogen addition". In: *Energy* 126 (2017), pp. 796–809.

[76] Liao, Y.-H. and Roberts, W. L. "Laminar Flame Speeds of Gasoline Surrogates Measured with the Flat Flame Method". In: *Energy & Fuels* 30.2 (2016), pp. 1317–1324.

[77] Linnett, J. and Simpson, C. "Limits of inflammability". In: *Symposium (International) on Combustion*. Vol. 6. 1. Connecticut, USA, 1957, pp. 20–27.

[78] Lutz, A. E., Kee, R. J., Miller, J. A., Dwyer, H. A. and Oppenheim, A. K. "Dynamic effects of autoignition centers for hydrogen and C1,2-hydrocarbon fuels". In: *Symposium (International) on Combustion*. Vol. 22. 1. Seattle, USA, 1989, pp. 1683–1693.

[79] Maas, U. "Mathematische Modellierung instationärer Verbrennungsprozesse unter Verwendung detaillierter Reaktionsmechanismen". PhD thesis. Universität Heidelberg, 1988.

[80] Maas, U. and Warnatz, J. "Ignition processes in hydrogen/oxygen mixtures". In: *Combustion and Flame* 74.1 (1988), pp. 53–69.

[81] Maas, U. "Selbstzündung in Kohlenwasserstoff- Luft- Gemischen bis zu Oktan und ihre Beziehung zum Motorklopfen". MA thesis. Ruprecht-Karls-Universität zu Heidelberg, 1985.

[82] Maly, R. "Spark Ignition: Its Physics and Effect on the Internal Combustion Engine". In: *Fuel Economy: in Road Vehicles Powered by Spark Ignition Engines*. Ed. by Hilliard, J. C. and Springer, G. S. Boston, MA: Springer US, 1984, pp. 91–148.

[83] Mastorakos, E. "Ignition of turbulent non-premixed flames". In: *Progress in Energy and Combustion Science* 35.1 (2009), pp. 57–97.

[84] Mathurkar, H. "Minimum ignition energy and ignition probability for Methane, Hydrogen and their mixtures". PhD thesis. Loughborough University, 2009.

[85] Meneveau, C. and Poinsot, T. "Stretching and quenching of flamelets in premixed turbulent combustion". In: *Combustion and Flame* 86.4 (1991), pp. 311–332.

[86] Merker, G. P., Schwarz, C., Stiesch, G. and Otto, F. *Simulating Combustion: Simulation of combustion and pollutant formation for engine-development*. Berlin: Springer Science & Business Media, 2005.

[87] Metzler, A. J. "Minimum ignition energies of six pure hydrocarbon fuels of the C2 and C6 series". In: *NACA report RM E52F27*. 1952.

[88] Moorhouse, J., Williams, A. and Maddison, T. "An investigation of the minimum ignition energies of some C1 to C7 hydrocarbons". In: *Combustion and Flame* 23.2 (1974), pp. 203–213.

[89] Najm, H. N., Paul, P. H., Mueller, C. J. and Wyckoff, P. S. "On the adequacy of certain experimental observables as measurements of flame burning rate". In: *Combustion and Flame* 113.3 (May 1998).

[90] Nakamura, H. and Shindo, M. "Effects of radiation heat loss on laminar premixed ammonia/air flames". In: *Proceedings of the Combustion Institute* 37.2 (2019), pp. 1741–1748.

[91] Otomo, J., Koshi, M., Mitsumori, T., Iwasaki, H. and Yamada, K. "Chemical kinetic modeling of ammonia oxidation with improved reaction mechanism for ammonia/air and ammonia/hydrogen/air combustion". In: *International Journal of Hydrogen Energy* 43.5 (2018), pp. 3004–3014.

[92] Palies, P. "2 - Premixed combustion for combustors". In: *Stabilization and Dynamic of Premixed Swirling Flames*. Ed. by Palies, P. London: Academic Press, 2020, pp. 57–103.

[93] Paul, P. H. and Najm, H. N. "Planar laser-induced fluorescence imaging of flame heat release rate". In: *Symposium (International) on Combustion*. Vol. 27. 1. Colorado, USA, 1998, pp. 43–50.

[94] Peters, N. "Laminar flamelet concepts in turbulent combustion". In: *Symposium (International) on Combustion*. Vol. 21. 1. Seattle, USA, 1988, pp. 1231–1250.

[95] Pfahl, U., Ross, M., Shepherd, J., Pasamehmetoglu, K. and Unal, C. "Flammability limits, ignition energy, and flame speeds in H_2 – CH_4 – NH_3 – N_2O – O_2 – N_2 mixtures". In: *Combustion and flame* 123.1 (2000), pp. 140–158.

[96] Pochet, M., Dias, V., Moreau, B., Foucher, F., Jeanmart, H. and Contino, F. "Experimental and numerical study, under LTC conditions, of ammonia ignition delay with and without hydrogen addition". In: *Proceedings of the Combustion Institute* 37.1 (2019), pp. 621–629.

[97] Poinsot, T. and Veynante, D. *Theoretical and Numerical Combustion*. Philadelphia: Edwards, 2005.

[98] Reuter, C. B., Won, S. H. and Ju, Y. "Cool Flames Activated by Ozone Addition". In: *53rd AIAA Aerospace Sciences Meeting*. Kissimmee, Florida.

[99] Ronney, P. D. "Effect of Chemistry and Transport Properties on Near-Limit Flames at Microgravity". In: *Combustion Science and Technology* 59.1-3 (1988), pp. 123–141.

[100] Ronney, P. D. "Understanding combustion processes through microgravity research". In: *Symposium (International) on Combustion*. Vol. 27. 2. Colorado, USA, 1998, pp. 2485–2506.

[101] Sadaghiani, M. S., Arami-Niya, A., Zhang, D., Tsuji, T., Tanaka, Y., Seiki, Y. and May, E. F. "Minimum ignition energies and laminar burning velocities of ammonia, HFO-1234yf, HFC-32 and their mixtures with carbon dioxide, HFC-125 and HFC-134a". In: *Journal of Hazardous Materials* 407 (2021), p. 124781.

[102] Schröder, V. and Molnarne, M. "Flammability of gas mixtures: Part 1: Fire potential". In: *Journal of Hazardous Materials* 121.1 (2005), pp. 37–44.

[103] Shepherd, J. E., Krok, J. C. and Lee, J. J. "Spark ignition energy measurements in Jet A". In: *Explosion Dynamics Laboratory Report FM97-9* (2000).

[104] Shrestha, K. P., Seidel, L., Zeuch, T. and Mauss, F. "Detailed Kinetic Mechanism for the Oxidation of Ammonia Including the Formation and Reduction of Nitrogen Oxides". In: *Energy & Fuels* 32.10 (2018), pp. 10202–10217.

[105] Shy, S., Shiu, Y., Jiang, L., Liu, C. and Minaev, S. "Measurement and scaling of minimum ignition energy transition for spark ignition in intense isotropic turbulence from 1 to 5 atm". In: *Proceedings of the Combustion Institute* 36.2 (2017), pp. 1785–1791.

[106] Shy, S. (, Liao, Y.-C., Chen, Y.-R. and Huang, S.-Y. "Two ignition transition modes at small and large distances between electrodes of a lean primary reference automobile fuel/air mixture at 373 K with Lewis number » 1". In: *Combustion and Flame* 225 (2021), pp. 340–348.

[107] Smith, G. P., Golden, D. M., Frenklach, M., Moriarty, N. W., Eiteneer, B., Goldenberg, M., Bowman, C. T., Hanson, R. K., Song, S., Jr., W. C. G. and Lissianski, V. V. *GRI-Mech 3.0*. `http://www.me.berkeley.edu/gri_mech/` [Accessed: (03.04.2024)]. 2011.

[108] Stahl, G. and Warnatz, J. "Numerical investigation of time-dependent properties and extinction of strained methane- and propane-air flamelets". In: *Combustion and Flame* 85.3 (1991), pp. 285–299.

[109] Steinberg, A. M., Hamlington, P. E. and Zhao, X. "Structure and dynamics of highly turbulent premixed combustion". In: *Progress in Energy and Combustion Science* 85 (2021), p. 100900.

[110] Sun, C. and Law, C. "On the nonlinear response of stretched premixed flames". In: *Combustion and Flame* 121.1 (2000), pp. 236–248.

[111] Svehla, G. "Nomenclature of kinetic methods of analysis (IUPAC Recommendations 1993)". In: *Pure and Applied Chemistry* 65.10 (1993), pp. 2291–2298.

[112] Takashi, H. and Kimitoshi, T. "Laminar flame speed of ethanol, n-heptane, iso-octane air mixtures". In: *FISITA 2006 World Automotive Congress, the Japan Society of Mechanical Engineers*. Yokohama, Japan: Japan Society of Mechanical Engineers, 2006.

[113] Turns, S. R. et al. *Introduction to combustion*. Vol. 287. New York: McGraw-Hill Companies, 1996.

[114] Turquand d'Auzay, C., Papapostolou, V., Ahmed, S. F. and Chakraborty, N. "On the minimum ignition energy and its transition in the localised forced ignition of turbulent homogeneous mixtures". In: *Combustion and Flame* 201 (2019), pp. 104–117.

[115] University of California at San Diego. *Chemical-Kinetic Mechanisms for Combustion Applications*. San Diego Mechanism web page, Mechanical and Aerospace Engineering (Combustion Research), University of California at San Diego `http://combustion.ucsd.edu` [Accessed: (03.04.2024)].

[116] Urban, J. L. and Fernandez-Pello, A. C. "Ignition". In: *Encyclopedia of Wildfires and Wildland-Urban Interface (WUI) Fires*. Ed. by Manzello, S. L. Cham: Springer, 2018, pp. 1–9.

[117] Van den Schoor, F., Hermanns, R., van Oijen, J., Verplaetsen, F. and de Goey, L. "Comparison and evaluation of methods for the determination of flammability limits, applied to methane/hydrogen/air mixtures". In: *Journal of Hazardous Materials* 150.3 (2008), pp. 573–581.

[118] Verkamp, F., Hardin, M. and Williams, J. "Ammonia combustion properties and performance in gas-turbine burners". In: *Proceedings of the Combustion Institute* 11.1 (1967), pp. 985–992.

[119] Wähner, A., Gramse, G., Langer, T. and Beyer, M. “Determination of the minimum ignition energy on the basis of a statistical approach”. In: *Journal of Loss Prevention in the Process Industries* 26.6 (2013), pp. 1655–1660.

[120] Wang, D., Ji, C., Wang, S., Yang, J. and Wang, Z. “Numerical study of the premixed ammonia-hydrogen combustion under engine-relevant conditions”. In: *International Journal of Hydrogen Energy* 46.2 (2021), pp. 2667–2683.

[121] Wang, H., Hawkes, E. R., Zhou, B., Chen, J. H., Li, Z. and Aldén, M. “A comparison between direct numerical simulation and experiment of the turbulent burning velocity-related statistics in a turbulent methane-air premixed jet flame at high Karlovitz number”. In: *Proceedings of the Combustion Institute* 36.2 (2017), pp. 2045–2053.

[122] Wang, H., DelVescovo, D., Zheng, Z., Yao, M. and Reitz, R. D. “Reaction Mechanisms and HCCI Combustion Processes of Mixtures of n-Heptane and the Butanols”. In: *Frontiers in Mechanical Engineering* 1 (2015).

[123] Warnatz, J., Maas, U. and Dibble, R. *Combustion: Physical and Chemical Fundamentals, Modeling and Simulation, Experiments, Pollutant Formation*. Berlin: Springer, 2009.

[124] Warnatz, J. “The Mechanism of High Temperature Combustion of Propane and Butane”. In: *Combustion Science and Technology* 34.1-6 (1983), pp. 177–200.

[125] Weaver, C. S. “Natural Gas Vehicles — A Review of the State of the Art”. In: *SAE Transactions* 98 (1989), pp. 1190–1210.

[126] Westbrook, C. K., Mizobuchi, Y., Poinsot, T. J., Smith, P. J. and Warnatz, J. “Computational combustion”. In: *Proceedings of the Combustion Institute* 30.1 (2005), pp. 125–157.

[127] Williams, F. A. “Recent Advances in Theoretical Descriptions of Turbulent Diffusion Flames”. In: *Turbulent Mixing in Nonreactive and Reactive Flows*. Ed. by Murthy, S. N. B. Boston: Springer, 1975, pp. 189–208.

[128] Wu, C., Chen, Y.-R., Schießl, R., Shy, S. S. and Maas, U. “Numerical and experimental studies on minimum ignition energies in primary reference fuel/air mixtures”. In: *Proceedings of the Combustion Institute* 39.2 (2023), pp. 1987–1996.

[129] Wu, C., Schießl, R. and Maas, U. “Numerical studies on minimum ignition energies in methane/air and iso-octane/air mixtures”. In: *Journal of Loss Prevention in the Process Industries* 72 (2021), p. 104557.

[130] Wu, C., Chen, Y.-R., Mai, V. T., Schießl, R., Shy, S. S., Yu, C. and Maas, U. “Experimental and numerical investigation of the induced ignition process in ammonia/air and ammonia/hydrogen/air mixtures”. In: *Proceedings of the Combustion Institute* 40.1 (2024), p. 105466.

[131] Wu, C. and Schießl, R. “Studies on the lean flammability limits of hydrogen/methane/air turbulent flames in a combustion bomb”. In: *9th European Combustion Meeting*. Lisboa, Portugal, 2019.

[132] Wu, C., Schießl, R. and Maas, U. “Numerical studies on minimum ignition energies in methane/air and iso-octane/air mixtures”. In: *13th Symposium International Symposium on Hazards, Prevention and Mitigation of Industrial Explosions*. Braunschweig, Germany, 2020.

[133] Wu, C., Schießl, R. and Maas, U. “Numerical studies on minimum ignition energy of primary reference fuels”. In: *10th European Combustion Meeting*. Napoli, Italy, 2021.

[134] Wu, C., Yu, C. and Schießl, R. “Experimental and simulation studies on the influence of hydrogen addition on the lean flammability limits of methane/air mixtures”. In: *27th International Colloquium on the Dynamics of Explosions and Reactive Systems*. Beijing, China, 2019.

[135] Xie, C., Lailliau, M., Issayev, G., Xu, Q., Chen, W., Dagaut, P., Farooq, A., Sarathy, S. M., Wei, L. and Wang, Z. “Revisiting low temperature oxidation chemistry of n-heptane”. In: *Combustion and Flame* 242 (2022), p. 112177.

[136] Yang, Q. and Zhao, P. “Minimum ignition energy and propagation dynamics of laminar premixed cool flames”. In: *Proceedings of the Combustion Institute* 38.2 (2021), pp. 2315–2322.

[137] Yeung, P., Girimaji, S. and Pope, S. “Straining and scalar dissipation on material surfaces in turbulence: Implications for flamelets”. In: *Combustion and Flame* 79.3 (1990), pp. 340–365.

[138] Yu, C., Markus, D., Schießl, R. and Maas, U. “Numerical study on spark ignition of laminar lean premixed methane-air flames in counterflow configuration”. In: *Combustion Science and Technology* 195 (Dec. 2021), pp. 1–25.

[139] Yu, C., Eckart, S., Essmann, S., Markus, D., Valera-Medina, A., Schießl, R., Shu, B., Krause, H. and Maas, U. "Investigation of spark ignition processes of laminar strained premixed stoichiometric NH_3-H_2-air flames". In: *Journal of Loss Prevention in the Process Industries* 83 (2023), p. 105043.

[140] Yu, C., Li, X., Wu, C., Neagos, A. and Maas, U. "Automatic Construction of REDIM Reduced Chemistry with a Detailed Transport and Its Application to CH4 Counterflow Flames". In: *Energy & Fuels* 34.12 (2020), pp. 16572–16584.

[141] Zabetakis, M. G., Scott, G. S. and Jones, G. W. "Limits of Flammability of Paraffin Hydrocarbons in Air". In: *Industrial & Engineering Chemistry* 43.9 (1951), pp. 2120–2124.

[142] Zhang, H. and Modest, M. F. "Evaluation of the Planck-mean absorption coefficients from HITRAN and HITEMP databases". In: *Journal of Quantitative Spectroscopy and Radiative Transfer* 73.6 (2002), pp. 649–653.

[143] Zhu, J., Li, J., Wang, S., Raza, M., Qian, Y., Feng, Y., Yu, L., Mao, Y. and Lu, X. "Ignition delay time measurements and kinetic modeling of methane/diesel mixtures at elevated pressures". In: *Combustion and Flame* 229 (2021), p. 111390.

[144] Zhukov, V. P. and Kong, A. F. "A Compact Reaction Mechanism of Methane Oxidation at High Pressures". In: *Progress in Reaction Kinetics and Mechanism* 43.1 (2018), pp. 62–78.